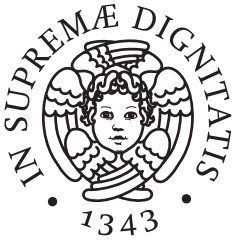

Università di Pisa

Corso di Laurea Magistrale in Fisica

Tesi di Laurea

Tracking performances of the ATLAS detector for the HL-LHC and impact on the $\mathbf{H \to ZZ^* \to 4\mu}$ channel

Relatori:
Prof. *Giorgio Chiarelli*
Dott. *Claudia Gemme*

Candidato:
Federico Massa

Anno Accademico 2015-2016

Contents

Introduction

This thesis is centered on the expected performance of the tracking system (ITk) which is being designed for the ATLAS upgrade and that will replace the current Inner Detector in the High Luminosity LHC phase (HL-LHC), scheduled to start in 2026.

The Large Hadron Collider (LHC) worked at a center-of-mass energy of 7 TeV during Run-1 and 13 TeV during Run-2. It is scheduled to be upgraded in two different stages: the first one will begin after the end of Run-2 during the Long shutdown 2 (LS2) in 2019-2020, when LHC will reach its maximum design energy of 14 TeV; the second one will start at the end of Run-3 during the Long shutdown 3 (LS3) in 2024-2026 (Fig.1). The latter stage will lead to what is dubbed as High-Luminosity LHC (HL-LHC) during which the instantaneous luminosity will reach the maximum value of 7.5×10^{34} cm^{-2}s^{-1}, corresponding to approximately 3000 fb^{-1} over ten years of data taking.

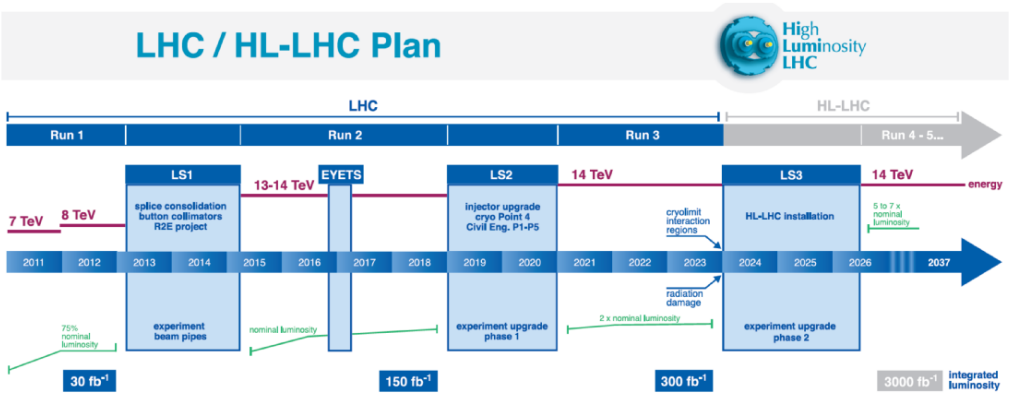

Figure 1: LHC/HL-LHC Plan as scheduled in 2015[1].

HL-LHC will provide an opportunity to study new physics processes, such as extra dimensions or the ones predicted by SUSY models, as well as improve

Standard Model measurements. In particular, Higgs boson couplings are expected to be measured with a precision between 5% and 30%[2]. Thanks to the increased luminosity, it will be possible to observe the Higgs boson in extremely rare channels, which are beyond today's capabilities.

By the end of Run-3, ATLAS detector will be using 15-20 years old components. In particular, the highly irradiated Inner Detector pixels and strips will have reached the end of their lifetime and the transition radiation tracker will reach 100% occupancy at that luminosity. Thus, the Inner Detector must be completely replaced by the Inner Tracker (ITk), which will have to guarantee the same or an improved performance in the harsh conditions of HL-LHC while maximizing the acceptance.

At design luminosity, the expected number of in-time pileup events will be about $\langle\mu\rangle = 200$, a much higher value than the one expected at the end of Run-3 ($\langle\mu\rangle = 80$) and even more if compared to the current one ($\langle\mu\rangle = 23$), introducing new challenges in the pattern recognition. The increase of the number of collisions per bunch crossing leads to new requirements on the front-end electronics, trigger and data acquisition system that cannot be met by the current apparatus, thus leading to a substantial upgrade of the electronics. Moreover, the Reference Scenario of the Scoping Document[1] proposes an increase of the geometrical acceptance of the detector by extending the $|\eta|$ coverage to 4.0, which requires either the replacement (such as in the case of ITk) or the addition of new detectors (muon chambers, calorimeter system). At the moment the ATLAS collaboration is working on the design of a robust ITk layout which will be able to perform adequately.

Other than detector and hardware upgrades, HL-LHC will require software upgrades to meet the needs of the new detectors, handle large event samples and adapt to multi-processor architectures. To deal with the simulation size and time requirements it will be necessary to mix fast simulation techniques (using detector parametrisations) with full simulation at event level.

My work was focused on the development of a fast simulation method that allows to simulate the effect of the high number of pile-up events on the tracking and physics performances, applied to single particle ("particle-gun") and $H \to ZZ^* \to 4\mu$ Monte Carlo studies. A fast simulation technique is needed as we want to quickly compare, in a realistic scenario, different detector designs and layouts. Besides, as Higgs physics is of the utmost importance it is useful to check our capability to perform well in the high luminosity

environment.

ATLAS presented a Scoping Document[1] last year. In this document three different upgrade scenarios ("Reference", "Middle" and "Low") with different angular coverage ($|\eta| < 4.0$, $|\eta| < 3.2$ and $|\eta| < 2.7$ respectively) and costs (about 120'000, 110'000 and 100'000 kCHF respectively), were discussed. While it is important to recall that about 50% of the cost of the upgrade is due to the ITk, the three scenarios have also impacts on other parts of the upgrade.

Unless otherwise specified, in this thesis we use c = 1, MeV for energies and momenta, mm for lengths and seconds for times.

This thesis is structured as follows. After a brief overview of the Standard Model and the most important measurements that will be performed during the high-luminosity phase, the current ATLAS detector is described, together with the foreseen upgrades.

The physics objects reconstruction in ATLAS is then described, with particular attention to the muon identification.

In the next chapter, we first describe the standard ATLAS simulation technique and then we present the fast simulation technique and its applications to single particle ("particle gun") and physics studies.

Finally we show the results, comparing the tracking and physics performances of the three proposed ITk layouts in different pile-up scenarios and checking that they respect the requirements fixed by the Collaboration.

Chapter 1

The Physics Scenario

As the upgraded detector for the high luminosity phase is foreseen to keep or improve the current ATLAS performance in spite of the huge amount of pileup events, the benefits gained from the increase in statistics will be fundamental to increase the accuracy of already performed measurements and to discover or improve the current limits on new physics.

This section briefly describes some of the physics channels that will mostly benefit from the high luminosity phase.

1.1 The Standard Model

The *Standard Model* (SM) of Elementary Particles is a gauge theory that describes the electromagnetic, weak and strong interactions of the known subatomic particles. The theory does not include general relativity, but is very well verified in a wide range of processes. The discovery of the vector bosons $W^{\pm}$ and Z_0[3] and of the top quark[4][5] lent credibility to it. The recent observation of a particle consistent with the SM Higgs boson[6][7] in 2012 started a new era of physics discovery at LHC.

So far, four fundamental interactions have been observed: gravity, electromagnetism, the weak interaction and the strong interaction, each of which (with the exception of gravity) is described, in the SM, by an elementary particle, or field. The SM belongs to the class of gauge theories and is based on a mathematical description that naturally incorporates quantum mechanics and special relativity. Within this theoretical framework, the interactions between fermions are obtained by requiring the invariance of the Lagrangian with respect to an arbitrary transformation of the fields describing

the particles according to the local symmetry group $SU(3)_C \otimes SU(2)_L \otimes U(1)_Y$, in which the three terms describe respectively: the symmetry group of the colored strong interactions of quantum chromodynamics, the left-handed weak isospin doublets and the right-handed weak hypercharge singlets. Together, the $SU(2)_L \otimes U(1)_Y$ group governs the unified *electroweak interaction*.

SM constituents

In the SM, the elementary particles are spin-1 *gauge bosons* and half-integer spin *fermions*, the latter divided into *leptons* and *quarks*.

The gauge bosons mediate the interactions and are generators of the symmetry group. 8 colored *gluons* are the mediators of the strong force and are the generator of the group $SU(3)_C$. The photon, $W^{\pm}$ and Z_0 are the force carriers of the electroweak interactions and are the generators of the group $SU(2)_L \otimes U(1)_Y$.

Six types of leptons form the SM, with their respective antiparticles. These are the electron (e), muon (μ) and tau (τ), each forming a left-handed (with -1 eigenvalue chirality) doublet with their respective neutrino (ν_e, ν_μ, ν_τ). As right-handed neutrinos are not observed, the right-handed fermions form a singlet for $SU(2)_L$.

Six types of quarks (with their antiparticles) are present in the SM, arranged in isospin doublets:

$$\begin{pmatrix} u \\ d \end{pmatrix}, \begin{pmatrix} c \\ s \end{pmatrix}, \begin{pmatrix} t \\ b \end{pmatrix}$$

They have fractional electric charge and a quantum property called *color*, which is the source of their strong interaction and comes in three states: red, green and blue. Experiments showed that quark mass eigenstates are different from electroweak interaction eigenstates. The latter are given by:

$$\begin{pmatrix} u \\ d' \end{pmatrix}, \begin{pmatrix} c \\ s' \end{pmatrix}, \begin{pmatrix} t \\ b' \end{pmatrix}$$

with

$$\begin{pmatrix} d' \\ s' \\ b' \end{pmatrix} = \begin{pmatrix} V_{ud} & V_{us} & V_{ub} \\ V_{cd} & V_{cs} & V_{cb} \\ V_{td} & V_{ts} & V_{tb} \end{pmatrix} \cdot \begin{pmatrix} d \\ s \\ b \end{pmatrix}$$

The matrix shown is called the Cabibbo-Kobayashi-Maskawa (CKM) matrix. Imposing unitarity, only four free parameters are independent. Their values are not predicted by the theory, but they can be measured in experiments.

The Higgs mechanism

The gauge invariance of $SU(2)_L \otimes U(1)_Y$ implies massless fermions and weak bosons, which contradicts the experimental results. A spin-0 scalar gauge field boson, which was observed only in 2012, after almost 40 years from its theorization[8], can generate the fermion and the weak boson masses as a result of a spontaneously broken symmetry arising in the $SU(2)_L \otimes U(1)_Y$ electroweak sector.

1.2 Measurements of the Higgs boson properties

The most important part of the physics programme at the HL-LHC is probably the study of the Higgs boson, with the precise determination of its characteristics, and its couplings to fermions and vector bosons[2].

At LHC the Higgs boson is produced in several processes, shown in Fig.1.1, with the dominant one being the gluon-gluon fusion, as can be seen in Fig.1.2a. It can be observed in a large number of final states, whose SM branching ratios are shown in Fig.1.2b. There are, however, models that predict Higgs bosons with couplings that can be different from the ones described in the SM, for example in some models predicting other heavy Higgs states. For this reason, an important goal of future studies is to measure the Higgs couplings as precisely as possible to search for potential new physics.

The large value of the luminosity at HL-LHC will allow to study the Higgs boson in a large number of production and decay modes. Fig.1.3a shows the precision on the measurement of the signal strength in each of them. The table in Tab.1.1 summarizes the results, and shows that in many channels (where the total uncertainty is dominated by the experimental contribution at 300 fb^{-1}) it is expected that they will be dominated by the theoretical contribution, assuming the current precision on the models, at 3000 fb^{-1}. The dominant production mode, $gg \to H$, is expected to reach an experimental precision of around 4%, which is very close to the limit imposed by the luminosity measurement, 3%, providing an important test of the Standard Model.

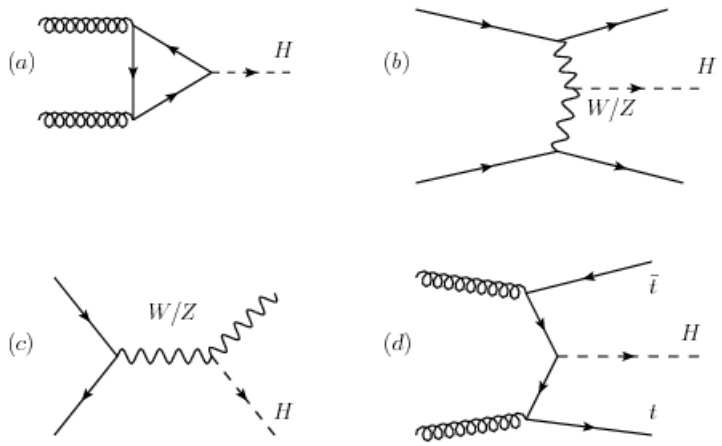

Figure 1.1: Feynman diagrams of Higgs production channels at LHC[10]. (a) gluon-gluon fusion (ggF) (b) Vector boson fusion (VBF) (c) W/Z bremmstrahlung (d) $t\bar{t}$ fusion

Besides, cross sections of rare production modes, like $t\bar{t}H$ will be measured with an expected precision around 10%. The channels that most profit from the luminosity upgrade in terms of measurement accuracy are the $\gamma\gamma$ and ZZ^* as in those channels the uncertainties are dominated by statistics. In other cases, such as in $WH/ZH, H \to b\bar{b}$ both the jet energy resolution and the rejection of light jets are crucial for the calculation, and suffer from the high pileup environment.

The data that will be gathered during the HL-LHC programme will also allow to measure many different Higgs couplings with a good precision. The results, extrapolated at 300 fb^{-1} and 3000 fb^{-1} are shown in Fig.1.3b.

Several analyses, based on the results of Run-1 analysis, were performed simulating the proposed upgraded detector by parametrising the calorimeter and muon spectrometer response[2][1]:

- $H \to \gamma\gamma$ in the 0-jet and the 2-jet final state.
- Inclusive $H \to ZZ^* \to 4\mu$.
- Vector boson fusion $H \to ZZ^* \to 4l$.
- $H \to WW^* \to l\nu l\nu$ in the 0-jet and the 2-jet final state.
- $H \to \tau^+\tau^-$ in the 2-jet final state.

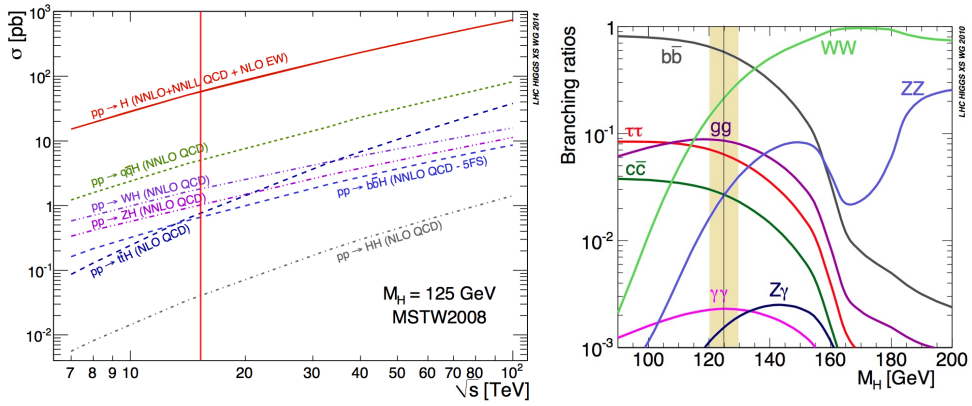

(a) (b)

Figure 1.2: (a): Cross sections of the Higgs boson production in p-p collisions as a function of the center of mass energy[11]. The red line shows the 14 TeV energy of the HL-LHC phase. (b): Branching ratios of the SM Higgs boson as a function of its mass, with the measured mass region highlighted[11].

Also, some channels which are too rare for LHC but are expected to have a good chance to be observed in the high-luminosity phase were studied:

- $WH/ZH/t\bar{t}H, H \to \gamma\gamma$.
- $H \to \mu\mu$.
- $t\bar{t}H \to \mu\mu$.

From a phenomenological standpoint, to find out if the Higgs mechanism is the one responsible for electroweak symmetry breaking, it is important to measure the Higgs self-couplings. In particular, the Higgs boson trilinear self-coupling λ_{HHH} can be measured in the double Higgs boson production channel. Cross section of this process in the Standard Model is predicted to be 34 ± 6 fb, which is about three orders of magnitude smaller than the total Higgs production cross section and thus needs high luminosity to be measured.

For these studies, interesting channels are $HH \to b\bar{b}W^+W^-$ and $HH \to b\bar{b}\gamma\gamma$. Their sensibility for the HL-LHC upgrade has been studied in [13]. The first is indistinguishable from the $H \to t\bar{t}$, so that it suffers from a huge background that makes impossible to measure the Higgs self coupling; the

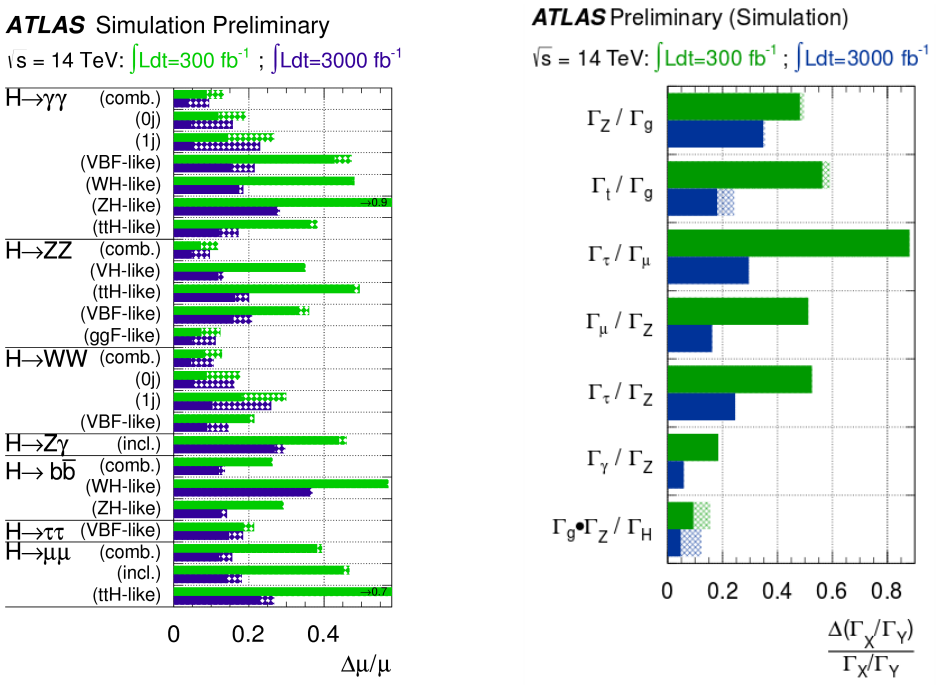

(a) (b)

Figure 1.3: (a): Expected measurement precision of the signal strength $\mu = (\sigma \times BR)/(\sigma \times BR)_{SM}$[2] at different integrated luminosity, for different production channels. (b): Expected measurement precision of the ratio between the Higgs couplings, assuming a SM Higgs boson with a mass of 125 GeV and with different integrated luminosities. The experimental and current theoretical uncertainties are shown separately, respectively with filled and hashed areas[12].

latter has a small branching ratio, but its signature is clear and is expected to produce $\simeq$ 260 events in 3000 fb^{-1}. After the analysis selection this channel is expected to provide a S/B ratio of around 0.6, with the background dominated by $t\bar{t}H$. The preliminary results of these studies show that none on these channels, taken alone, can provide a measurement of the Higgs self coupling, but it is expected that, combining the results of all the channels with the ones of the CMS experiment, a 30 % measurement should be feasible at HL-LHC.

1.3 Weak boson scattering

The weak boson scattering (WBS) is a promising new physics channel because the predicted increase of its cross-section in the longitudinal mode

would violate unitarity at the TeV energy scale. In the SM the Higgs boson is responsible for its damping, while other theoretical models, such as Technicolour and little Higgs, predicts TeV-scale resonances and a light scalar particle that can achieve the same effect. Even if the Higgs mechanism was established, other mechanisms can produce an observable difference in the WBS processes, thus it is very important to measure the energy dependence of this cross-section. In [14] it is shown that, thanks to the improved statistics of HL-LHC, the channel $ZZjj \rightarrow lllljj$ can be pushed to the level of discovery and its cross section be measured with a statistical precision of about 10 %.

1.4 Supersymmetry searches

The study of weak scale supersymmetry (SUSY) remains one of the top priorities at LHC. SUSY models predict that every SM particle has a supersymmetric partner and Run-1 analysis has already excluded, assuming a light LSP, that the 1st and 2nd generation of squarks (supersymmetric partner of the quarks) and the gluino (supersymmetric partner of the gluon) lies in the mass region below 1.4 TeV and 1.0 TeV respectively. Because of the flexibility on the parameters of the SUSY models, the current limits on 3rd generation squarks, gauginos and sleptons (supersymmetric partner of the gauge bosons and leptons respectively) cannot rule out several SUSY scenarios.

The **squark and gluino searches** are usually carried out by looking at final states with multiple jets and large missing transverse momentum. With 3000 fb^{-1}, the limits for the discovery are pushed at $\simeq$ 400-500 GeV[2] in the simplistic model that assumes a zero-mass LSP (the result is, however, preserved in less stringent hypotheses). The main background emerges from $Z \rightarrow \nu\nu + jets$ and $t\bar{t}$ production.

Third generation searches are also interesting because naturalness arguments require the stop (SUSY partner of the top quark) to be light (below 1 TeV). Its cross-section is expected to grow significantly when considering smaller masses, from 10 fb for a 1 TeV stop to 240 fb for a 600 GeV stop. At HL-LHC, the sensibility for the top squark will significantly increase and, if found, it will be possible to measure its properties.

Stop can be observed in a large number of modes, including top or bottom quarks, W/Z or Higgs bosons and an LSP. Such event would be character-

ised by the presence of several jets (including b-jets), large missing transverse momentum and possibly leptons. Studies described in [2] show that the stop mass limits can be increased by up to 200 GeV at HL-LHC, with further improvements still possible.

In scenarios with heavy squarks and gluinos, the SUSY production modes are dominated by pair production of **weak gauginos**. The predicted associated production cross sections of $\widetilde{\chi}_1^{\pm} - \widetilde{\chi}_2^0$ decrease significantly with increasing masses. Assuming 100% branching ratios for the decays $\widetilde{\chi}_1^{\pm} \rightarrow W^{\pm(*)}\widetilde{\chi}_1^0$ and $\widetilde{\chi}_2^0 \rightarrow Z^{(*)}\widetilde{\chi}_1^0$, the event selection can be performed by looking for final states with three charged leptons and missing transverse momentum, where a pair of same flavour and opposite sign leptons comes from a Z boson. The main backgrounds consists of $t\bar{t}$ and WZ production. At the end of the LHC program, scenarios with chargino masses up to 500 GeV can be probed with a neutralino mass below 100 GeV, while at HL-LHC it will be possible to probe scenarios with chargino masses up to 800 GeV and neutralino masses below 300 GeV.

1.5 Exotic sector

Exotic phenomena include a very large number of models and, consequently, a broad range of the parameters. However, their characteristic feature is the production of high-p_T leptons, photons and jets and the measurement of missing E_T. Two important exotic channels are presented in [2] to ensure that HL-LHC maintains or improve the sensitivity to their signatures: $t\bar{t}$ and di-lepton resonances.

$t\bar{t}$ resonances are interesting because they provide a benchmark for cascade decays containing leptons, jets and missing E_T and they allow to study highly boosted topologies. They can be observed in two complementary channels, which are the di-leptonic and the lepton + jets channels. The lepton+jets channel allows a better mass reconstruction but it suffers from W+jets background and to the loss of the top quark identification capability when the two jets merge. In this channel, b-tagging is fundamental to reduce the huge light flavour jet background. The dileptonic channel cannot measure the resonance mass and suffers from the irreducible $t\bar{t}$ background but it is less susceptible to the top quark jets merging because the leptons are more easily identified when they are close to the b-jet. The increase in sensitivity at HL-LHC depends on the particular resonance mass considered, but it can improve the mass limits by up to 2 TeV.

The *dilepton resonances* study at LHC are a quite challenging sector because of several problematic issues. The detector should, in fact, prevent that high-energy electrons lead to EM calorimeter response saturation due to the readout electronics, maintain a good momentum resolution for high-p_T muons, ensure a proper angular coverage to measure the resonance spin. The main background is the Drell-Yan production, but in the case of di-electron resonances also the jet-misidentification plays an important role. In [2] it is shown that, for Z' resonances, HL-LHC will increase the mass limit by $\sim$1.2 TeV.

1.6 Flavour-changing neutral currents in top decays

In top physics, flavour-changing neutral currents (FCNC) are of particular interest. In the SM, FCNC are suppressed due to the GIM mechanism, with a branching ratio smaller than 10^{-12}. However, several extensions to the SM predict a considerable increase of this branching ratio, up to 10^{-4}. At the moment, LHC experiments are not able to provide a direct measurement of the FCNC branching ratios, and only upper limits have been obtained. In [2], an analysis is described in which the signal is a top quark pair production, where one of the top quarks decays in the dominant channel and the other via a FCNC process ($t \to q\gamma$, $t \to qZ$). For the $t \to q\gamma$ channel, the dominant backgrounds are $t\bar{t}$, Z+jets and W+jets, for the $t \to qZ$ they are $t\bar{t}$, Z+jets and WZ. At HL-LHC, the expected limits at 95% CL are in the range $10^{-5} \div 10^{-4}$, with possible improvements.

$\Delta\mu/\mu$	300 fb^{-1}		300 fb^{-1}	
	All unc.	No theory unc.	All unc.	No theory unc.
$H \to \gamma\gamma$ (comb.)	0.13	0.09	0.09	0.04
(0j)	0.19	0.12	0.16	0.05
(1j)	0.27	0.14	0.23	0.05
(VBF-like)	0.47	0.43	0.22	0.15
(WH-like)	0.48	0.48	0.19	0.17
(ZH-like)	0.85	0.85	0.28	0.27
(ttH-like)	0.38	0.36	0.17	0.12
$H \to ZZ$ (comb.)	0.11	0.07	0.09	0.04
(VH-like)	0.35	0.34	0.13	0.12
(ttH-like)	0.49	0.48	0.20	0.16
(VBF-like)	0.36	0.33	0.21	0.16
(ggF-like)	0.12	0.07	0.11	0.04
$H \to WW$ (comb.)	0.13	0.08	0.11	0.05
(0j)	0.18	0.09	0.16	0.05
(1j)	0.30	0.18	0.26	0.10
(VBF-like)	0.21	0.20	0.15	0.09
$H \to Z\gamma$ (incl.)	0.46	0.44	0.30	0.27
$H \to b\bar{b}$ (comb.)	0.26	0.26	0.14	0.12
(WH-like)	0.57	0.56	0.37	0.36
(ZH-like)	0.29	0.29	0.14	0.13
$H \to \tau\tau$ (VBF-like)	0.21	0.18	0.19	0.15
$H \to \mu\mu$ (comb.)	0.39	0.38	0.16	0.12
(incl.)	0.47	0.45	0.18	0.14
(ttH-like)	0.74	0.72	0.27	0.23

Table 1.1: Relative uncertainty on the signal strength μ for the combination of Higgs analyses at 14 TeV, with 300 fb^{-1} (left) and 3000 fb^{-1} (right), assuming a SM Higgs boson with a mass of 125 GeV and assuming production cross sections as in the SM. For both 300 and 3000 fb^{-1} the first column shows the results including current theory systematic uncertainties, while the second column shows the uncertainties obtained using only the statistical and experimental systematic uncertainties. The abbreviation "(comb.)" indicates that the precision on μ is obtained from the combination of the measurements from the different experimental sub-categories for the same final state, while "(incl.)" indicates that the measurement from the inclusive analysis was used[9].

Chapter 2

ATLAS Detector

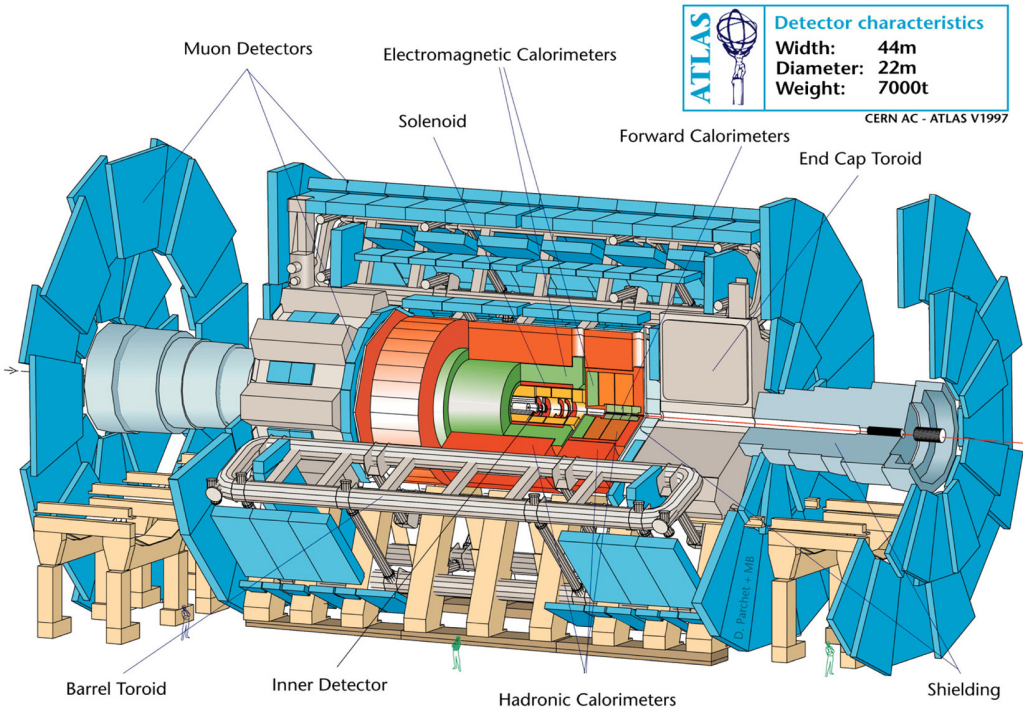

Figure 2.1: Current ATLAS detector.

This section briefly describes the current experimental apparatus, shown in Figure 2.1, and the reasons why it cannot withstand the conditions of HL-LHC.

The ATLAS detector is is a magnetic spectrometer, therefore its components are:

- the **magnet system**;
- the **inner detector**;
- the **electromagnetic calorimeter**;
- the **hadronic calorimeter**;
- the **muon spectrometer**;
- the **trigger system**;
- the **data acquisition system (DAQ)**.

In the following sections these elements are briefly described, outlining the main upgrades that will be applied for the high luminosity phase.

ATLAS uses a coordinate system where the z axis is parallel to the beam line, whereas x and y lie in the transverse plane. It is also common to use a cylindrical coordinate system (r,z,ϕ) and also the variable $\eta = -\log\tan\theta/2$ for directions, where θ is the angle formed with the beam line (see also appendix A).

2.1 The Magnet System

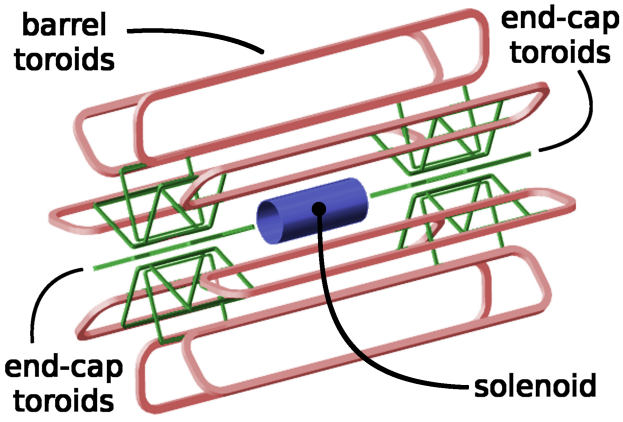

Figure 2.2: ATLAS magnet system[15].

The current magnet system (Fig.2.2) comprises four superconducting magnets[16], for charged particles bending and momentum measurement in

the 8000 m^3 volume of the apparatus.

The *Central Solenoid Magnet* encloses the tracking volume and provides a 2 T magnetic field along the beam axis and minimal thickness in order to reduce the degradation of photon and electron energy resolution in the subsequent calorimeter layers.

The *Barrel* and *Endcap Toroids* provide a tangential magnetic field of about 1 T for the muon detectors, both in the radial and the forward region.

As the current magnet system already matches HL-LHC needs, it will not require an upgrade.

2.2 The Inner Detector

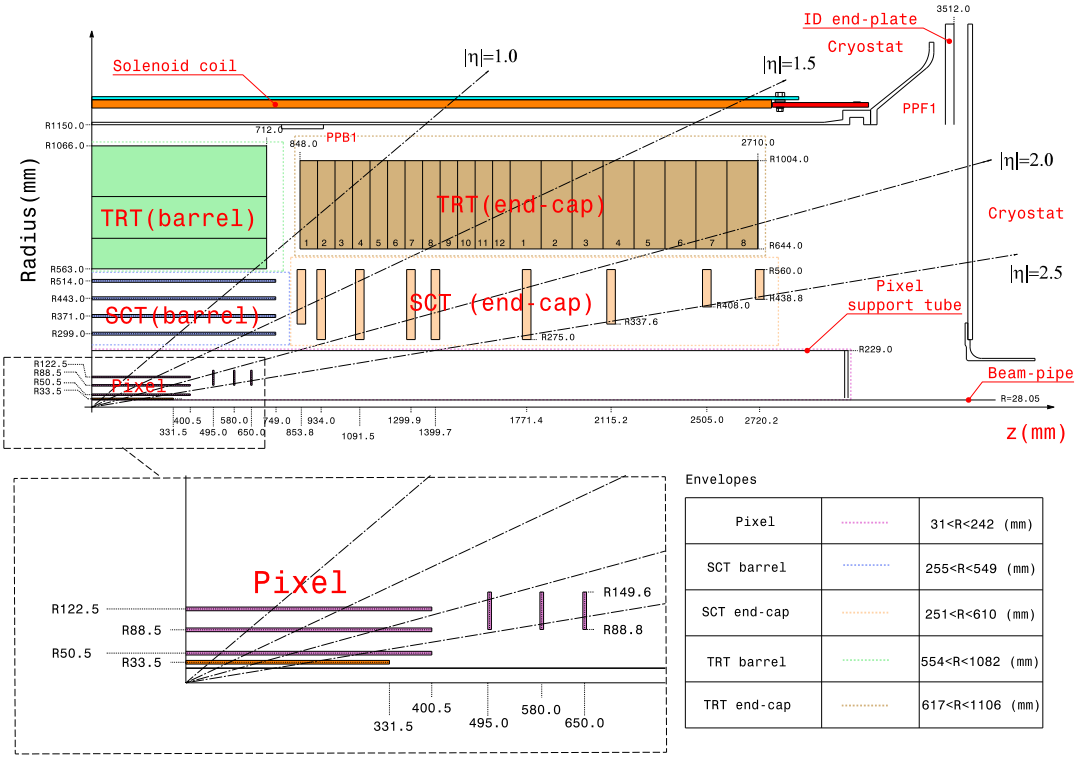

Figure 2.3: ATLAS Inner Detector layout[17].

The ATLAS **Inner Detector** (ID), whose current layout is shown in Fig.2.3, is designed to measure the momentum of the charged particles tracks

with $p_T \gtrsim 500$ MeV and within $|\eta| < 2.5$, with the capability to reconstruct multiple primary vertices, as well as vertices displaced from the primary[17].

The ID is contained in a cylindrical envelope (with the axis along the z-axis) that extends ± 3512 mm in length and 1150 mm in radius. The whole system is placed inside the central solenoid magnet. The ID consists of three sub-detectors: the innermost section provides high resolution pattern recognition and secondary vertexing capability using *silicon pixel layers*, the middle one consists of stereo pairs of *silicon microstrip* (SCT) layers and the outermost one consists of the *Transition Radiation Tracker* (TRT). During 2014 ATLAS upgrade, the *Insertable B-Layer* (IBL), a fourth pixel barrel layer, was added to avoid the decrease of performances after the luminosity upgrade of LS1.

Each one of these detectors is subdivided into a *barrel* ($|\eta| \lesssim 1.0$) region, in which the sensor modules are organized tangentially with respect to a circle around the beam axis and an *end-cap* region, in which they are placed perpendicularly with respect to the beam axis, producing a disk resemblant shape.

The *pixel* barrel layout consists of 3 layers placed at approximate radii 50.5, 88.5 and 122.5 mm with respect to the beam axis. The IBL was added during the LS1 as the innermost pixel layer at radius 33.5 mm. In the end-cap region, three disks per side were chosen, at z position respectively 495 mm, 580 mm, 650 mm.

The *SCT* barrel layout consists of four layers at radii 300 mm, 373 mm, 447 mm and 520 mm. The end-cap region is instead composed by 9 disks per side with variable inner radii and z-position ranging from 850 mm to 2720 mm.

The *TRT* barrel layout is formed by straw chambers parallel to the beam axis at radii from 563 mm to 1066 mm, while the end-cap region consists of radially wound straws with z ranging from 850 mm to 2710 mm. This detector can track particles up to $|\eta| < 2.0$.

Pixel and SCT

The pixel and SCT sensors are designed to maintain their performance during the detector lifetime at nominal luminosity[17]. As the integrated radiation dose has significant consequences on these sensors, they are operated at a

temperature between $-10\ ^{\circ}C$ and $-5\ ^{\circ}C$.

Pixel sensors of the Run-1 ID (thus excluding IBL) are 250 μm thick detectors which are mounted on oxygenated n-type wafers, with the pixel on the n^{+} side. About 90% of the pixel on a sensor have a nominal size of $50 \times 400\ \mu m^2$, while the rest are $50 \times 600\ \mu m^2$ large and are placed at the front-end chips on a module. There are a total of 1744 identical pixel sensors with an external dimension of $19 \times 63\ mm^2$, each composed by 47232 pixels. For reasons of space, there are four ganged pixels on each column of the front-end chip, thus resulting in a total of 46080 readout channels. *IBL pixels* are, instead, $50 \times 250\ \mu m^2$ large to ensure a very precise measurement of the coordinates near the interaction point[18]. Two different technologies have been implemented in the central and forward IBL region, which results in a different sensor thickness and module sizes.

The *SCT* consists of a total of 15912 silicon strips sensors with thickness 285 μm. Each sensor consists of 768 strips of 12 cm length, with average pitch of 80 μm. On each SCT module there are two back-to-back sensors with a relative angle of 40 mrad, which allows the extraction of a second coordinate. The readout electronics is placed at the end of each sensor.

Pixel and SCT system will be completely replaced for HL-LHC, as described in Chap.5.

TRT

The basic elements of *TRT* consist of 4 mm diameter tubes[17]. For both the barrel and end-cap sections, the anodes are made of 31 μm diameter, $\pm$ 71.2 cm active length tungsten wires connected to the front-end electronics and grounded. The wires are carefully aligned within the straw, with a maximum tolerance of 300 μm. The barrel section contains about 50000 straw tubes, whereas the end-cap contains approximatively 320000, for a total of 420000 electronic channels[19]. This detector typically provides an almost continuous tracking of the particles traversing it, with an average of 36 measurements per track.

Due to the strict requirement of HL-LHC, the TRT will be removed, and its space will be allocated to the new Inner Tracker (ITk), which is the main focus of this thesis and will be described in detail in Chap.5.

2.3 Calorimeter system

The ATLAS experiment relies on an electromagnetic and a hadronic calorimeter to identify and measures energies and direction of photons, electrons, hadrons, jets and neutrinos. Both compartments are divided into a central and a forward region (Fig.2.4). The electromagnetic calorimeters are based on the liquid Argon technology, whereas the hadron calorimeters are either liquid Argon (forward region) or tile calorimeter (central).

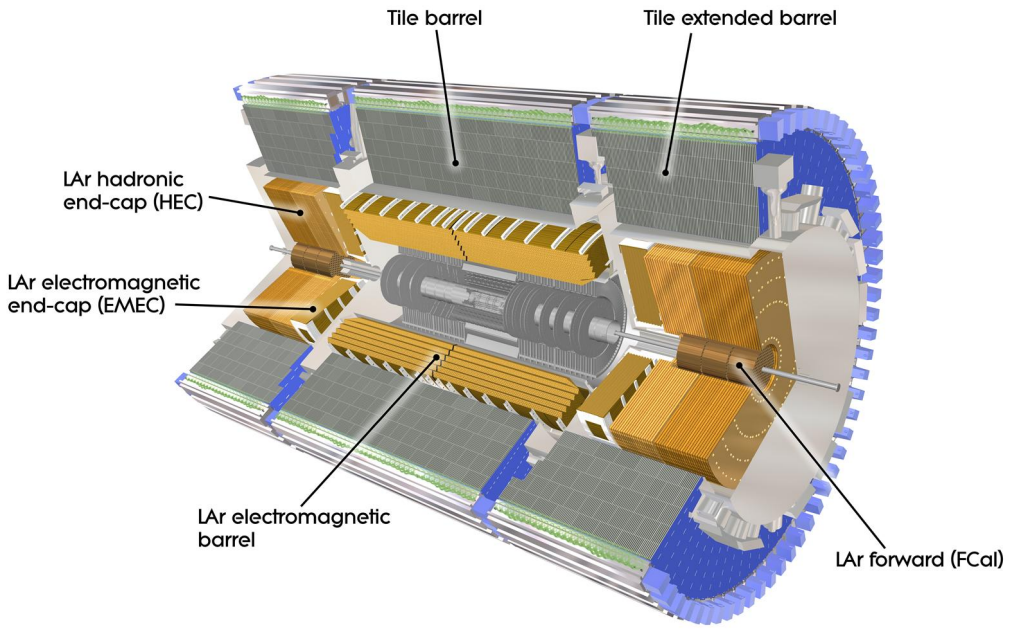

Figure 2.4: ATLAS Calorimeter System.

Liquid Argon Calorimeters

Several components of the ATLAS calorimeter use Liquid Argon (LAr) as active medium[20]. The electromagnetic barrel and endcap (EMEC) are entirely built this way, but also the Hadronic Endcap Calorimeter (HEC) and the Forward Calorimeter (FCal).

The **electromagnetic calorimeter** uses lead as absorber and is designed to trigger on and to provide precision measurements of electrons, photons, jets, and missing E_T . The full cryostat of the *barrel section* is 6.8 m long,

with the inner and outer radius being respectively 1.15 m and 2.25 m and ranges in $|\eta|$ from 0 to 1.7. The *endcap section* consists of two concentric wheels, the larger one ranging in $|\eta|$ from 1.4 to 2.5, the smaller from 2.5 to 3.2. In addition, a *presampler* layer was inserted behind the cryostat wall to correct for the losses in the upstream material. Detailed studies based on the response to high energy photons and electrons measured the thickness of the calorimeter to be about 24 X_0 in the barrel and 26 X_0 in the endcap. Each section is physically divided into longitudinal projective towers which produce the signal and are so responsible for the granularity of the calorimeter. High granularity is especially required in the central regions, where it reaches the value of $\Delta\eta \times \Delta\phi = 0.025 \times 0.025$. Hermeticity is also a very important feature for the measurement of missing E_T and has been maximized using a transition gap detector between the barrel and endcap cryostats.

HEC[21] is a sampling calorimeter with copper absorber plates and consists of two wheels of outer radius 2.03 m, made of 32 identical modules. It ranges in $|\eta|$ from 1.4 to 3.2 and every half of it shares the cryostat with the EMEC and FCal. The thickness of the active part of the calorimeter is about 12λ.

FCal has to cope with a high level of radiation, which makes it a particularly challenging detector. The high material density employed allows to reach the required 9.5λ in a reduced space and to minimize the endcap calorimeter pileup signal.

Hadron Tile calorimeters

The main requirement for the **Tile Calorimeter** is to reconstruct the energy of the jets produced and, due to the large center-of-mass energy at LHC, it must provide good response in a large energy range. Also thanks to the use of an extended barrel, the HEC, together with the FCal, is able to provide a good p_T^{miss} reconstruction.

The Tile calorimeter is a sampling calorimeter composed by alternated layers of scintillating tiles (used as active medium) and steel (as an absorber). The signal is transmitted from each module using optical fibres, which can then run through the calorimeter. It is segmented with a granularity of $\Delta\eta \times \Delta\phi = 0.1 \times 0.1$.

This calorimeter is composed by one barrel (5.64 m long) and two exten-

ded barrel (2.91 m long) parts, with a gap of 60 cm in between. It consists of a cylindrical structure of inner radius 2.28 m and 4.23 m. The barrel covers the region $0 < |\eta| < 1.0$ whereas the extended barrel covers the region $0.8 < |\eta| < 1.7$. The overlap region from 0.8 to 1.0 is occupied by the Intermediate Tile Calorimeter (ITC). The three longitudinal layers are approximately 1.4, 4.0 and 1.8λ thick.

Upgrade of the electromagnetic calorimeter

The performance requirement of the barrel electromagnetic calorimeter during the high luminosity phase will not change, thus no major change is foreseen. In contrast to that, the FCal performances will be degraded by the conditions of HL-LHC.

In the Reference Scenario of the ATLAS Scoping Document[1] the replacement of the current FCal with a high-granularity Small-Gap Forward Calorimeter (sFCal) is foreseen. Its design has better performances with respect to the current one thanks to smaller LAr gaps. The improved granularity will also be helpful with the new tracker. Furthermore, the addition of a High Granularity Timing Detector (HGTD) is planned, which will be hopefully installed in front of the LAr Calorimeter endcaps and will be needed to deal with the pile-up. It will cover the range $2.4 < |\eta| < 4.3$ measuring the arrival time of charged particles, assigning them to different collision vertices. The readout electronics will also be upgraded due to insufficient radiation tolerance and inadequate performances for the requirements of the upgraded trigger. In the Middle and Low cost scenarios, on the contrary, no upgrades in the endcap and forward region are foreseen, unless new issues arise.

Upgrade of the Tile Calorimeter

The Tile Calorimeter maintains the required performance even during the HL-LHC phase and so it does not need replacement. However, the readout electronics will be upgraded due to limited radiation tolerance and to accommodate the new trigger requirements in terms of rates and latencies. This will be fulfilled, as in the case of the LAr, by substituting the on-detector front-end electronics, the optical links, the off-detector signal processing unit, the powering system and the interface modules to the TTC and DAQ systems. R&D is ingoing to verify that the current photomultipliers can survive

the radiation dose.

2.4 Muon Spectrometer

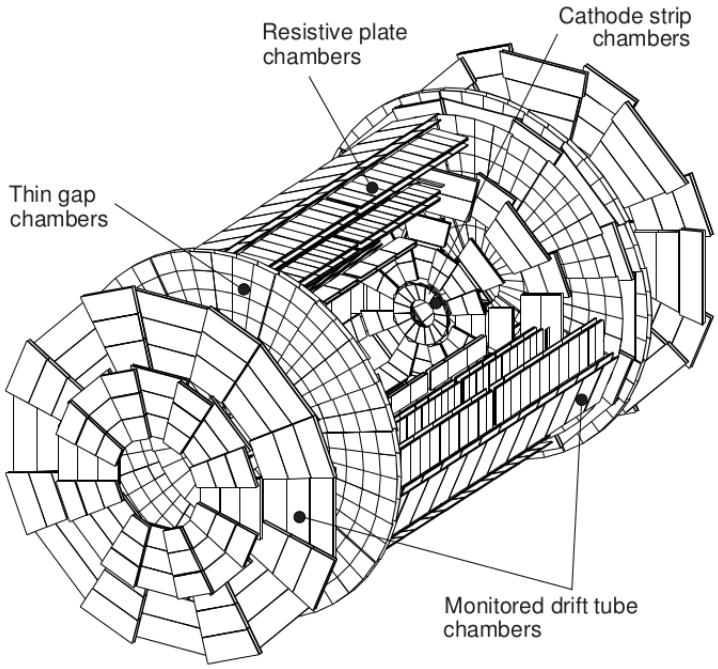

Figure 2.5: ATLAS Muon System[22].

The ATLAS **muon spectrometer** is designed to track charged particles that manage to pass through the whole calorimetric system, and to perform stand-alone measurements of their momentum, in the range 3 GeV $< p_T <$ 3 TeV. Even at the upper limit, the detector is still able to provide adequate momentum resolution and charge sign measurement[22][17].

The layout of the current ATLAS muon spectrometer is shown in Fig.2.5. It is divided into three main regions of pseudo-rapidity: in the range $|\eta| < 1.0$ the bending power is provided by a barrel magnet composed by eight coils; the region $1.4 < |\eta| < 2.7$ is covered by a pair of *end-cap toroids* placed at the tips of the barrel toroid; the *transition region*, $1.0 < |\eta| < 1.4$, is

covered by a combination of the two. The system is built so that it provides a field that is mostly orthogonal to the particle direction while minimizing the contribution to multiple scattering. A *trigger system* is also available for $|\eta| < 2.4$.

In the barrel section tracks are measured by stations arranged in three concentric cylinders (approximately 5 m, 7.5 m and 10 m radius) while in the end-cap and transition region other three stations are arranged in disks along the z-axis (approximately at $|z| = 7.4$ m, 10.8 m, 14 m and 21.5 m). An extra disk is added in the transition region to increase acceptance. A gap in the region $|\eta| < 0.1$ is necessary to allow for services. The layout is designed so that a track coming from the interaction point can traverse only three of the aforementioned stations.

Four different detector technologies are employed in the current layout to optimize momentum reconstruction and trigger efficiency in the different regions. *Monitored drift tube chambers*(MDT) are employed in the barrel and endcap regions (except in the innermost endcap layer, where the particle flux is maximum) to provide precise z coordinate measurement in the bending plane. In the innermost endcap layer, instead, *Cathode Strip Chambers*(CSC) are used to provide $R - \phi$ and time measurements. For the muon trigger system, *Resistive Plate Chambers*(RPC) are used in the barrel region, while *Thin Gap Chambers*(TGC) were chosen for transition and endcap regions. Besides, they also provide a measurement of the coordinate in the non-bending plane to the MDTs.

Upgrade of the muon spectrometer

During the HL-LHC upgrade, the huge increase in the average number of pileup events leads to a number of difficulties that must be overcome by a corresponding improvement of the performances[1].

In particular, the innermost endcap layer will be replaced by *New Small Wheels*(NSW) that combines small strip TGCs and MicroMegas chambers, both for triggering and precision tracking. The MDT, together with the New Small Wheel, should already be able to provide an adequate performance and will not be substituted. Its read-out electronics, instead, will not be able to cope with the high hit rate and the new ATLAS L0/L1 trigger scheme, so it will be replaced. The same also applies to the RPC and TGC. In the case of RPC, moreover, the gas gain will be lowered to ensure safety in the expected high rate environment and protract its life. New RPCs with increased rate

capabilities will be located in the innermost barrel layer to maintain a good trigger efficiency, while new high resolution TGC will replace the present ones in the middle endcap disk to keep fake rate at a minimum.

The possibility to extend the coverage to $|\eta| < 4$ to identify muons and tag inner detector tracks in that range will be obtained by inserting micro-pattern gaseous or silicon pixel detectors in the region $2.7 < |\eta| < 4.0$.

2.5 Trigger and DAQ system

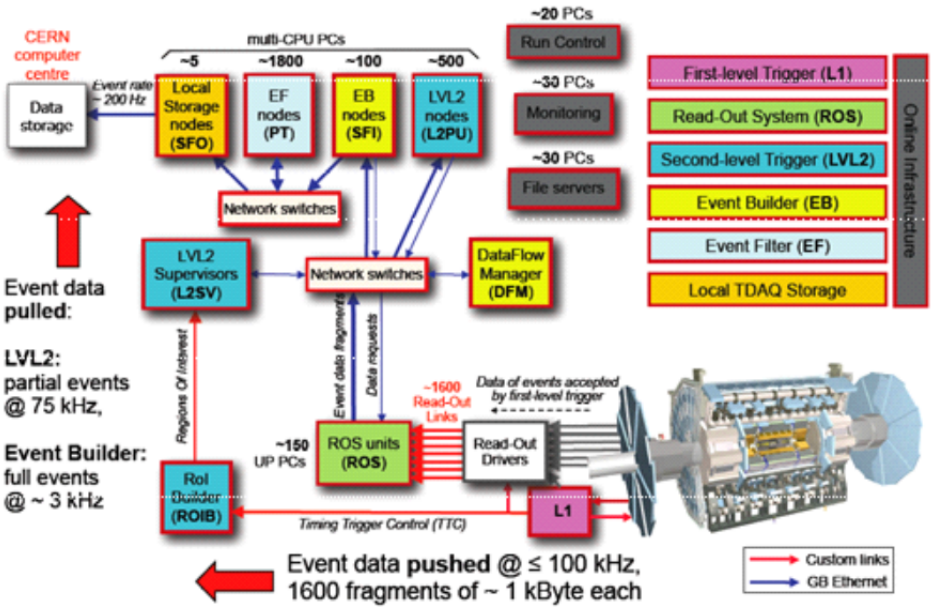

Figure 2.6: ATLAS Trigger and DAQ System[23].

The current ATLAS **trigger system** is structured in three levels of event selection: *Level 1* (L1), *Level 2* (L2) and event filter[17]. The L2 trigger, together with the event filter, form the *High-Level Trigger* (HLT). Due to the high level of integration between the trigger and the DAQ system they are sometimes referred as a single system (TDAQ).

At LHC, a bunch crossing takes place every 25 ns (therefore with a frequency of 40 MHz). Crossings in which a collision is identified generate a "trigger" signal to the whole TDAQ. The goal of L1 trigger is to search for signatures from high p_T muons, electrons, photons, jets and τ decaying into

hadrons. It also searches for events with large E_T^{miss} or large E_T. It manipulates reduced granularity data coming from the muon spectrometer (RPCs and TGCs) and calorimeters. L1 trigger is designed to work without dead time with an accept rate of 100 kHZ, with a latency of 2.5 μs. A *Central Trigger Processor* applies the selection and, if the event passes it, the data is sent to the DAQ and to the *RoI*[1] *Builder*, which computes the regions of interest for the next trigger level.
L2 trigger is designed to select events so that the event rate is reduced from the 100 kHz of the L1 trigger to 3.5 kHz, with an average processing time of 40 ms per event, by exploiting a distributed architecture. This trigger level takes as input the regions of interest from the L1 trigger as input and send a data request to the DAQ network, based on these RoI. A quick reconstruction is performed distributing the information among the nodes and a selection is applied. If an event passes this selection is then sent to the *event filter*, which applies a more sophisticated selection (similar to the offline) with high latency, taking the event rate from 3.5 kHz to $\approx$ 200 Hz, which are stored in a permanent memory area by the DAQ system.

Upgrade of the TDAQ system

The trigger system and electronics were designed to operate at the initial luminosity $\mathcal{L} = 10^{33}$ cm^{-2}s^{-1} at low trigger thresholds and at the Run2 luminosity, $\mathcal{L} = 10^{34}$ cm^{-2}s^{-1}, with higher thresholds[1].

Tp cope with the increase of the luminosity to $\mathcal{L} = 2 - 3 \cdot 10^{34}$ cm^{-2}s^{-1} during the Phase-I upgrade and then to a maximum of $\mathcal{L} = 7.5 \cdot 10^{34}$ cm^{-2}s^{-1}, the entire TDAQ system will have to be significantly improved. During the Phase-I upgrade the New Small Wheels will be installed, together with a finer granularity calorimeter trigger and the L1 trigger will become more selective, with the goal of keeping the latency and the accept rate unchanged. During this phase also the *Fast TracKer trigger* (FTK)[24], which will perform full tracking on the events accepted by the L1 trigger, will be installed.

During the HL-LHC phase, when the luminosity will reach its maximum, it will be necessary to increase the maximum rate and latency of the trigger system and install an additional Level 0 hardware trigger (L0), which will be based on the muon and calorimeter trigger information. The L0 trigger is designed to decrease the data flow from 40 MHz to 1 MHz, with a maximum latency of 6 μs. The upgraded L1 trigger will be seeded by the

[1] Region-of-interest

regions of interest (RoIs) provided by the L0 trigger and it will use full calorimeter readout with higher-granularity data. It is designed to operate with a maximum latency of 30 μs and an accept rate of 400 kHz (in the Reference scenario of the *Scoping Document*[1]). The Phase-II DAQ system is designed to make efficient use of commercial networking and computing hardware.

Chapter 3

Physics objects reconstruction

Every analysis in the ATLAS experiment starts from the reconstruction of physics objects based on the features of the signals coming from the different sub-detectors[25]. In this section we briefly summarize how physics objects are reconstructed in ATLAS. Given the relevance of muons in this thesis, they will be described in more detail.

3.1 Track reconstruction algorithm in the ATLAS ID

The first important step to identify physics objects in the ATLAS experiment is the track reconstruction process based on the Inner Detector data. Charged particles that traverse the ID produce hits which are then used for track reconstruction. The *baseline* track reconstruction algorithm[26] used during Run-1 is briefly described below.

The track reconstruction process takes place in two phases: the first one starts with a so called *inside-out reconstruction* that uses the data from the Pixel Detector and the SCT; the last phase is an *outside-in reconstruction* that uses the TRT measurements.

Inside-out reconstruction

The inside-out reconstruction starts with the conversion from raw data to 3D measurements called *space points*. In the Pixel Detector, a space point is computed by considering only one cluster; in the SCT a space point is

obtained by combining the clusters of both sides of the layers.

In the Pixel Detector it is possible to measure the distribution of the energy loss, so a complex algorithm was developed to fully benefit from this information. The total charge is often distributed among different pixel sensors and strongly depends on the incidence angle of the particle with respect to the sensor. Clusters are formed by grouping pixels that have a common edge or corner and then the space point is obtained by using a charge interpolation technique. If two particles are very close to each other, it is possible that they generate a measurable signal in side by side pixels, which result in the formation of a *merged cluster*. An artificial neural network is then implemented to identify these clusters, and attempt to split them.

Once the space points have been reconstructed, *seeds* are formed by combining three space points taken either from the Pixel Detector or the SCT. The track parameters (q/p_T, d_0, z_0, η and ϕ, see A) are estimated for each seed, assuming a helical trajectory in a uniform magnetic field, and the seeds are finally combined to build track candidates with limited resolution. At this point, the track candidates pass to the *ambiguity solver*. During this phase they are sorted based on a score which measures track quality weighing intrinsic resolution, χ^2, holes (sensors that have not produced a signal but should have because the fitted track traverses them) and momentum (high momentum tracks are promoted). A limit in the number of shared clusters is also imposed. Track candidates passing the previous step are fit with full resolution and added to the track collection.

Outside-in reconstruction

This second phase starts with the identification of straight line patterns in the TRT detector and uses hits which have not been already chosen. Track candidates are then passed to an ambiguity solver analogous to the one of the inside-out reconstruction phase. Segments obtained this way are extrapolated to the silicon detectors and a full track fit is performed if a match is found. Conversely, if no acceptable silicon tracks are found during the extrapolation, the track candidates become *TRT-only tracks*.

The outside-in reconstruction is particularly important to reconstruct tracks from neutral particle decays ($K^0 \to \pi^+\pi^-$ or $\Lambda^0 \to p\pi^-$), conversion electrons and bremsstrahlung electrons, and all cases in which tracks do not have produced enough hits in the silicon detector.

In ITk (Chap.5) the TRT is not present, which has led to a necessary revision of the tracking algorithm. However, the general idea is basically the same: the pattern recognition starts from seeds in the outer SCT layers, going backwards towards the interaction point[27].

3.2 Muon identification

In the ATLAS experiment, muon momentum is measured independently in the ID and in the Muon Spectrometer (MS). The identification efficiency is $> 95\%$[25] in the range $|\eta| < 2.7$. Muons also produce a minimum ionization signal in the calorimeters.

Reconstruction in the MS

In the MS, muon reconstruction starts by finding combination of hits in each muon chamber to form segments performing straight-line fits. Track candidates are then built by fitting the segments together[28], starting from the middle layers (which typically have more hits) and looking for seeds in the remaining layers that match the position and angle of the segment. An *overlap removal* algorithm finally selects the best candidate among those formed starting from the same segment, removing hits that decrease the fit quality if necessary.

Combined reconstruction

Four muon types are defined depending on the subdetectors used in the reconstruction.

- *Combined muons* (CB) are reconstructed independently in the ID and MS. A global fit is performed by combining the hits from both subdetectors, adding or removing hits to increase the fit quality. Usually a match between the ID and MS is found by extrapolating the MS track candidate to the ID, thus following an outside-in approach;
- *Segment-tagged* muons (ST) are reconstructed in the ID and identified as muons if there is at least one matching track segment in the MDT or CSC chambers. ST muons are used when muons only traverse one layer of the MS, typically because they have low transverse momentum or they fall in a low MS acceptance region;

- *Calorimeter-tagged* muons (CT) are tracks in the ID which are matched to a calorimeter deposit compatible with a minimum-ionizing particle. This muon type has the lowest purity of all, but it is useful to recover acceptance where the MS is only partially instrumented, like in the region $|\eta| < 0.1$;

- *Extrapolated* muons (ME) are MS-only muons with a loose requirement on compatibility with a particle originating from the interaction point and different requirements on the number of crossed layers depending on the pseudo-rapidity region. ME muons are mostly useful to recover acceptance in the region $2.5 < |\eta| < 2.7$, where the ID is not present.

Events in which more than one type can be identified are solved by giving preference to CB muons, then to ST and finally to CT. Ambiguities involving ME muons are solved by selecting the track with better fit quality and larger number of hits.

Muon identification

In ATLAS, prompt muons or muons coming from W/Z decays are considered as *signal*, while muons coming from in-flight decays of light hadrons (mainly pions and kaons) are considered *background*. Muon identification is performed by applying track quality requirements that suppress background. Variables used in CB tracks are:

- *q/p significance*, defined as the absolute value of the difference between the q/p ratio as measured in the ID and the MS, divided by the sum in quadrature of the corresponding uncertainties;

- $\rho^{'}$, defined as the absolute value of the difference between the p_T measurement in the ID and MS divided by the p_T of the CB track;

- χ^2/DOF of the combined track fit;

- number of hits in the Pixel, SCT and TRT systems.

Four identification selections are provided that deal with different physics analyses:

Loose This identification uses all muon types and is designed to increase the efficiency while providing good-quality tracks and it is optimized for the reconstruction of muons in the $H \rightarrow 4l$ channel. All CB and ME muons that can also identified as *medium muons* are included in this category, whereas CT and ST muons are restricted to the $|\eta| < 0.1$ region;

Medium This is the default selection for muons in ATLAS, that minimises the systematic uncertainties on muon reconstruction and calibration. Only CB and ME muons are used, with different requirements on the number of hits in the MS. A requirement on the q/p significance is also present;

Tight This identification guarantees a high purity (losing some efficiency). Only CB muons that pass the medium selection and satisfy additional requirements on the number of hits in the MS, $\rho^{'}$, q/p and χ^2/DOF are included.

High p_T This identification is aimed at maximising the momentum resolution for tracks with $p_T > 100\ GeV$ and it is optimized for high-mass resonances searches. These muons are required to pass the Medium selection, with an additional requirement on the number of hits in the MS.

The Loose, Medium and Tight selections are inclusive, so a muon passing the Tight selection also pass the Medium and the Loose. With increasing the level of the selection, the efficiency decreases while the purity increases, as can be seen in Tab.3.1

Selection	$4 < p_T < 20$ GeV		$20 < p_T < 100$ GeV	
	ϵ_{μ}^{MC} [%]	$\epsilon_{Hadrons}^{MC}$ [%]	ϵ_{μ}^{MC} [%]	$\epsilon_{Hadrons}^{MC}$ [%]
Loose	96.7	0.53	98.1	0.76
Medium	95.5	0.38	96.1	0.17
Tight	89.9	0.19	91.8	0.11
High-p_T	78.1	0.26	80.4	0.13

Table 3.1: Efficiency for prompt muons from W decays and hadrons decaying in-flight and misidentified as prompt muons computed using a $t\bar{t}$ MC sample[28]. The results are shown for the four identification criteria separating low and high momentum muons for candidates within the ID acceptance.

Muon identification in this analysis

The analysis on the $H \rightarrow ZZ^* \rightarrow 4\mu$ channel presented in this thesis uses the simulated data coming from ITk exclusively, so there is no information coming from the muon spectrometer. We chose to make the hypothesis of 100% identification efficiency of the muons that pass a track quality selection

and with a minimum p_T, as will be described in Chap.6. Considering the efficiencies shown in Tab.3.1 and the fact that for this channel a loose muon identification was chosen for Run-1, these assumptions appear reasonable.

3.3 Electrons and photons

Electrons and photons produce a very similar energy release in the electromagnetic calorimeter and are typically completely absorbed before reaching the hadronic calorimeter for a broad range of energies. The electron identification can be achieved by looking for a track in the Inner Detector that points to the calorimeter energy release and has a momentum compatible with the calorimeter energy measurement. For both particles, several levels of selection are defined that apply increasingly more stringent requirements, based on track quality and cluster-track matching variables (for the electron only), lateral and longitudinal shower shape and energy leakage in the hadronic calorimeter (for both particles). In the forward region ($2.5 < |\eta| < 4.9$) the selection can only rely on calorimeter information and the discrimination against hadrons is achieved by considering shower shape and cluster moments variables. An in-situ fine tuning of the electromagnetic energy scale is performed at ATLAS by measuring the well known Z mass in the decay $Z \to e^+e^-$.

3.4 τ identification in hadronic decay channels

The τ lepton, being much heavier than the electron, does not radiate appreciably and, due to its relatively long lifetime, can cover a significant space before decaying, resulting in the identification of a secondary vertex. The hadronic decay channels of the τ lepton with larger branching ratio are the one-prong and three-prongs decays with charged and neutral pions, and neutrinos. The identification is based on the characteristics of the jets emitted from quark or gluons, such as low track multiplicity, collimated energy deposits, secondary vertex displacement (for the three-prong decay). The discrimination against electrons is based on the analysis of the longitudinal energy distribution.

3.5 Jets

In ATLAS, as quarks and gluons hadronize into showers of particles (called *jets*), it is important to reconstruct this object. Jets are reconstructed starting from topological energy clusters built from calorimeter cells. These clusters are then split based on the position of local maxima and calibrated using local properties such as energy density, calorimeter depth, and isolation. Thanks to these variables the jets are classified as electromagnetic or hadronic. The reconstructed jets are then corrected to account for the extra energy released by pileup particles, as well as other effects (Z vertex position, calorimeter energy calibration, quark/gluon fragmentation effects etc.).

3.6 Neutrino identification

In a collinear collision such as that of the protons in LHC, the momentum conservation implies the transverse component of the momentum of all the collision products to be zero. By measuring the energy released in the calorimeter, and in the hypothesis that the particles emitted are highly relativistic, it is possible to measure the missing transverse energy. Neutrinos do not interact in the detector, and are characterized by missing energy. Therefore, missing transverse energy is used as a tag of their presence in events of interest. The measurement of the missing transverse energy relies on the calibration of the physics objects, as described in Chap.3.5. The performance and uncertainties are evaluated by comparing the data and simulation of processes like $Z \to ll$ and $W \to l\nu$. The pileup suppression algorithms make the resolution mostly independent on the number of pile-up events. Also muons can produce missing transverse energy as they release minimum ionization energy traversing the calorimeter. If a muon is identified, then missing transverse energy is corrected for its energy as measured in the spectrometer.

Chapter 4

Overview of the simulation technique

Full Monte Carlo simulations are typically performed considering a physical process of interest and simulating it through the whole detector. As the goal of this thesis is to analyse and compare the performances of several ITk configurations in a way that is independent from the other sub-detectors, only the tracker is simulated. This is ideal for tracking studies, in which we are interested only in the response of ITk, but somewhat limits the potential of the analysis of physics processes because of the small number of physics objects that can be reconstructed with the tracker only (muons, charged pions and kaons, photon conversion). Furthermore, no particle identification is possible without the other sub-detectors, so some hypotheses must be done on the identification efficiency and rejection power. As already mentioned in the introduction of this thesis, the HL-LHC environment is particularly challenging due to the very high number of average proton-proton collisions per bunch crossing (~ 200). Thus, full ITk simulation including all the tracks is computationally challenging and the production of samples of this kind with acceptable statistics is very difficult to achieve.

In this thesis, a fast simulation technique that significantly reduces the computational time necessary to produce the samples was developed and applied to single particle ("particle gun") and to the $H \to ZZ^* \to 4\mu$ channel. In this section, the standard and fast simulation technique are described. Before discussing the simulation, we describe one of its main ingredients, the pile-up events.

4.1 Overlapping events

Besides the products of the proton-proton collision of interest, other particles can traverse the detector, resulting in an overlap of signals. The term *pile-up event* refers to an occurred proton-proton collision different from the one of interest. At LHC, two sources of pile-up are present:

- in-time pile-up;
- out-of-time pile-up;

Other overlaps are caused by particles that are not direct products of the bunch collisions and include:

- cavern background;
- beam halo;
- beam-gas collision;
- cosmic background.

In-time pile-up

An HL-LHC bunch will consist of about 10^{11} protons. The elementary proton-proton collisions that take place in the same bunch of the hard-scatter event of interest constitute the *in-time pile-up* events. These events are essentially inelastic proton collisions and are modelled by the so called *minimum-bias* events, which were simulated using the Pythia generator (see appendix B), whose parameters are tuned to reproduce ATLAS data. These events are the most important source of pile-up in the tracker and the only taken into account in the study presented in this thesis.

Out-of-time pile-up

The whole HL-LHC proton beam will consist of approximately 2800 bunches colliding every 25 ns. The time response of some of the sub-detectors is much longer than 25 ns, and the electronics integrates over more than one bunch-crossing. This effect is particularly important in the Liquid Argon detectors, where the integration time is around 250 ns[29]. The tracker is less susceptible to this kind of pile-up events, therefore this effect was neglected in this study.

Cavern background

During an LHC run, the experiment cavern is filled with thermal neutrons and photons with energy below ~ 1 MeV which can produce hits in the muon chambers. This background was not very relevant in LHC, but it could be in the luminosity upgrade phase[29].

Beam halo

These events come from the collision of protons with collimators upstream of the interaction point. They typically consist of muons and produce a quite characteristic signal (for example, they are out-of-time), so are normally easily removed. They are mainly seen by the muon chambers and sometimes can leave a measurable signal in the calorimeter[29].

Beam-gas events

These events arise from the collision of protons with the residual gas in the beam-pipe. These collisions are highly asymmetric and produce a clear signature, with a vertex way outside of the interaction region and an out-of-time signal, so that they are not typically simulated[29].

Cosmic background

Cosmic high-energy muons or air shower can reach the ATLAS cavern and produce a signal in the detectors. They normally have a clear signature because they are out-of-time and have a high impact parameter, but they can sometimes be mistaken as high energy jets and fake SUSY or other physics signals[30].

4.2 In-time pile-up study

The transverse momentum, pseudo-rapidity and azimuthal angle distribution of the pile-up particles reconstructible by ITk is shown in Fig.4.1, as simulated by Pythia (see appendix B).

Particles with the following features are excluded from these plots:

- particles not in the final state (e.g. partons before showering and/or hadronisation);

- neutrons and neutrinos;
- particles with $p_T < 500$ MeV.

The particle composition of the pile-up events after the selection is as shown in Fig. 4.2. Particles belonging to the soft part of the pile-up ($p_T < 500$ MeV) are numerically more consistent but they are not reconstructed as tracks by ITk. However, they can travel in spirals around the detector layers or, more generally, traverse the detector sensors at an angle very different from 90 degrees and produce hits that can become problematic for the pattern recognition, increase the fake rate and deteriorate the tracking performances.

The number of hard pile-up particles produced in a proton-proton collision passing the selection is very high (42, on average), half of which consists of charged pions. A geometrical acceptance of 67% for the minimum-bias events was computed from the η distribution, taking into account the number of particles that lie inside the region $|\eta| < 4.0$, thus resulting in $\simeq 15$ charged pions per proton collision in the acceptance.

Considering an expected average number of pile-up events per bunch-crossing of 200, an average number of 3000 charged pion tracks per bunch-crossing is expected at ITk. Due to the very large number of particles exiting from the collision points, and to the generation of secondaries in their interactions, the time needed to perform a full simulation of each event becomes too large. As of today, small ITk full simulation samples are mainly available for tracking studies. In the following section a faster simulation method is presented.

4.3 General structure of an ATLAS simulation

A typical ATLAS simulation consists in four steps, as described in Fig.4.3.

During the **generation** step the proton-proton event of interest is first generated with the Monte Carlo (or custom) generator of choice. The collision is typically generated at the ATLAS interaction point and the so obtained vertices are then smeared to account for the beam shape. The pile-up events are also generated, typically with the Pythia Monte Carlo generator. The outputs are saved in the HepMC format.

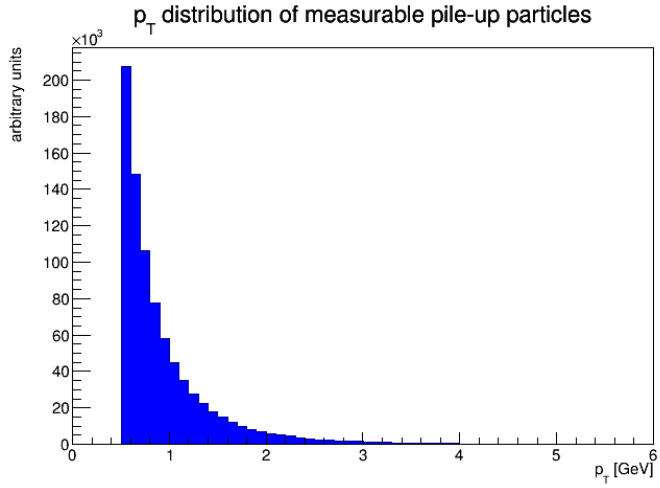

(a)

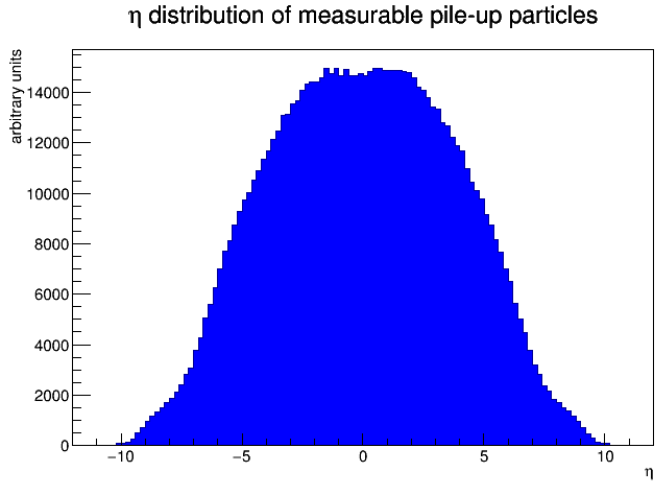

(b)

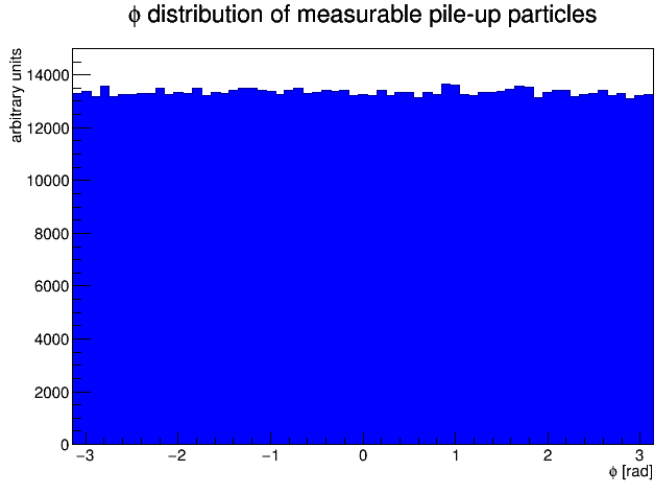

(c)

Figure 4.1: p_T, η and ϕ distribution of the pile-up particles reconstructible as tracks by ITk.

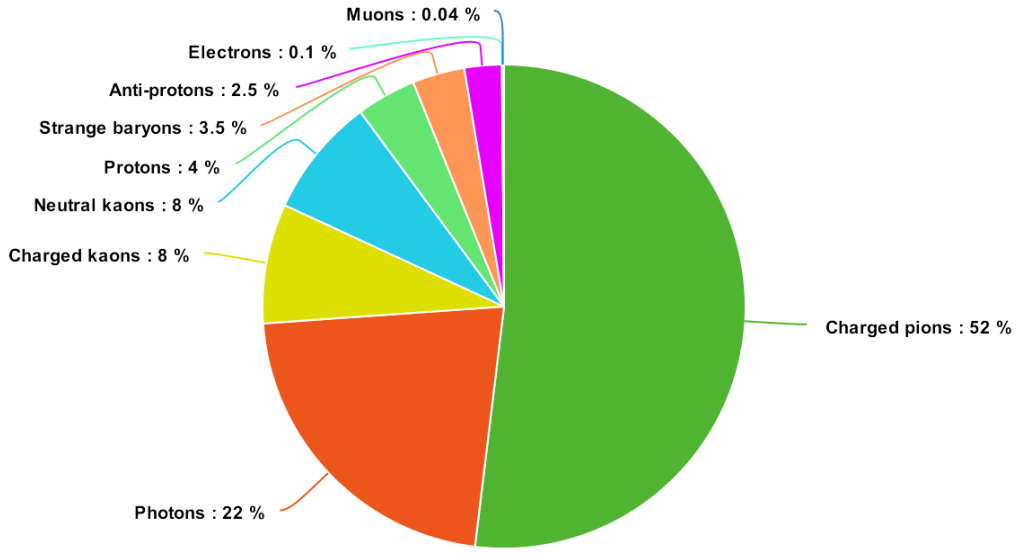

Figure 4.2: Pile-up particle composition after the p_T selection and excluding stable neutral particles.

During the **simulation** step the HepMC files are taken as input, together with the detector description complete of all detector and passive materials and services. The Geant4 package[31] is used to simulate the interaction of each particle with the material, the decays and the magnetic field. This step concludes with the production of a HITS file, that contains the detector physical hits with a measure of the released energy, together with the generation information. After the generation, this step is normally the one that requires the longest computational time to process because of the complexity and the large number of physics processes that have to be emulated.

The **digitization** step takes the HITS file as input and simulates the response of the detector and the readout electronics as ADC counts. The output of this stage is a Raw Data Object (RDO) file that is essentially identical to the raw data produced during a real ATLAS data taking, except that it carries the information from the generation stage. The pile-up events are generated and simulated separately from the physics events and then incorporated during digitization.

Finally, the **reconstruction** step takes the RDO file as input and implements the reconstruction algorithm on the raw data. The results are stored in different file formats depending on the specific user needs[32]. For what

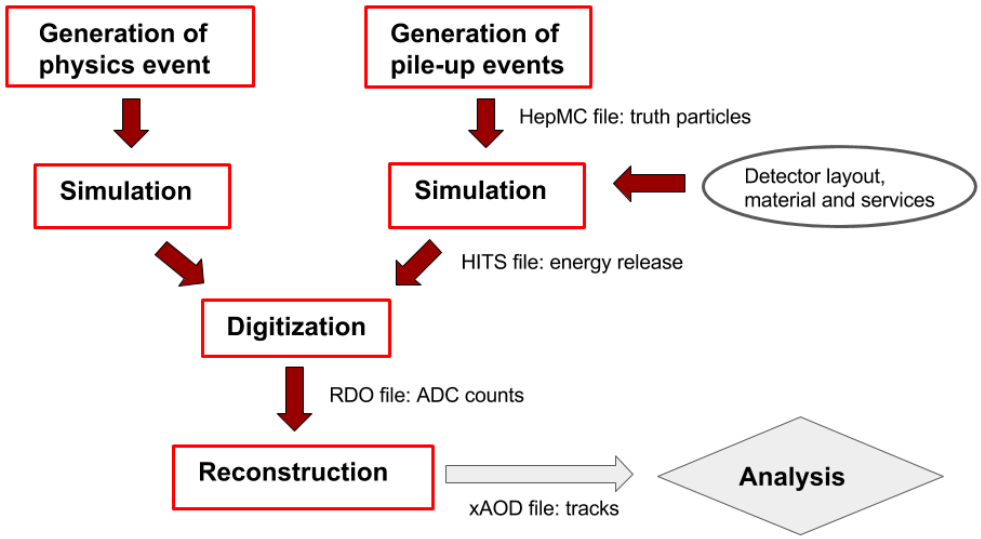

Figure 4.3: The ATLAS simulation flow.

concerns the analysis presented in this thesis, the output file produced in this stage in an xAOD file, which contains information suitable to specific analyses and it is readable by the ROOT framework[33] and within the ATHENA framework[34], and is (since the start of Run-2) the ATLAS standard. This file contains both the information on the primary and secondary particles (*truth* level) and the reconstructed tracks parameters (*reco* level).

4.4 The fast simulation method

This method, based on an original idea by S. Tsuno[35], has, as its main goal, to study the effects of the on-time pile-up on the ITk performances and it is based on the identification of the regions-of-interest (RoIs) at **generation level**. Particles lying outside a RoI are not simulated, thus drastically reducing the time required by the simulation/digitization/reconstruction stages.

The RoIs are computed by selecting the pile-up particles that lie inside a cone with fixed radius ΔR[1] $= 0.1$ around the hard-scattering particles. The value was chosen as it is typical of isolated tracks in ATLAS and the same concept of RoI is already part of the ATLAS trigger. The dependency of the

[1] $\Delta R = \sqrt{\Delta\eta^2 + \Delta\phi^2}$

results on this parameter was studied in Chap.5.9.1. A visual representation of the method is depicted in Fig.4.4.

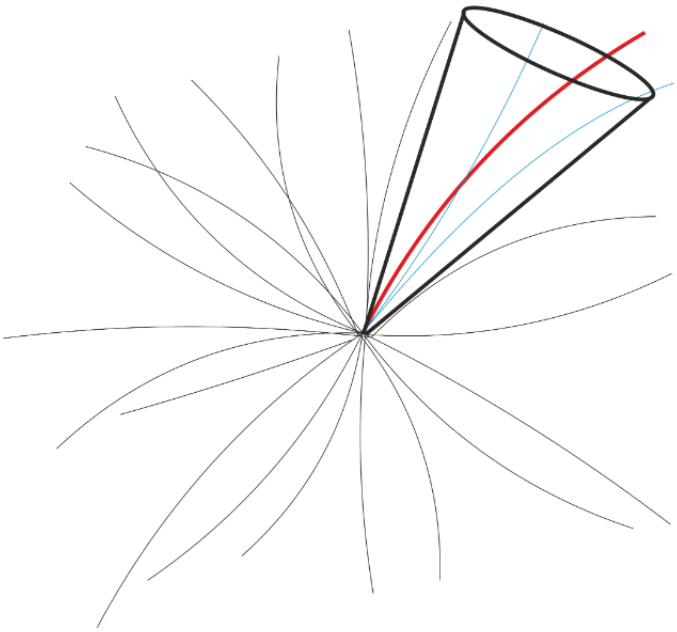

Figure 4.4: Visual (unrealistic) representation of an event with a "hard-scattering" particle (in red), the accepted pile-up particles (in light blue) and the rejected pile-up particles (in grey). The RoI is a cone around the hard-scatter particle with fixed $\Delta R = 0.1$.

The idea at the basis of this method is that to efficiently represent the pile-up effect on the detector performances it is not necessary to simulate all the pile-up particles, because most of them are distant from the particles of interest and cannot produce fake hits that alter the reconstructed tracks. This method implies some important assumptions:

- The chosen radius value is large enough to contain all the pile-up particles that can produce fake hits;
- As the RoI is computed at generation level, before the simulation of the effect of the magnetic field on the charged particles, it is assumed that the curvature does not bring particles that were initially outside of the RoI cone inside of it, potentially producing fake hits;
- The ΔR variable is an angular variable which does not take into account the vertex displacement between the particles considered. This leads to

the fact that particles that travel approximately parallel to each other but spatially distant can be included into the RoI even if they do not produce fake hits in the silicon layers. On the contrary, particles that have different angular parameters and distant vertices with respect to the hard-scatter particles in the event are not included into the RoI but can potentially intersect the silicon layers in points where they can produce fake hits. It is assumed that these particles do not contribute appreciably to the fake rate.

The validity of these assumptions were tested by simulating a limited number of samples with a larger value of the RoI size, and are discussed in Chap.5.

In this thesis two applications of this method are presented, analysing two different aspects of ITk performances: particle gun studies and physics studies, the latter in the $H \to ZZ^* \to 4\mu$ channel.

4.5 Fast simulation method applied to particle gun studies

Single particle studies, from now on dubbed **particle gun**, are a very useful tool to analyse the tracking performances of the detector, allowing to study the number of hits distribution, reconstruction efficiency, resolution and the reconstruction of fake tracks. In these studies, one particle with given kinematic properties is injected in the simulation for each event.

The generation flow in the fast simulation method studied is shown in Fig.4.5 and proceeds as follows, for every event (i.e. bunch-crossing).

- Generation of a single particle of fixed type ("pdgId"[2]) and user-defined distribution (for specifics, see Chap.5);
- For each event, generation of a number of pile-up events extracted from a Poissonian distribution with fixed mean $\langle\mu\rangle$. The vertex is smeared according to the bunch shape defined in the generation job option (σ_z = 75 mm, $\sigma_{x,y}$ = 15 μm);

[2]The *pdgId* is a standardized Monte Carlo variable that uniquely identifies the particle species.

- For every generated pile-up particle in the final state, if it lies inside a cone of fixed $\Delta R = 0.1$ around the hard-scatter particle it is added to a truth vertex, which is added to the vector of output vertices;
- A primary vertex is built with the hard scatter particle placed at the origin of the ATLAS reference frame.

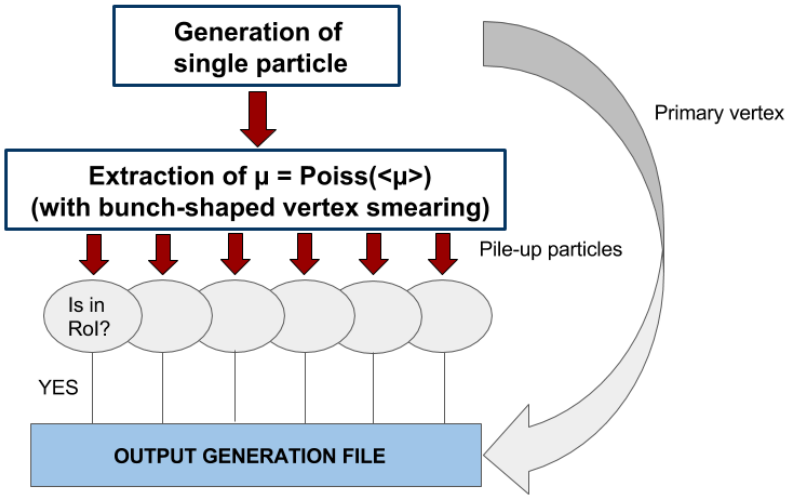

Figure 4.5: The generation flow for the particle gun samples employed in the fast simulation method.

At the end of the event, the output vertices are pushed to the generation file, which is then sent as input to the standard ATLAS simulation/digitization/reconstruction chain.

Samples with different parameters were produced by using a different initial Pythia seed to avoid repetitions in the pile-up sample.

4.6 Fast simulation method applied to physics studies

Physics studies are similar to particle gun studies for what concerns the generation technique and consist in the generation of a physics event with a superimposed pile-up distribution. There is a difference as the physics events

are generated separately and then used at the generation phase, replacing the particle gun section.

The generation flow in this case is then slightly different from the particle gun case, because the physics objects distribution is not user-defined but previously generated with a Monte Carlo generator. It is visually described in Fig.4.6 and proceeds as follows:

- Generation of N proton-proton collisions with the production of the physics process of interest;
- Extraction of the final state particles of interest to an ASCII file containing their position and momentum four-vectors and the pdgId, after applying the appropriate generation selection;
- For each event, generation of a number of minimum bias events extracted from a Poissonian distribution with mean $\langle\mu\rangle$, with a vertex smearing as described in Chap.4.5;
- For each generated final state minimum bias particle, check if it lies inside a cone of $\Delta R = 0.1$ around at least one of the charged particles saved in the ASCII file. If it does, it is added to a vertex, which will be in turn added to the list of output vertices;
- The particles contained in the ASCII file are added to a vertex placed at the origin of the ATLAS reference frame that will constitute the primary vertex of the event.

With respect to the particle gun method, a difference is that the number of RoIs (cones in ΔR) is not one but is equal to the number of final state particles that constitutes the searched signature. For example, in this study we present an application of this technique to the physics process $H \rightarrow ZZ^* \rightarrow 4\mu$, including possible final state bremmstrahlung photons emitted from the muons. Both the muons and the photons are saved into the ASCII file and simulated, but the cones are only drawn for the four muons. In this way, the photons can convert and potentially produce hits in the tracker and they can also be used to study the effect on the estimate of the Higgs boson mass.

Also note that the only hard scattering particles simulated in this case are the ones coming from the elementary parton-parton collision, excluding

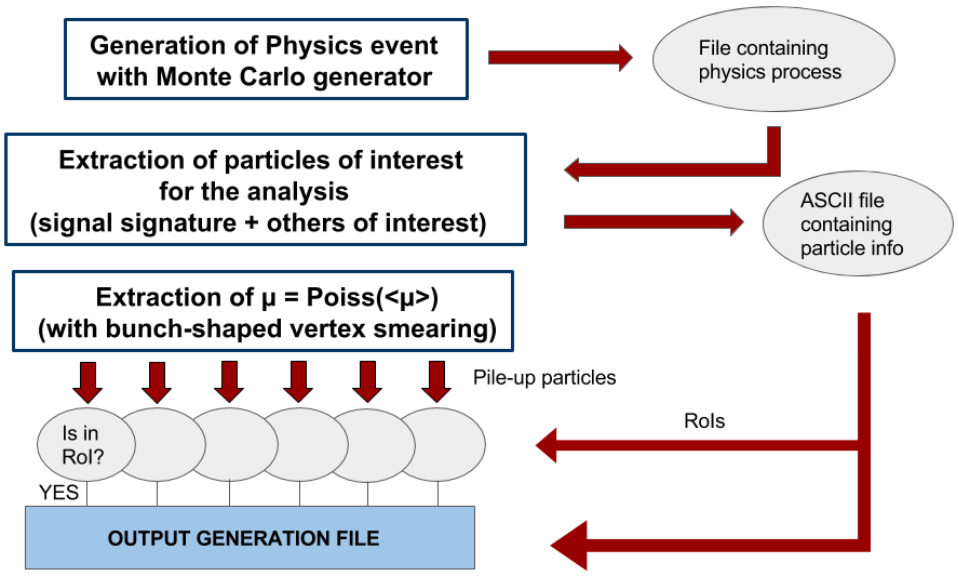

Figure 4.6: The generation flow for the physics samples employed in the fast simulation method.

the remaining part of the underlying event. This is an approximation that was considered reasonable as, although it is not completely true that the underlying event is independent from the hard-scattering event, in the high pile-up environment of HL-LHC fake hits are expected to be mainly due to pile-up particles.

Due to the assumptions used in generating these samples, physics studies have some limitations that must be taken into account when looking at the findings.

4.7 Time requirements

In this section the timing requirements of the fast simulation technique and the standard full simulation method are compared. The chain from generation to reconstruction was run on a CERN LXPLUS machine.

The results are shown in Tab.4.1, for a single muon with $p_T = 15$ GeV sample, in the $\langle\mu\rangle = 200$ scenario and InclBrl4 layout. Muons were chosen as they are very quick to simulate, so the time is (both in fast and full simulation) dominated by the pile-up events simulation. In charged pion samples, fast simulation time is strongly dependent on the generated p_T.

	Fast sim./evt.	Full sim./evt.	Fast sim./50K evt.	Full sim./50K	Ratio(fast/full)
Gen	2.45s	2.45s	1d 10h	1d 10h	100%
Sim	0.20s	88 m	2h 46	8y	0.004%
Digit	0.04s	47s	33m	27d	0.1%
Reco	0.06s	2m 40s	50m	90d	0.04%
Total	2.75s	90m	1d 14h	8y	0.05%

Table 4.1: Comparison between fast and full simulation timing requirements at $\langle\mu\rangle = 200$, for a muon particle gun with $p_T = 15$ GeV, in the InclBrl4 layout. The full simulation results for 50 thousand events have been extrapolated from a sample of 5 events.

From the result it is noticeable that the time required by the generation is in both cases the same, which is due to the fact that in the fast simulation method all the pile-up particles are generated and only then discarded if they do not lie inside the RoI. The huge total full simulation time for 50 thousand events ($\sim$ eight years) show that it is impossible to use the employed technology to produce these samples. However, some samples were produced by ATLAS exploiting the large parallelization available on the GRID. The absolute time results in Tab.4.1 are thus to be considered as an indication of the difficulties presented by the high pile-up environment of HL-LHC, whereas the value of the ratios show the comparison between analogous computing frameworks.

Chapter 5

Tracking performances of the upgraded Inner Tracker

5.1 The ATLAS tracker upgrade: ITk

The current ATLAS Inner Detector was designed to operate for 10 years at a maximum luminosity of $10^{34}\ cm^{-2}s^{-1}$, average number of in-time pile-up events $\langle\mu\rangle = 23$ per 25 ns bunch-crossing, with a L1 trigger rate of 100 kHz[2]. As described in Chap.2.2, it consists of 3 pixel layers (plus the Insertable B-Layer, IBL), 4 layers of silicon microstrips (SCT) and a straw tube tracker (TRT). The HL-LHC conditions are particularly challenging, and the current tracker will not be able to perform adequately, leading to the necessity of a completely new tracker, called **Inner Tracker** (ITk). The main limitations of the current Inner Detector under the HL-LHC conditions are the following:

- both the pixel (including IBL) and the SCT detector were designed to withstand a radiation fluence much smaller than that expected at HL-LHC;

- due to limitations in the buffering and the communication between the module local electronics and the read-out card, which were designed for a maximum number of pile-up events of 50, at a luminosity of $3 \cdot 10^{34}\ cm^{-2}s^{-1}$, both the pixel and the SCT detectors are expected to be inefficient, with a subsequent data loss;

- the present SCT would be unable to resolve close particles in particularly dense events (hith p_T jets), and the TRT straws will approach 100% occupancy.

Due to the increase of the instantaneous luminosity to $\mathcal{L} = 5 - 7.5 \cdot 10^{34}$ cm^{-2}s^{-1} and the center of mass energy increase to 14 TeV with the consequent proton-proton inelastic cross section increase, the number of expected average collisions per bunch crossing will reach the value $\langle\mu\rangle = 200$, with an expected beam spot of $\sigma_z = 75$ mm. The main requirements of the new Inner Tracker will be to:

- measure the momentum of isolated charged particles, in particular electrons and muons, the latter being reconstructed and identified also with the help of the muon spectrometer;
- reconstruct the vertices and identify the primary vertex corresponding to the hard-interaction;
- identify secondary vertices in b-jets with high efficiency and purity;
- measure tracks in the core of high p_T jets with good double-track resolution;
- identify τ lepton decays with the measurement of the impact parameter;
- reconstruct the tracks corresponding to a converted photon;

The resolution requirements were defined in [36] and are shown in Tab.5.1.

Track parameter ($0 < \|\eta\| < 0.5$)	Units	$\sigma_x(\infty)$
Inverse transverse momentum $\sigma(q/p_T)(\infty)$	TeV^{-1}	< 0.2
Transverse impact parameter d_0	μm	< 8
Longitudinal impact parameter z_0	μm	< 50 (η dependent)

Table 5.1: Expected track resolutions at large transverse momentum, with an average number of pile-up events $\langle\mu\rangle = 200$[36].

In the next paragraph are presented some of the proposed layouts for the future ITk detector.

5.2 The Step-1 layouts

After the publication of the ATLAS Phase II Scoping Document[1], the ATLAS community started to study several different ITk layouts. The optimization process was divided into steps. In this thesis, the tracking performances

of the three current layouts at **Step-1** are studied. In particular, this section describes the tracking performances of these layouts using "particle gun" samples of charged pions and muons.

Step-1 layouts are designed to be accurate from the point of view of the geometry and sensors description, but not completely realistic in the description of passive material and services, nor in the reconstruction algorithms. Studies that make use of these layouts, such as the one presented in this thesis, are thus to be considered with particular care. However, as the main task for HL-LHC is to study the Higgs properties, it is important that physics performances are fulfilled.

The main difference of several proposed ITk layouts with respect to the current Inner Detector is the absence of the TRT in favour of the exclusive use of pixel and SCT layers, with extended angular coverage to $|\eta| < 4.0$, to be compared with the current one, that only reaches $|\eta| < 2.5$.

The three layouts studied are shown in Fig.5.1. They have the same angular coverage, SCT and pixel endcap geometry, and only differ in the **pixel barrel** sector. In the **Extended Barrel 4.0 layout** (ExtBrl4), the two innermost barrel layers are longer and reach ± 1215 mm in the z-axis, while the three remaining extend to ± 730 mm. In the **Inclined Barrel 4.0 layout** (IExtBrl4), the two innermost barrel layers are extended in length but are subdivided into a short flat sector (± 180 mm and ± 200 mm respectively) and an *inclined* sector, in which the layers are tilted at a fixed angle of about 35 degrees with respect to the horizontal plane. Each module in this sector is formed by two pixel modules at a distance that ranges from 4 to 6 mm from each other. In the **Fully Inclined 4.0** (InclBrl4) layout, all of the pixel barrel layers are subdivided into a central flat sector and an inclined sector. In this case the length of the flat sector depends on the layer and increases from ± 180 mm in the innermost layer to ± 320 mm in the outermost layer. The inclined sector extends to ± 1200 mm for the two innermost layers and to ± 700 mm for the others. The number of the inclined modules is the same as the IExtBrl4 layout for the two innermost layers and is 13 for the other layers. The value of the radii of the barrel layers are summarized in Tab.5.2.

The **pixel endcap disks** extend to ± 3000 mm. Their number depends on the layer and ranges from 15 to 20 per detector side.

The **SCT system** is identical for the three layouts. It is composed by four barrel layers of identical length (± 1372 mm). The value of the radii

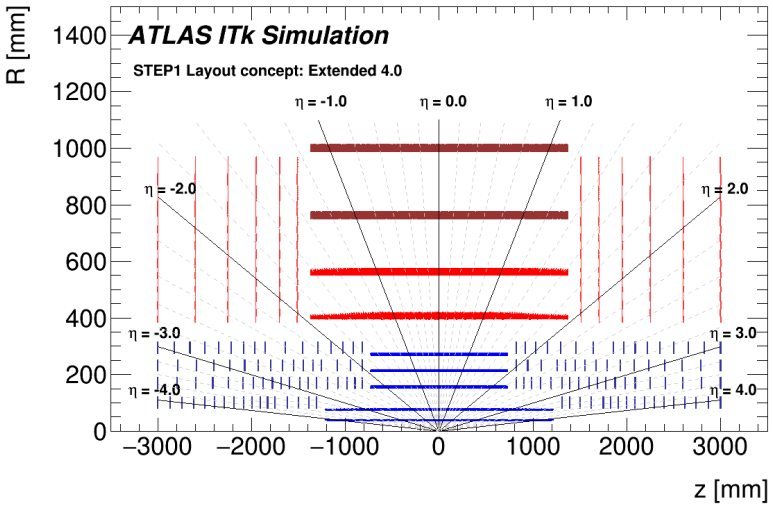

(a) The Extended Barrel 4.0 layout (ExtBrl4).

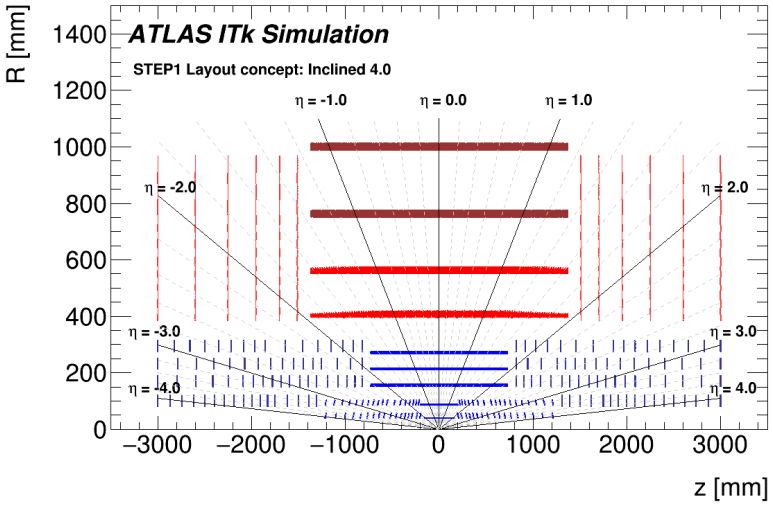

(b) The Inclined Barrel 4.0 layout (IExtBrl4).

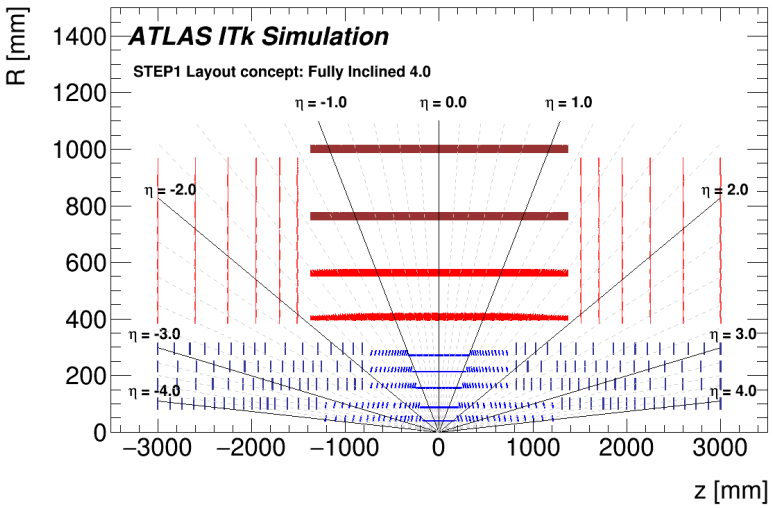

(c) The Fully Inclined 4.0 layout (InclBrl4).

Figure 5.1: R-z view of the Step-1 layouts.

are shown in Tab. 5.2. The reduced number of SCT layers is one of the most important changes with respect to the Scoping Document[1]. There are six endcap disks per side, ranging in z from 1500 mm to 3000 mm. Each strip module has strips in each side, with a relative tilt of 40 mrad. This is necessary to obtain a measurement of the third coordinate when a particle produces hits on both sides of the strip.

	Layer	**Radius (mm)**
Pixel	1	39
	2	75*
	3	155
	4	213
	5	271
SCT	1	405
	2	562
	3	762
	4	1000

Table 5.2: For the three Step-1 layouts considered, values of the barrel layers radii in the Pixel and SCT layers. *The second pixel layer is 75 mm only for the ExtBrl4 layout, and is 85 mm in the IExtBrl4 and InclBrl4 layouts.

For the studies that will be presented in this thesis, it is useful to identify critical pseudo-rapidity regions for the three layouts. The region $0 < |\eta| < 1.0$ is completely covered by flat barrel layers in all the layouts; in the region $1.0 < |\eta| < 1.4$ the InclBrl4 layout starts the transition to the inclined barrel modules in the three outermost layers; in the region $1.4 < |\eta| < 1.8$ the same happens for the innermost layers (IExtBrl4 and InclBrl4); also, the region $1.0 < |\eta| < 1.8$ marks the tranition from SCT barrel to SCT endcap; the region $1.8 < |\eta| < 2.2$ is the transition region from pixel barrel to pixel endcap; the region $2.2 < |\eta| < 2.7$ relies on pixel and SCT endcap; the region $2.7 < |\eta| < 3.2$ is pixel only (two innermost barrel layers + pixel endcap); the most forward region $3.2 < |\eta| < 4.0$ counts only on the innermost barrel layer and the pixel endcap disks.

With respect to the current Inner Detector, the momentum resolution will benefit from the longer lever arm, a large number of silicon hits (typically 13, also to account for possible dead modules), smaller pixel sizes (50×50 μm^2, with 150 μm sensor thickness) and smaller strip lengths (23.8 mm in the two innermost layers and 47.6 mm in the remaining, 75 μm pitch and 320 μm

thickness)[1]. Also, the material contribution in terms of radiation lengths will be significantly smaller than in the current Inner Detector ($< 0.7X_0$ against $1.2X_0$), for a broad pseudo-rapidity region. This will be important to minimize photon conversions, electron bremmstrahlung and hadron interactions.

One of the effects connected with the angular coverage extension proposed in these layouts is the generation of *long clusters* in the forward region. This effect is a purely geometrical one and emerges from the fact that particles with large pseudo-rapidity traverse the depth of the sensors, therefore the corresponding signal spans over a broader region. This effect is minimized in the inclined layouts, where the inclined sensors ensure that the particle traverses a smaller amount of material. However, a better reconstruction algorithm could reduce the impact of this effect in the ExtBrl4 layout by using the sharing of the signal among different pixels. Unfortunately in Step-1 studies the reconstruction algorithms still need to be optimized, so it is too early to draw final conclusions from the comparison of different performances in the forward region.

5.3 Monte Carlo samples

Particle gun samples of $4.5 \cdot 10^4$ events were generated with charged pions following the technique described in Chap.4.5. The charge of the pion is chosen randomly for each event. Each sample contains pions distributed with flat η in the range [-5,5], flat ϕ in the range [-π, π] and fixed transverse momentum (5 GeV, 15 GeV, 50 GeV, 100 GeV). A flat η distribution was chosen to study all the regions of the detector with the same statistics, whereas the chosen η range, that extends well beyond the detector coverage ($|\eta| < 4.0$), is a standard within the ITk tracking studies and allows to study possible effects at the detector edges. To compare the performances of the detector under different pile-up conditions, samples were produced with $\langle\mu\rangle = 0$, 50, 200, for the three ITk layouts described (ExtBrl4, IExtBrl4, InclBrl4).

5.4 Motivations of the study

Particle gun studies are a particularly useful tool to measure the tracking performances of the detector, because they allow to perform specific measurements in well controlled conditions (fixed p_T in our case). The idea is

to generate a hard particle that simulates one of the outgoing products of a hard-scattering process, and superimpose a given number of pile-up events. Measurements of interest that can be performed with these studies include track quality parameters, reconstruction efficiency, fake probability and track parameters resolution.

The choice of generating charged pions was based on several reasons. Pions are the most frequently produced charged particles in the collisions, and are also the most frequent secondary particle produced by the strong interaction of hadrons. They typically lose energy in the tracker continuously by ionization, with a Landau distribution very similar to that of the muons, but they can also undergo strong interactions, with the production of several secondary particles. The reconstruction of their tracks is thus more difficult than in the case of the muons and poses interesting problems for further studies.

5.5 Event features

After the generation step, each sample was processed using the full simulation/digitization/reconstruction chain. The final xAOD file contains the information at both truth and reconstruction level.

For the different pile-up scenarios, the number of reconstructed tracks, the number of simulated primary and secondary charged particles per event (inside the simulated region of interest) are shown in Fig.5.2, 5.3, 5.4, for the InclBrl4 layout (as an example) and with pion $p_T = 15$ GeV. The plots show the growth in the number of particles produced with increasing average number of generated pile-up events and the correspondent increase in the number of reconstructed tracks. Events in which no track is reconstructed are mostly due to the geometrical acceptance (80%), and part is caused by reconstruction inefficiencies (Fig.5.2).

From the distribution of the number of tracks per event in the $\langle\mu\rangle = 0$ scenario is visible how the single simulated pion can produce more than one track due to the production of high p_T secondary particles. The plot in Fig.5.5 shows the number of secondary charged particles produced by the pion (in the $\langle\mu\rangle = 0$ scenario) with a 1 GeV minimum transverse momentum requirement.

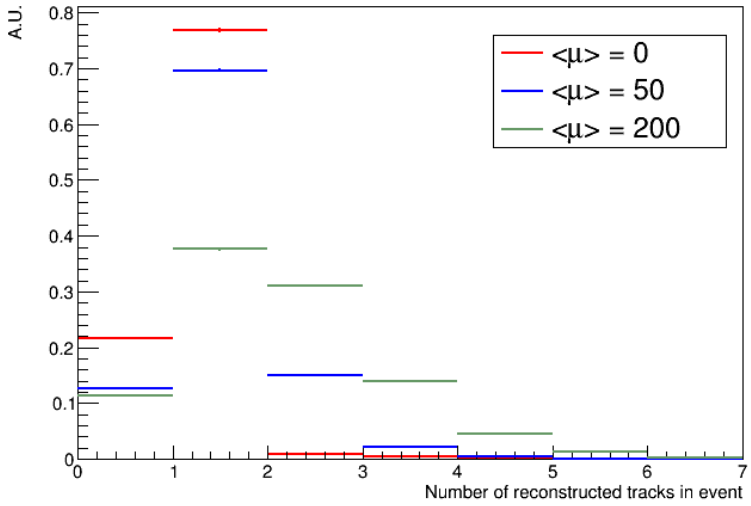

Figure 5.2: Number of reconstructed tracks per event in different pile-up scenarios, for the InclBrl4 layout and pion $p_T = 15$ GeV.

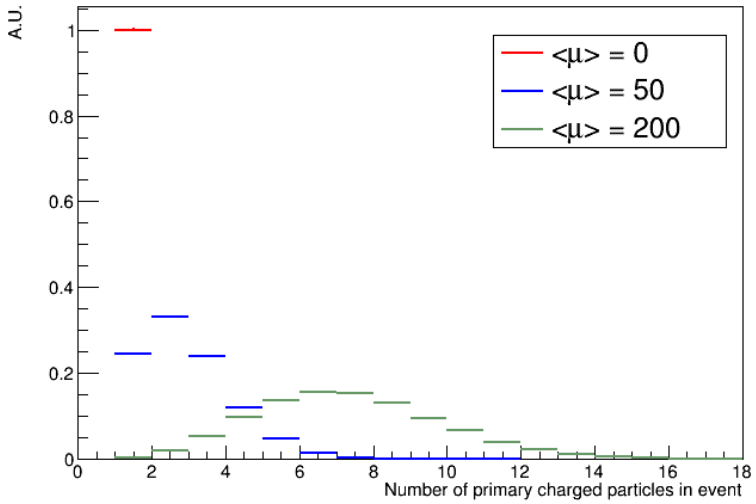

Figure 5.3: Number of simulated primary charged particles per event in different pile-up scenarios, for the InclBrl4 layout and pion $p_T = 15$ GeV.

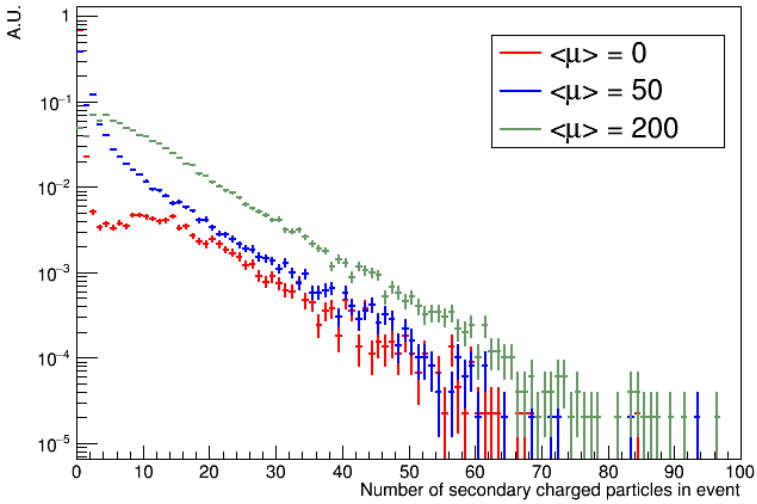

Figure 5.4: Number of simulated secondary charged particles per event in different pile-up scenarios, for the InclBrl4 layout and pion $p_T = 15$ GeV.

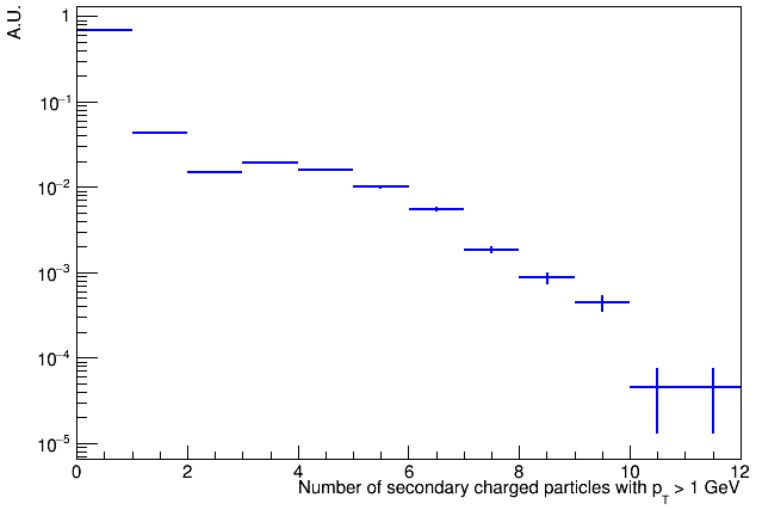

Figure 5.5: Number of secondary charged particles with $p_T > 1\ GeV$ in the $\langle\mu\rangle = 0$ sample, in the InclBrl4 layout and pion $p_T = 15$ GeV.

5.6 Track matching

To identify the pion generated with the particle gun, we look, among the primary particles, for a match in pdgID and p_T. The reconstructed track closest in ΔR to this particle is *matched* with it if this distance is less than 0.1 and the reconstructed p_T is larger > 3 GeV. The ΔR value corresponds to the size of the region of interest and is safely much larger than the track resolution in η and ϕ, as shown in Chap.5.8. In the other cases a match is not found. This excludes most of the events outside the geometrical acceptance, and those where the pion is not reconstructed, and there is no other high p_T track faking it. There could be events in which the hard-scatter pion lies beyond the geometrical acceptance but close to the detector edge and a high p_T track is reconstructed from the pile-up particles. These cases are included by the matching algorithm and can potentially contribute to the number of fake tracks. The "matched track" represents the reconstructed "hard-scattering" candidate of the event.

The dependence on $|\eta|$ of the number of reconstructed tracks is shown in Fig.5.6, in events with a generated pion with $p_T = 15$ GeV, in the InclBrl4 layout and $\langle\mu\rangle = 200$ scenario, only for the events in which a matching is found. The distribution is approximately flat, which indicates that the number of unmatched tracks is essentially constant.

5.7 Track quality

5.7.1 Comparison between matched and unmatched tracks

We studied two parameters that measures the track quality, separately for matched and unmatched tracks (the latter mainly due to pile-up particles). These are the **number of hits**[1] that constitutes the track, and the value of the **chi square per degree of freedom**. When dealing with the number of hits, it is important to remember that each SCT module is two-sided, so that it typically produces two hits per layer. The results are shown in Fig.5.7, 5.8.

The hit distributions are, for matched and unmatched tracks, similar but a tendency of the matched ones to produce tracks with more hits is noticeable (especially in the total hits distribution).

[1] From now on what we call "hits" are actually clusters.

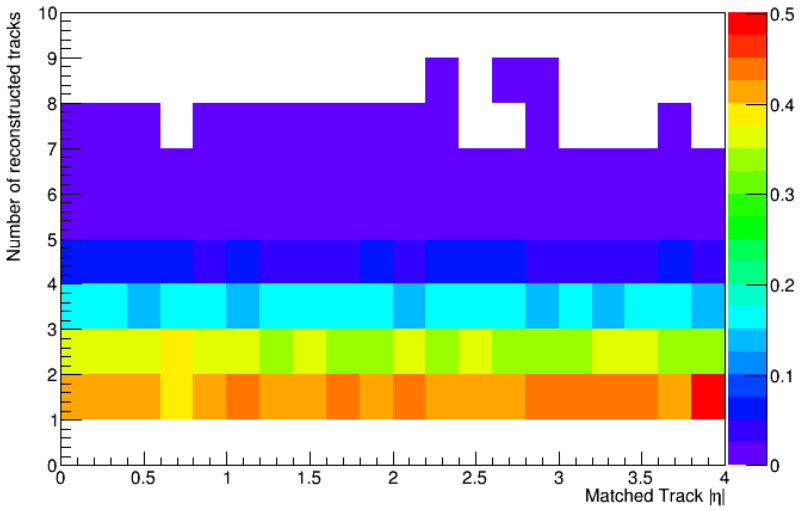

Figure 5.6: Number of reconstructed tracks per event as a function of the track $|\eta|$, for the InclBrl4 layout and pion $p_T = 15$ GeV, in the $\langle\mu\rangle = 200$ scenario. The bin contents have been normalized separately for every $|\eta|$ bin to reduce the impact of the generation fluctuations.

The χ^2/DOF distribution of the unmatched tracks is broader and denotes a generally -worse quality reconstruction of tracks generated by secondary and pile-up particles.

5.7.2 Quality of matched tracks

The distribution of the number of hits (Pixel, SCT, total) are shown, as a function of $|\eta|$, for the different layouts in Fig.5.9, 5.10, 5.11. The average number of hits for the three layouts is summarized in Tab.5.3. While the number of hits in the inclined layouts (IExtBrl4 and InclBrl4) are similar, the ExtBrl4 has an average number of hits significantly smaller because of the different barrel geometry. A requirement on the total number of hits of 9 for $|\eta_{track}| < 2.4$ and of 5 for $|\eta_{track}| > 2.4$ is applied in the reconstruction algorithm and is clearly visible in the distribution of the total number of hits. Also, with increasing $|\eta_{track}|$ the distribution of the number of hits becomes broader. This is an indication of the increasing difficulty of the reconstruction.

The number of holes in the pixel and SCT system, defined as the number

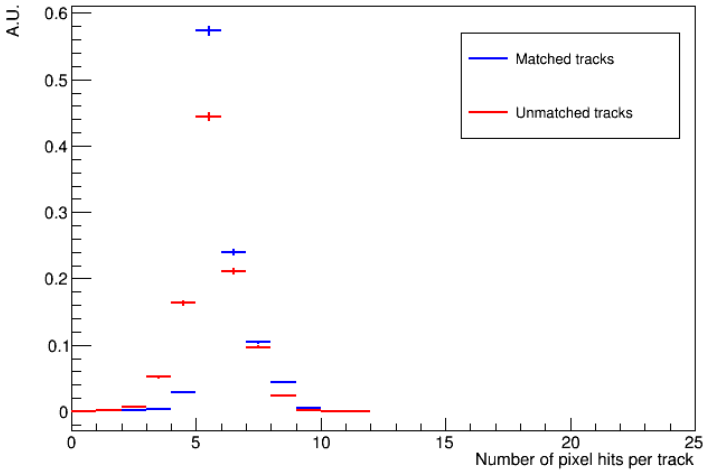

(a)

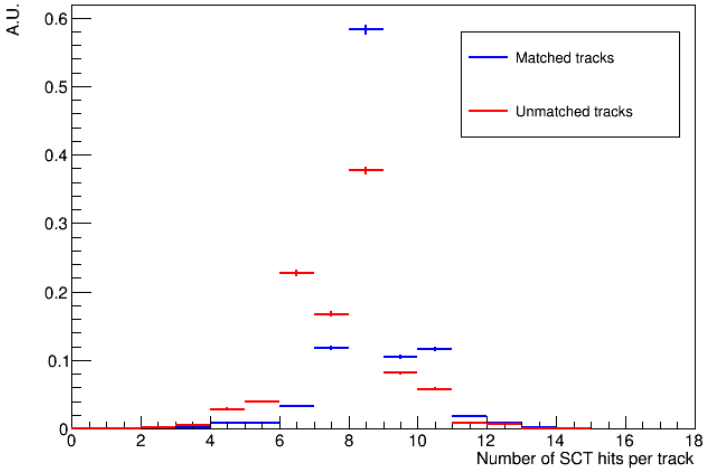

(b)

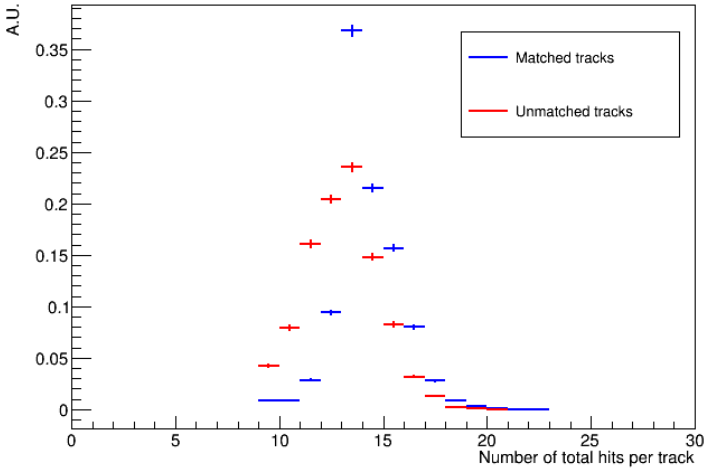

(c)

Figure 5.7: Number of pixel (a), SCT (b) and total (c) hits for matched and unmatched tracks in the sample with a generated pion with $p_T = 15\ GeV$, $|\eta <$ 1.0 and $\langle\mu\rangle = 200$, in the InclBrl4 layout.

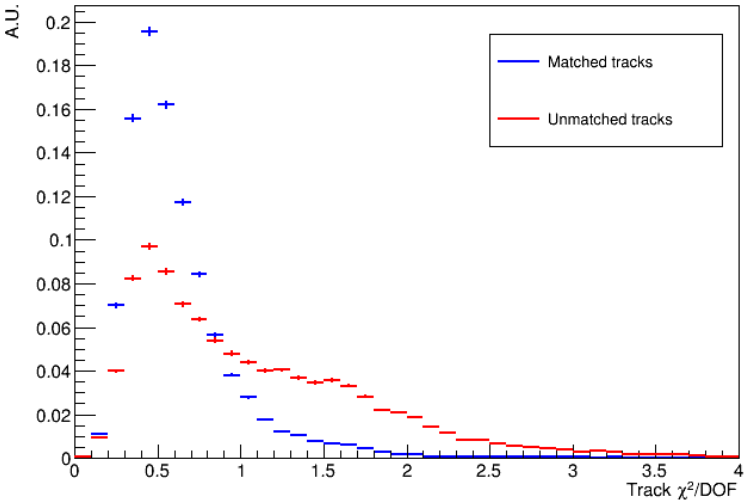

Figure 5.8: InclBrl4 layout: distribution of the χ^2/DOF for matched and unmatched tracks in the sample with a generated pion with $p_T = 15$ GeV and $\langle\mu\rangle = 200$.

	Pixel	**SCT**	**Total**
ExtBrl4	7.93 ± 0.02	5.64 ± 0.02	13.57 ± 0.01
IExtBrl4	9.53 ± 0.02	5.61 ± 0.02	15.14 ± 0.01
InclBrl4	9.81 ± 0.02	5.62 ± 0.02	15.42 ± 0.01

Table 5.3: Average number of pixel, SCT and total hits in the three ITk layouts considered.

of missing clusters when the extrapolated track expects to find one, was measured. It was found to be a small effect (around 1% of the matched tracks) and limited to the pixel system (no tracks with holes in the SCT were found). The distribution of holes in the pixel systems is shown in Fig.5.12 for the three layouts. The number of holes was found to be independent on the track transverse momentum within the statistical uncertainties. These "holes" correspond to small geometrical effects that are observed in each layout with a small difference of the InclBrl4 layout with respect to the others. The actual inefficiencies due to dead channels, readout errors and other effects are not considered in this phase.

The distribution of the average value of the χ^2/DOF in the different $|\eta_{truth}|$ bins is shown in Fig.5.13. The distribution is correlated to the distri-

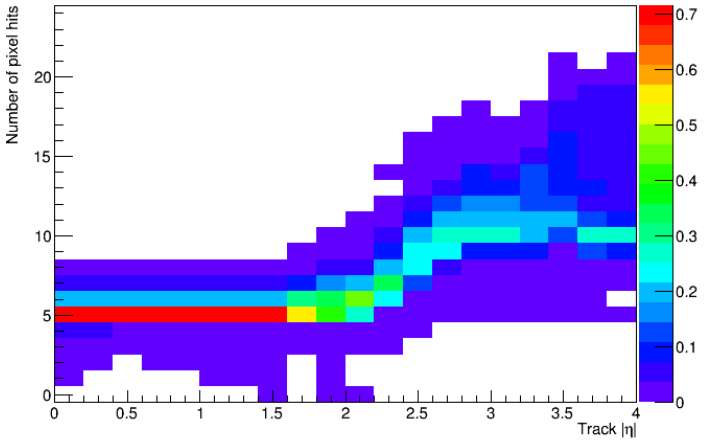

(a)

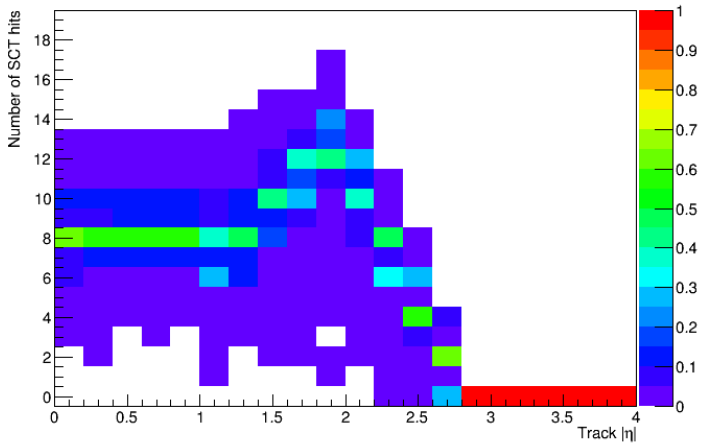

(b)

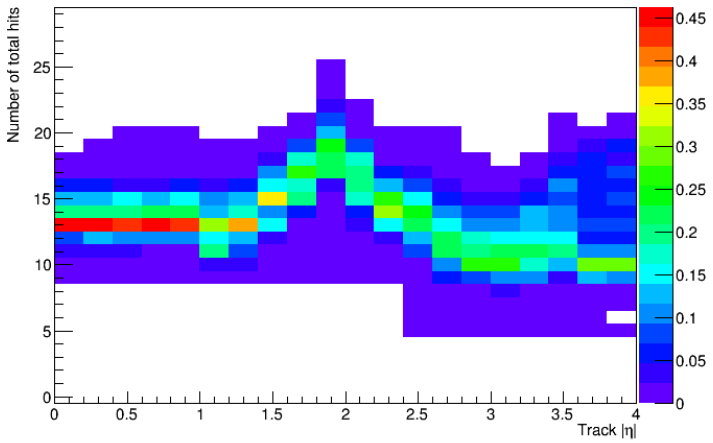

(c)

Figure 5.9: Number of pixel (a), SCT (b) and total (c) hits of the matched tracks as a function of the pseudo-rapidity in the sample with a generated pion with $p_T = 15\ GeV$ and $\langle\mu\rangle = 200$, for the ExtBrl4 layout. The content of each η bin was independently normalized so that the overall distribution does not depend on the η distribution of the track.

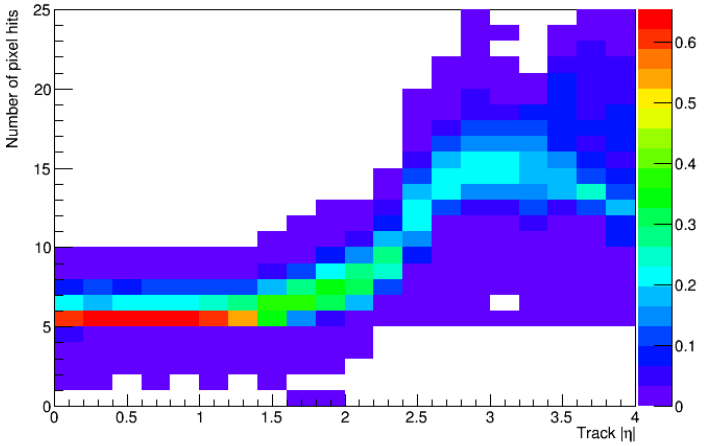

(a)

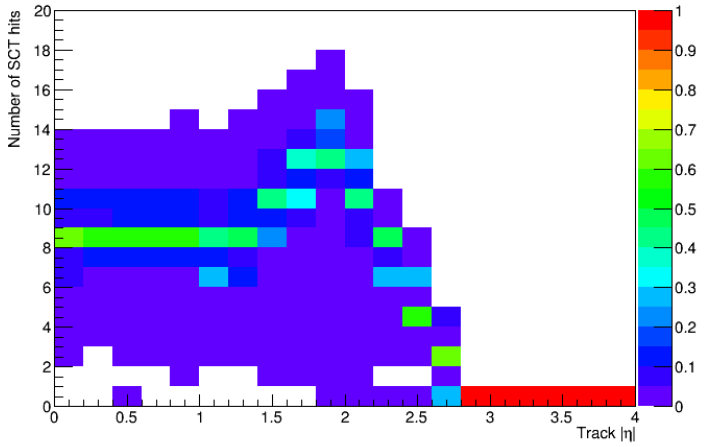

(b)

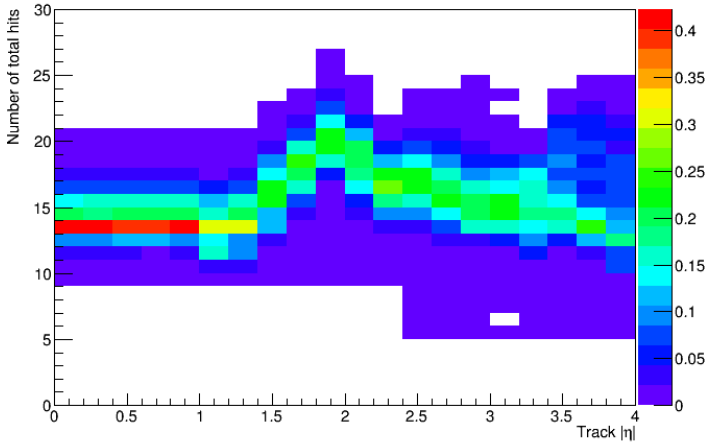

(c)

Figure 5.10: Number of pixel (a), SCT (b) and total (c) hits of the matched tracks as a function of the pseudo-rapidity in the sample with a generated pion with $p_T = 15\ GeV$ and $\langle\mu\rangle = 200$, for the IExtBrl4. The content of each η bin was independently normalized so that the overall distribution does not depend on the η distribution of the track.

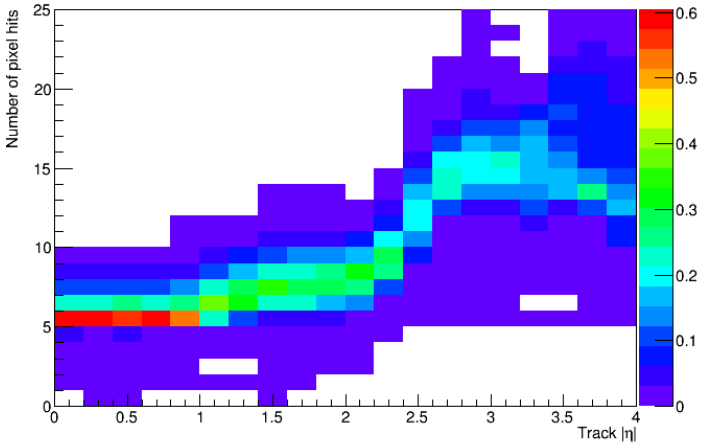

(a)

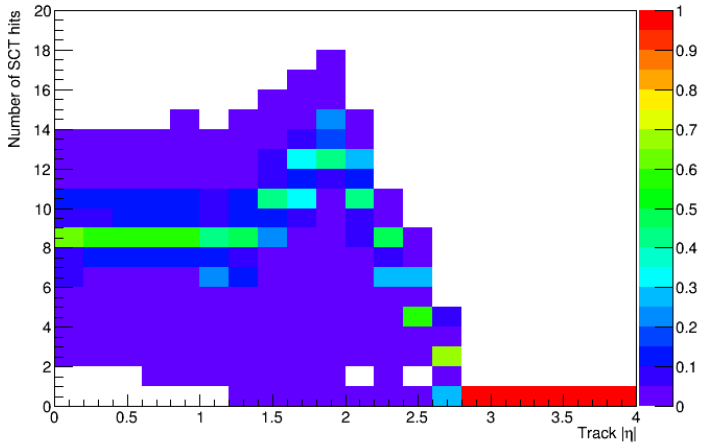

(b)

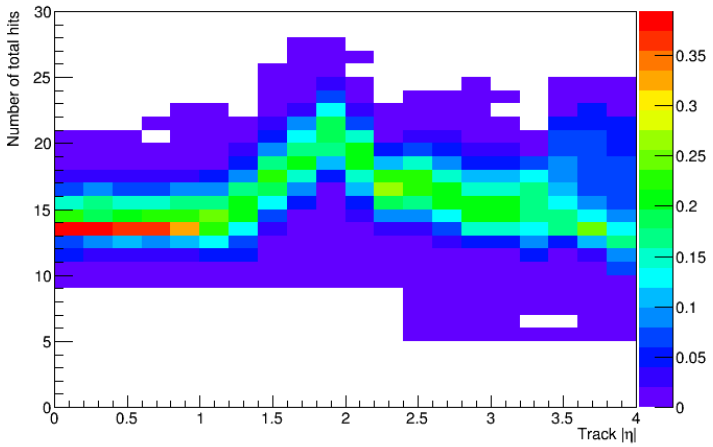

(c)

Figure 5.11: Number of pixel (a), SCT (b) and total (c) hits of the matched tracks as a function of the pseudo-rapidity in the sample with a generated pion with $p_T = 15\ GeV$ and $\langle\mu\rangle = 200$, for the InclBrl4. The content of each η bin was independently normalized so that the overall distribution does not depend on the η distribution of the track.

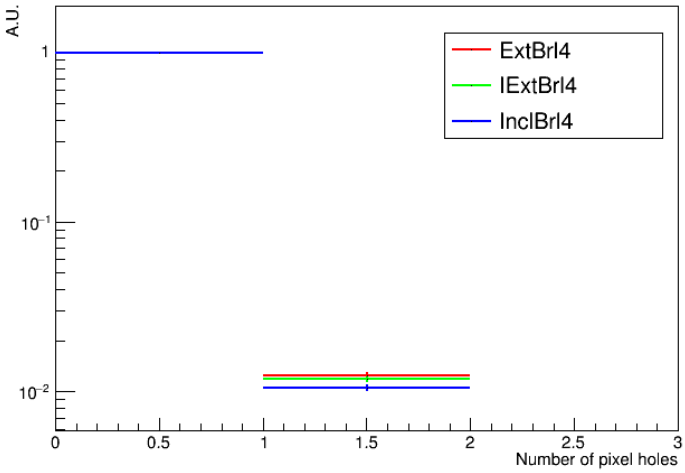

Figure 5.12: Number of holes in the pixel system for the three ITk layouts considered, at $\langle\mu\rangle = 200$ and $p_T = 15\ GeV$.

bution of the total number of hits, as the χ^2/DOF increases in the $|\eta|$ regions with a larger number of total hits. Also, the value of this variable is significantly smaller than 1 for the three layouts, which could be an indication of the overestimation of the uncertainties and/or of a significant departure from the gaussian model. A significantly larger value of the χ^2/DOF can be observed in the forward region for the ExtBrl4 layout, which is an indication of the worsening of track quality due to the formation of long clusters.

5.8 Track parameters reconstruction

The reconstruction resolution and bias of the reconstructed track parameters were calculated for different $|\eta_{truth}|$ bins by considering the distributions of the residuals:

$$\Delta_x = x_{matched} - x_{truth}$$

only for the events in which a match was found and $|\eta_{truth}| \in bin_i$. For each bin, an iterative gaussian fit was performed (appendix C). The **resolution** is defined as the σ parameter extracted from the fit, while the **bias** is defined as the mean parameter extracted from the fit. Results are shown for the different layouts at fixed pion $p_T = 15\ GeV$ and $\langle\mu\rangle = 200$ in Fig.5.14,5.15, 5.16,5.17. The IExtBrl4 and InclBrl4 layouts show very

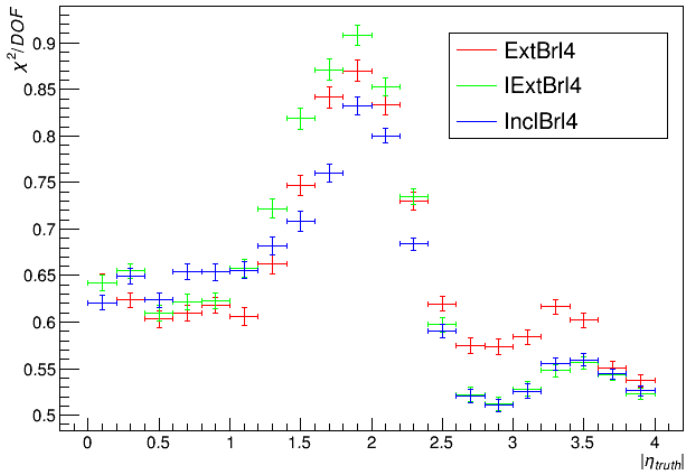

Figure 5.13: Average value of the χ^2/DOF variable for the matched tracks as a function of the track pseudo-rapidity, in the three ITk layouts considered, for a $p_T = 15\ GeV$ pion and in the $\langle\mu\rangle = 200$ scenario.

similar performances. The ExtBrl4 layout show worse performances in the forward region for each variable considered, but slightly better performances are observed in the transition region between the flat barrel and the inclined modules for the d_0 parameter.

The results for the resolution show a substantial decrease of performances with increasing track pseudo-rapidity. This is caused by different effects:

- the decrease of the angle between the track and the magnetic field causes the particle to describe, for the same p_T, a helix with larger pitch, which is reconstructed with greater uncertainty. This particularly affects the track p_T reconstruction;

- the decrease of the angle between the track and the beam axis causes the d_0 and z_0 reconstruction uncertainties to increase for purely geometrical reasons;

- the increase of the angle between the particle and the pixel surface causes a spread over a large area of the energy released, producing a longer cluster. As already said, this is especially true for the ExtBrl4 layout, which does not implement (at this stage) an optimized reconstruction algorithm;

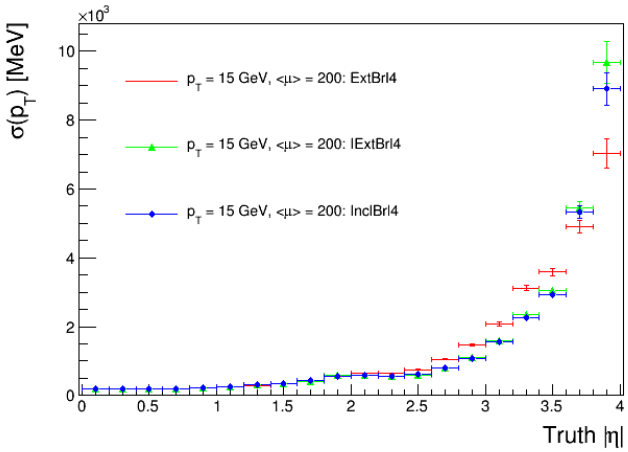

(a)

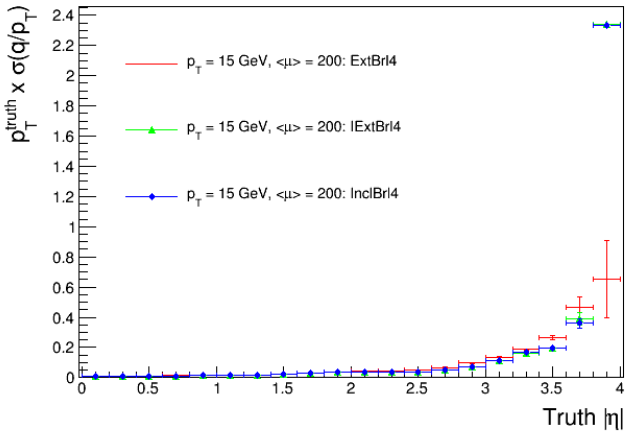

(b)

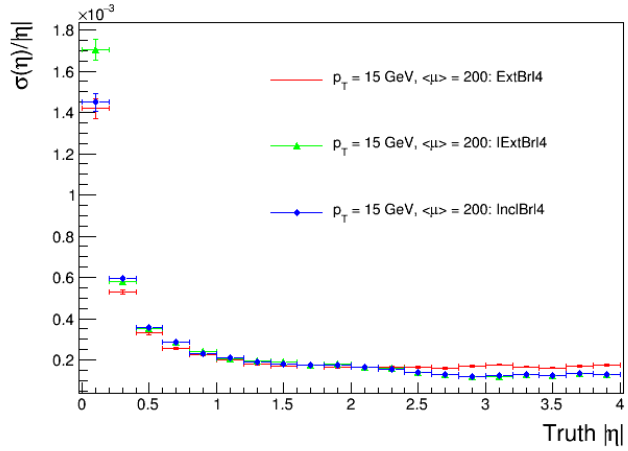

(c)

Figure 5.14: Resolution of the reconstructed track p_T, q/p_T and η for the three ITk layouts considered, in the sample with pion $p_T = 15\ GeV$ and $\langle\mu\rangle = 200$

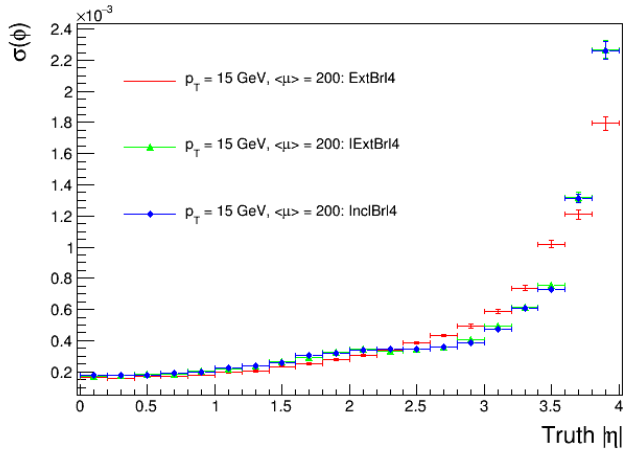

(a)

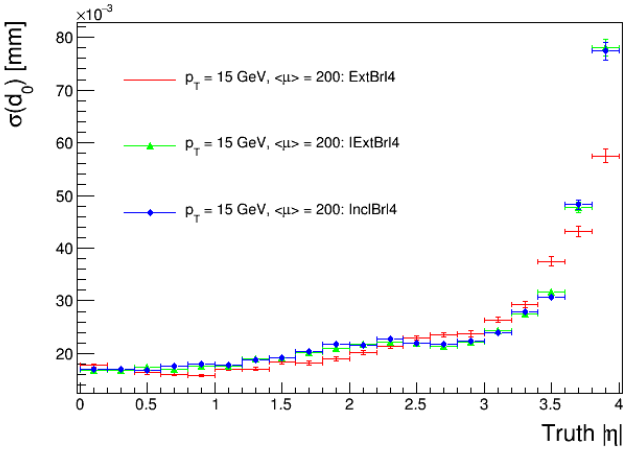

(b)

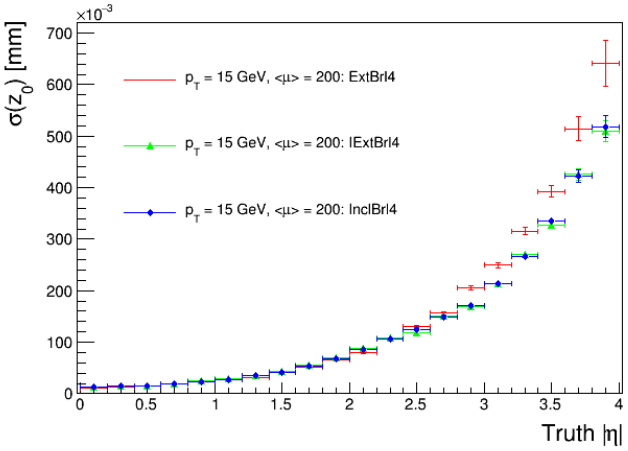

(c)

Figure 5.15: Resolution of the reconstructed track ϕ, d_0 and z_0 for the three ITk layouts considered, in the sample with pion $p_T = 15\ GeV$ and $\langle\mu\rangle = 200$

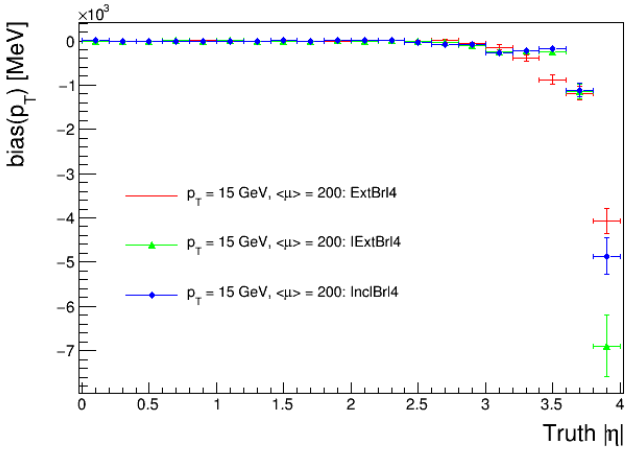

(a)

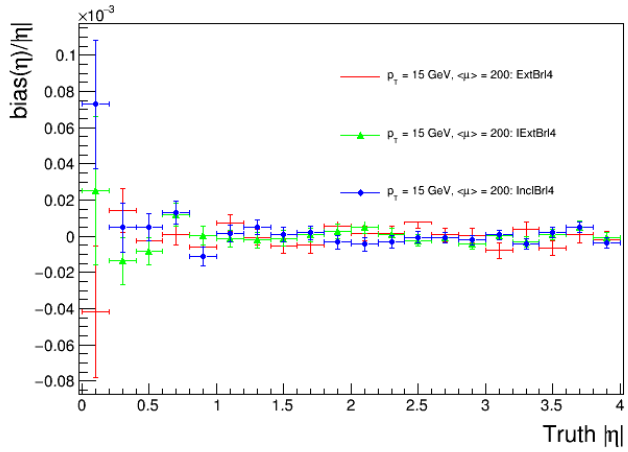

(b)

Figure 5.16: Bias of the reconstructed track p_T and η for the three ITk layouts considered, in the sample with pion $p_T = 15\ GeV$ and $\langle\mu\rangle = 200$

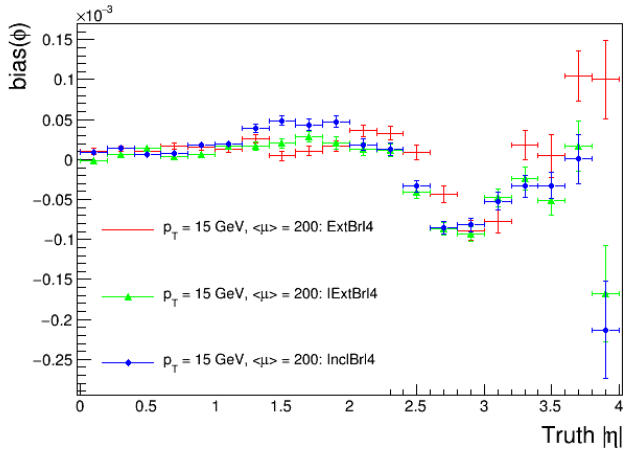

(a)

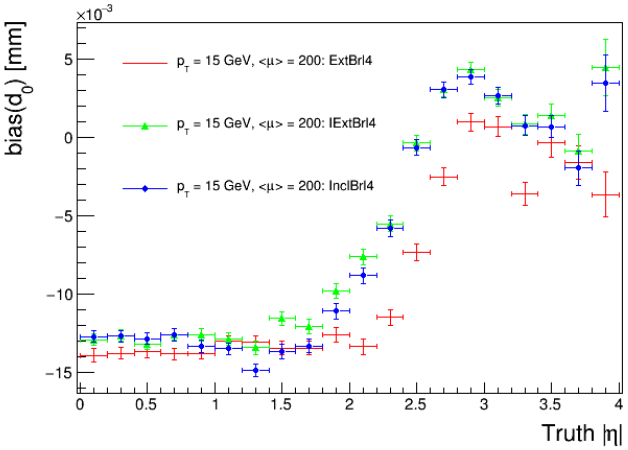

(b)

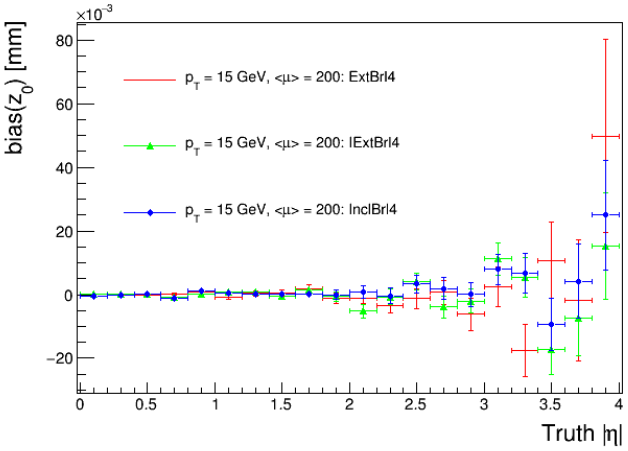

(c)

Figure 5.17: Bias of the reconstructed track ϕ, d_0 and z_0 for the three ITk layouts considered, in the sample with pion $p_T = 15\ GeV$ and $\langle\mu\rangle = 200$

- for the same reason the amount of material traversed by the particle is larger, so the interaction probability and the amount of energy lost by the primary particle is larger, which also causes a resolution decrease.

The increase of the uncertainty at high $|\eta|$ is not due to a lack of statistics but to the worsening of the gaussian fit quality, which, at large $|\eta|$, poorly describes the real distribution of the residual.

The results also show significant reconstruction biases for the variables p_T, ϕ and d_0 in different $|\eta|$ regions and for all layouts. The p_T results systematically underestimated in the region $|\eta| > 3.0$; ϕ is underestimated in the region $2.6 < |\eta| < 3.2$ and d_0 is underestimated in the region $|\eta| < 2.6$. This latter is particularly evident and credible because it happens in the central region where the resolution is optimal. This effect was also seen by other research groups and revealed an error in the geometry that was corrected in sequent geometry versions of the Step-1 layouts. The resolution of track parameters for different p_T (5, 15, 50, 100) is shown in Fig.5.18,5.19 for the InclBrl4 layout, in the $\langle\mu\rangle = 200$ scenario. The p_T resolution worsens with increasing p_T of the generated pion because of the smaller curvature radius; for the other variables the resolution tend to improve with increasing p_T as the multiple scattering plays a stronger role at lower p_T.

The resolution as a function of the average number of pile-up events is shown in Fig.5.20, 5.21, 5.22, 5.23,5.24, 5.25. No significant difference was observed, which shows that the layouts are robust against pile-up and that the fake rate is low.

Another quantity of interest to assess the quality of the reconstruction is the significance of the parameters, defined as:

$$x_{signif} = \frac{x_{matched} - x_{truth}}{x_{err}}$$

where x_{err} is the uncertainty on the variable x as estimated from the fit. If the variable is gaussian distributed, this distribution should be compatible with a gaussian distribution with mean = 0 and $\sigma = 1$. In Fig.5.26, for the sample with a $p_T = 15\ GeV$ generated pion, $\langle\mu\rangle = 200$ in the InclBrl4 layout, the significance is shown for the different reconstructed track angular parameters. Results show a general overestimation of the fit uncertainty, that causes the σ to be smaller than one and confirm the presence of a negative bias, especially in the d_0 reconstruction. This could also partially explain the systematically $\chi^2/DOF < 1$ measured in Fig.5.13. To verify if this effect

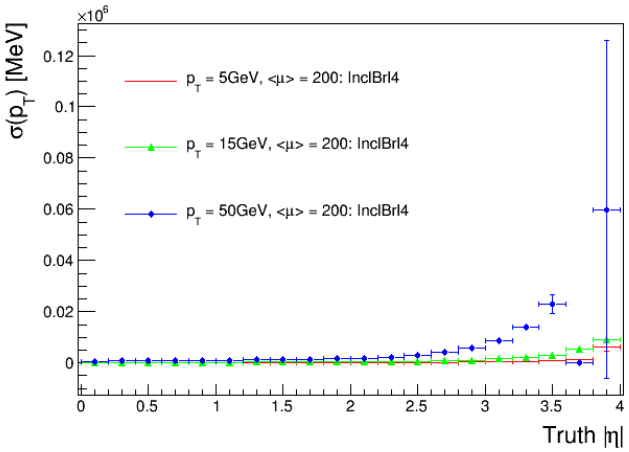

(a)

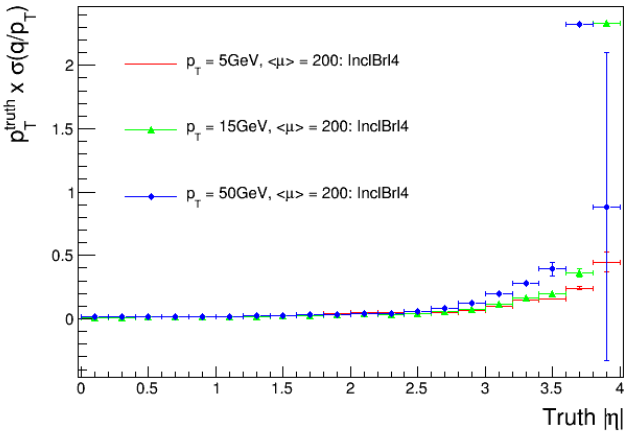

(b)

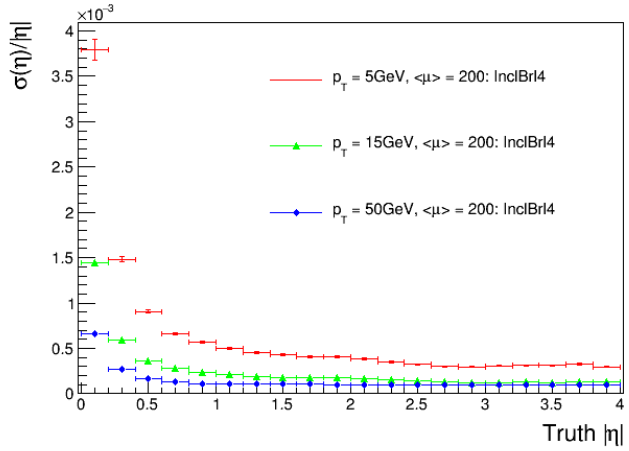

(c)

Figure 5.18: Resolution of the reconstructed track p_T, q/p_T and η for the InclBrl4 layout, in the $\langle\mu\rangle = 200$ scenario, as a function of the generated pion p_T

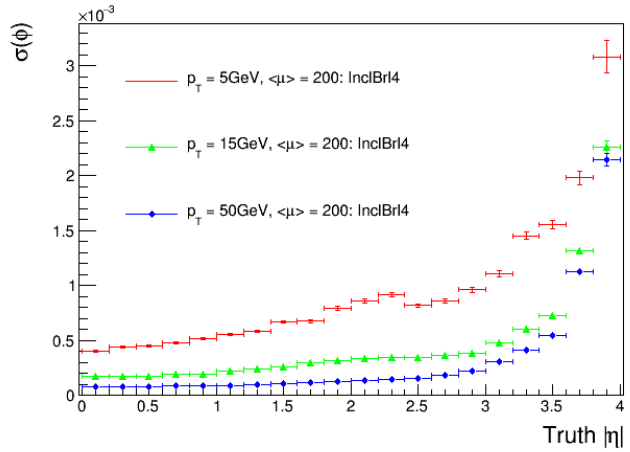

(a)

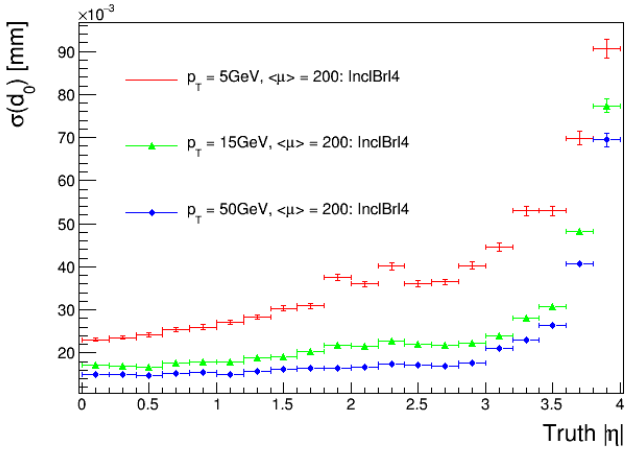

(b)

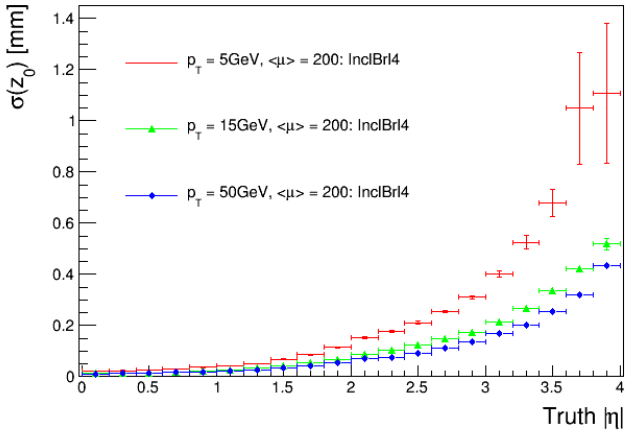

(c)

Figure 5.19: Resolution of the reconstructed track ϕ, d_0 and z_0 for the InclBrl4 layout, in the $\langle\mu\rangle = 200$ scenario, as a function of the generated pion p_T

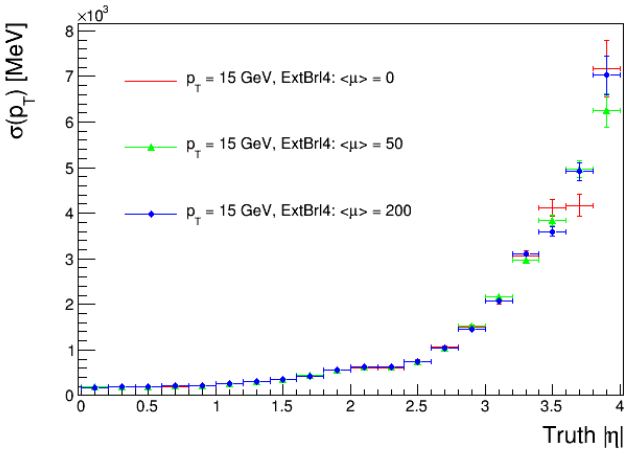

(a)

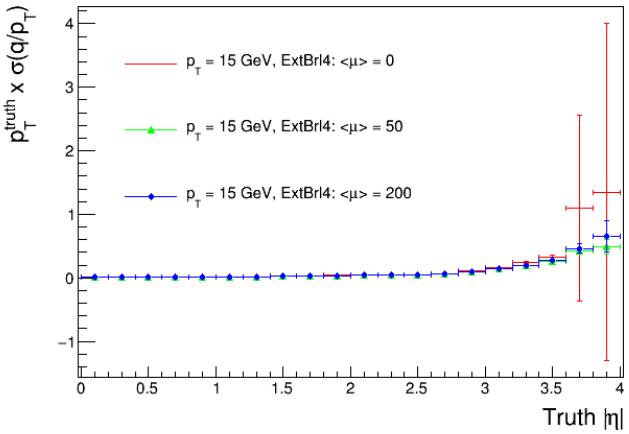

(b)

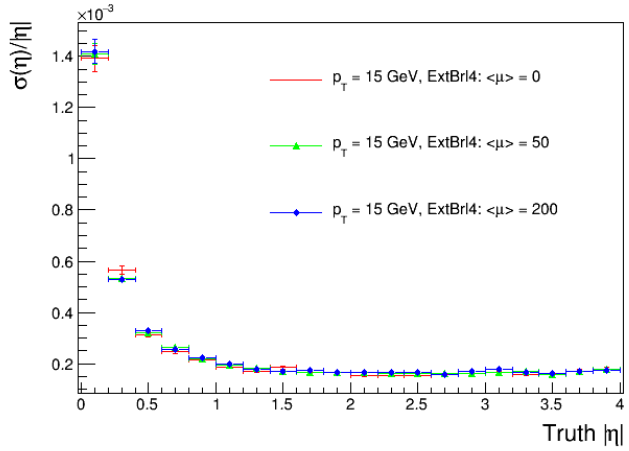

(c)

Figure 5.20: Resolution of the reconstructed track p_T, q/p_T and η for the ExtBrl4 layout, with a pion $p_T = 15$ GeV in different pile-up scenarios.

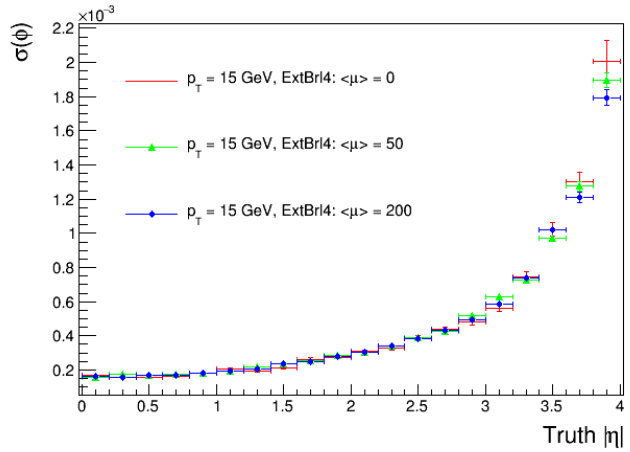

(a)

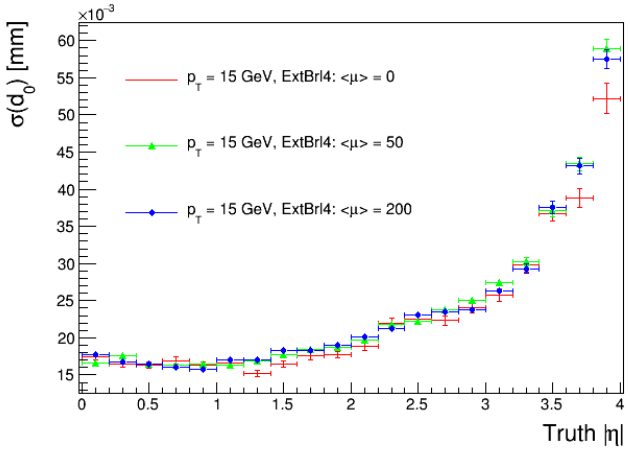

(b)

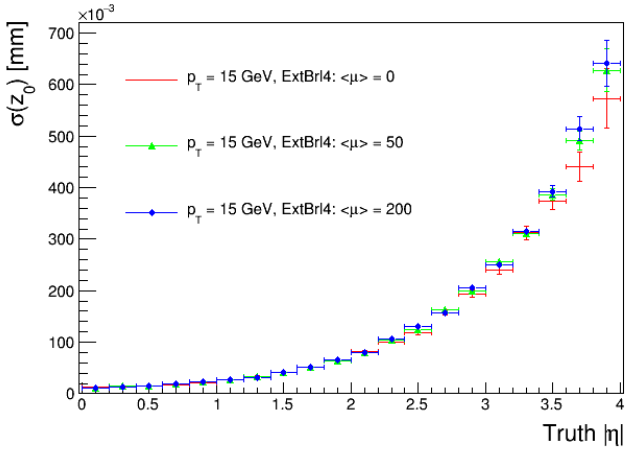

(c)

Figure 5.21: Resolution of the reconstructed track ϕ, d_0 and z_0 for the ExtBrl4 layout, with a pion $p_T = 15$ GeV in different pile-up scenarios.

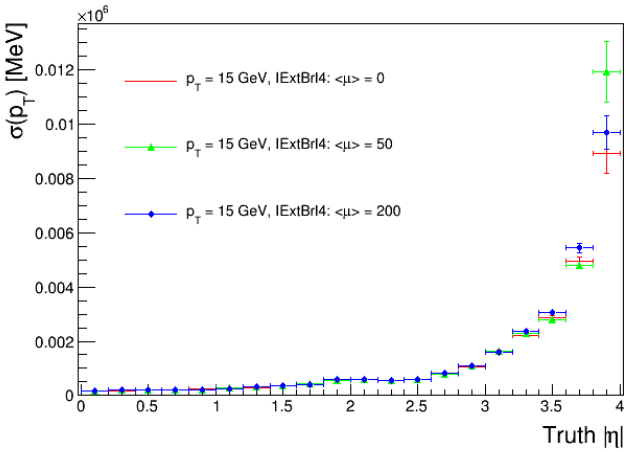

(a)

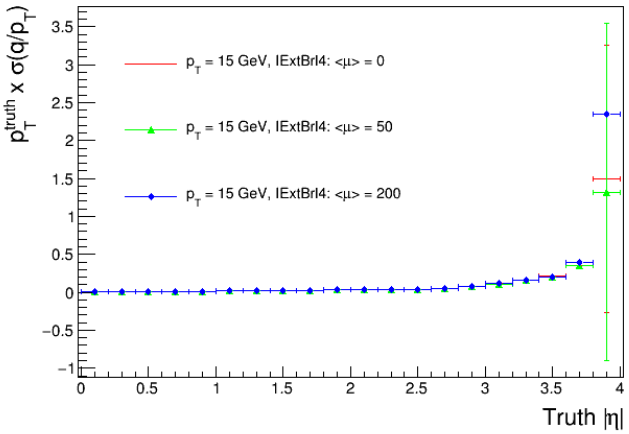

(b)

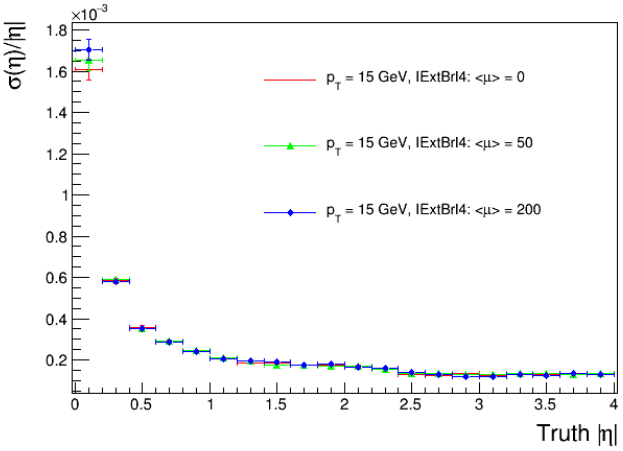

(c)

Figure 5.22: Resolution of the reconstructed track p_T, q/p_T and η for the IExtBrl4 layout, with a pion $p_T = 15$ GeV in different pile-up scenarios.

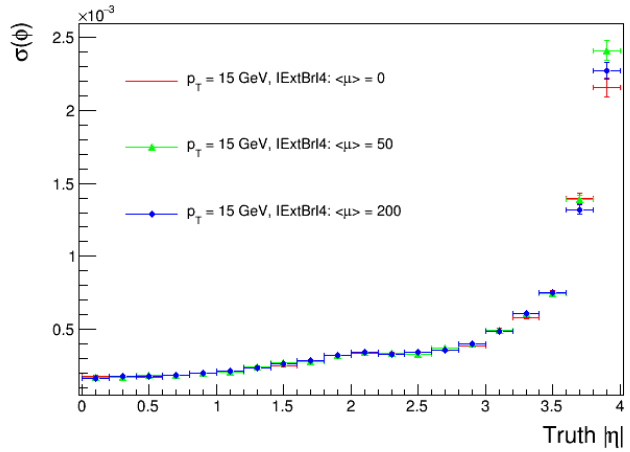

(a)

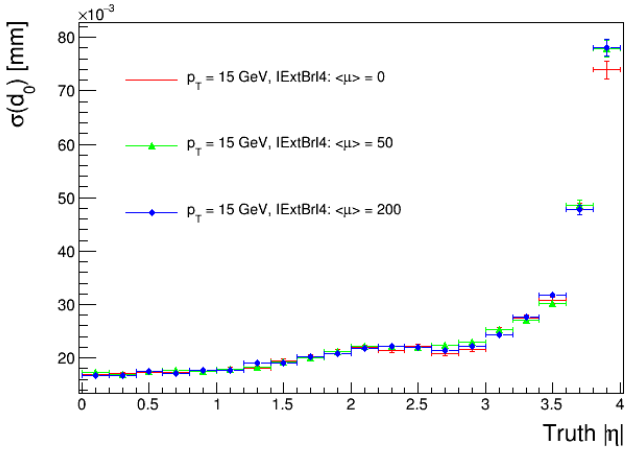

(b)

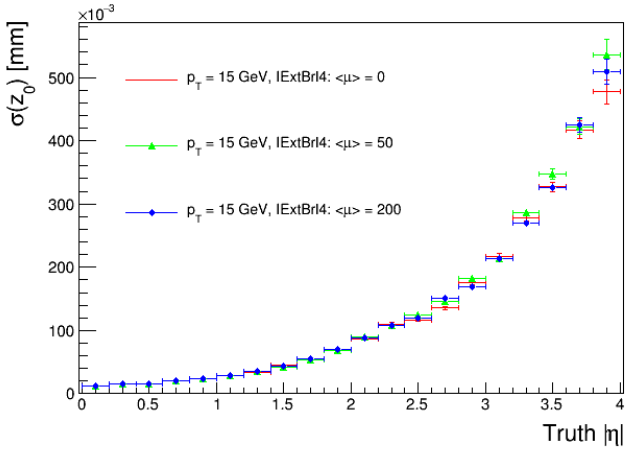

(c)

Figure 5.23: Resolution of the reconstructed track ϕ, d_0 and z_0 for the IExtBrl4 layout, with a pion $p_T = 15$ GeV in different pile-up scenarios.

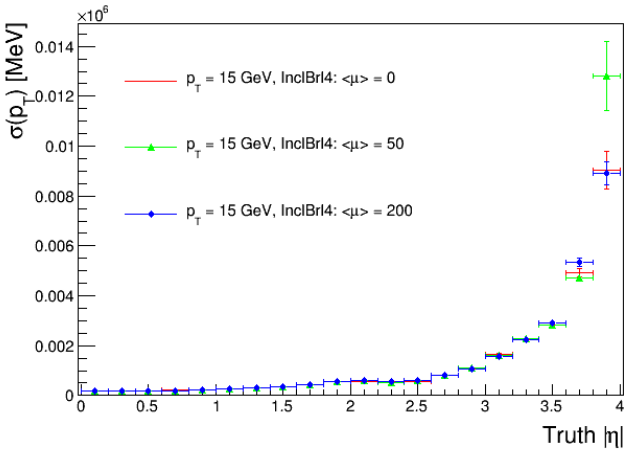

(a)

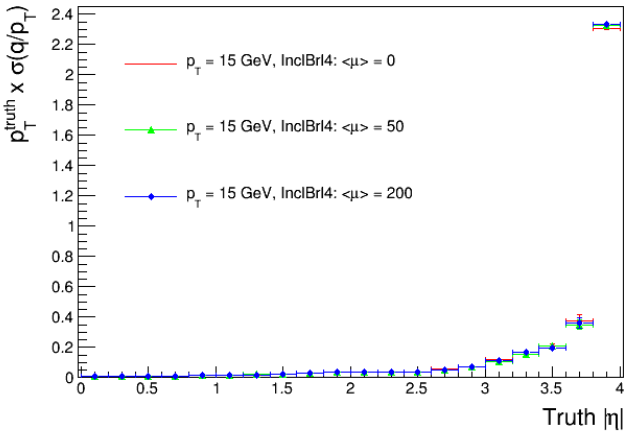

(b)

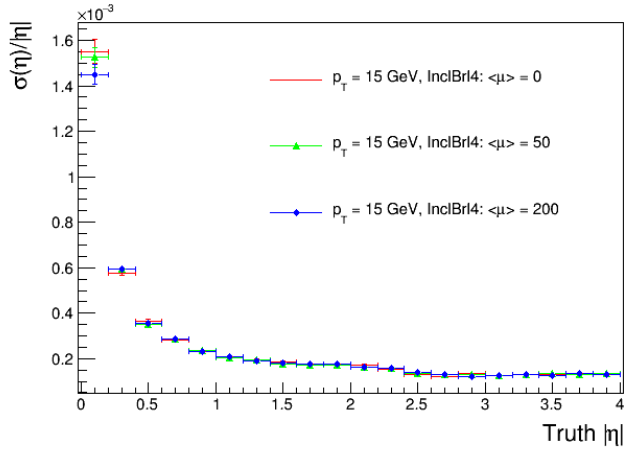

(c)

Figure 5.24: Resolution of the reconstructed track p_T, q/p_T and η for the InclBrl4 layout, with a pion $p_T = 15$ GeV in different pile-up scenarios.

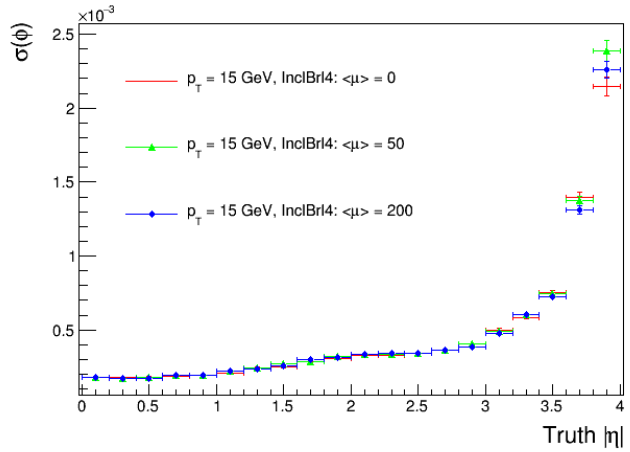

(a)

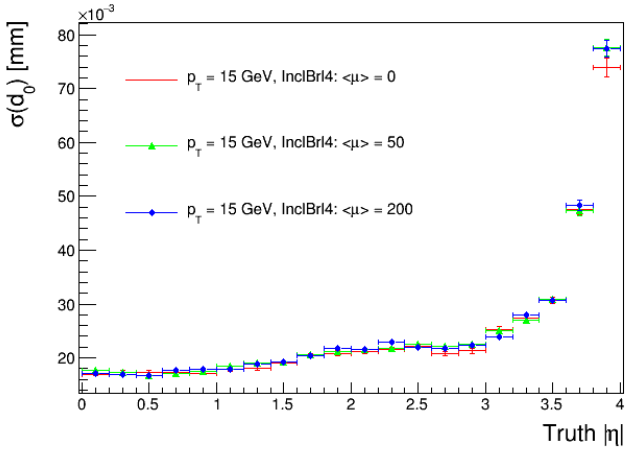

(b)

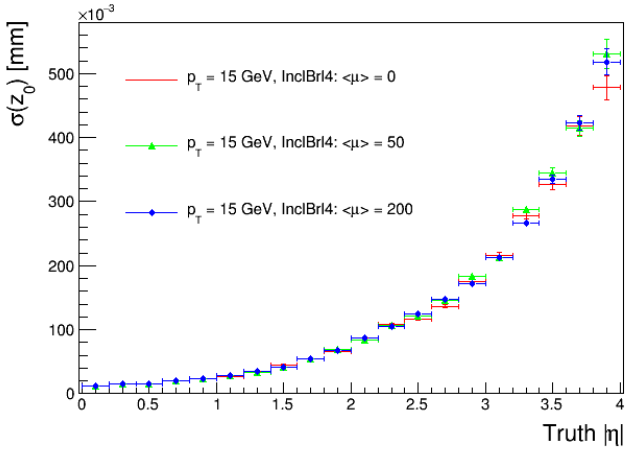

(c)

Figure 5.25: Resolution of the reconstructed track ϕ, d_0 and z_0 for the InclBrl4 layout, with a pion $p_T = 15$ GeV in different pile-up scenarios.

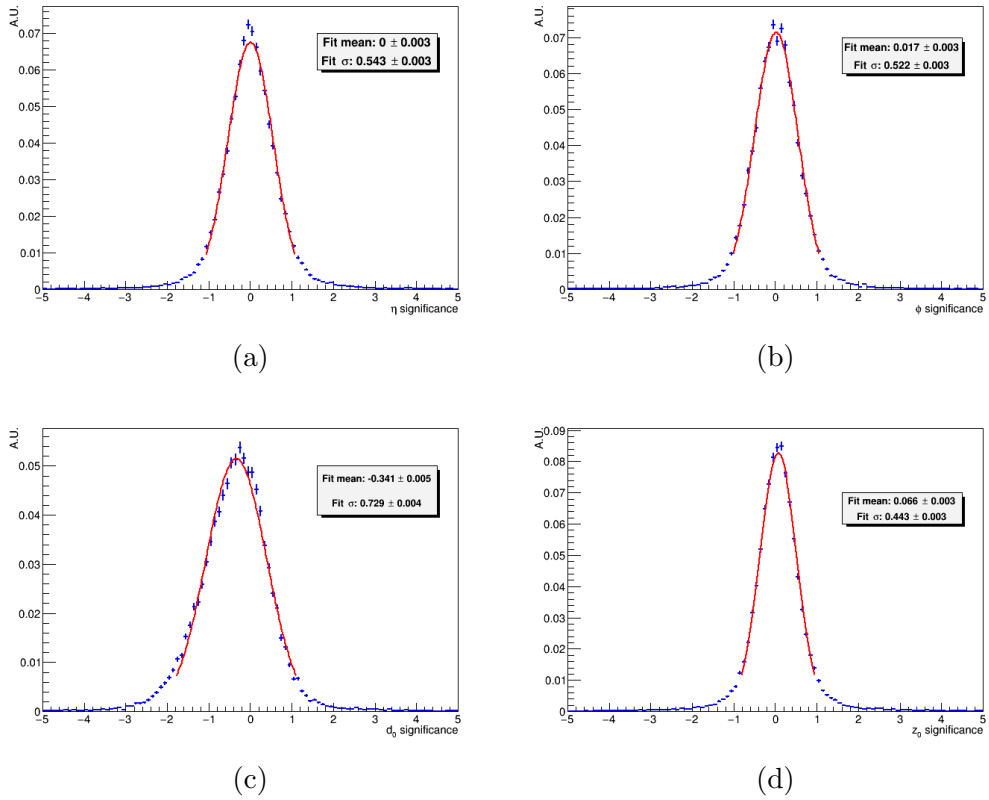

Figure 5.26: Distribution of the significance of the different reconstructed track parameters, in the sample with $p_T = 15$ GeV and $\langle\mu\rangle = 200$, for the InclBrl4 layout. The uncertainties shown are taken from the fit covariance matrix.

was due to η asymmetries in the detector geometry, we also looked at the d_0 significance distribution separately for tracks with $\eta > 0$ and $\eta < 0$, but no significant difference was found.

Finally, to compare the performances of our layouts at large momentum with the Collaboration requirements (Fig.5.1), we consider the $p_T = 100$ GeV sample. Fig.5.27 shows the resolutions in q/p_T, d_0 and z_0 in the central $|\eta|$ region. The measured d_0 resolution, as described in appendix A, is the sum of the intrinsic resolution and the transverse dimension of the beamspot (~ 12 μm for the particle gun[2]). Thus, our findings confirm that the ITk requirements are fulfilled for all the different layouts. It is important to remember that, at Step-1, it is too early to choose among the layouts, because

[2]The primary vertex smearing is hard-coded inside the simulation algorithm. It parameters are $\sigma_x = \sigma_y = 12$ μm and $\sigma_z = 50$ mm.

of the limited description of the passive material and services, and the not yet optimized reconstruction algorithm.

5.9 Fake tracks

There is no unique way to define a fake track, which should in general represent a track that was badly reconstructed. As the samples were produced using a fast simulation technique that only includes the particles inside a region of interest around the generated particle, it is not possible to measure the total fake rate but only what will from now on be referred as the **fake probability**, which is defined as the probability of a matched track to be fake.

The standard way to define a fake track in the ITk community is based on the determination of the fraction of hits common to the track and the truth divided by the number of total hits, with the pixel hits being weighed twice with respect to the SCT hits to take into account that a pixel hit has two coordinates:

$$f = \frac{2N_{pixel,common} + N_{SCT,common}}{2N_{pixel,tot} + N_{SCT,tot}}$$

In this definition, a fake track is defined as a track with $f < 50\%$. Unfortunately the detailed information on the clusters is lost in the xAOD file and such analysis should be performed directly on the AOD file which is produced at the end of the reconstruction stage[3]. We studied an operative definition based on the distribution of the ΔR distance between the matched track and the generated pion. Plot in Fig.5.28, which refers to a sample with a $p_T = 15$ GeV generated pion, $\langle\mu\rangle = 0$ in the InclBrl4 layout, shows that two ΔR regions are identifiable. The region with $\Delta R_{truth-track} < 0.02$ appears to be approximately made by two exponentials, whereas at the right of that, the distribution is approximately flat. This critical value has been measured in all the samples and appeared to depend only on the p_T of the generated pion. In particular, for the samples with a generated pion of $p_T = 5$ GeV this value was 0.04, for $p_T = 15$ GeV it was 0.02, for $p_T = 50$ GeV it was 0.01 and for $p_T = 100$ GeV the measured value was 0.006. No significant dependence on

[3] A software package based on the InDetPhysValMonitoring package was used to measure the fraction of fake tracks (matched and unmatched) using this definition. The results were around the $3 \cdot 10^{-4}$ level, but they are not realistic because of the region of interest selection applied in these samples.

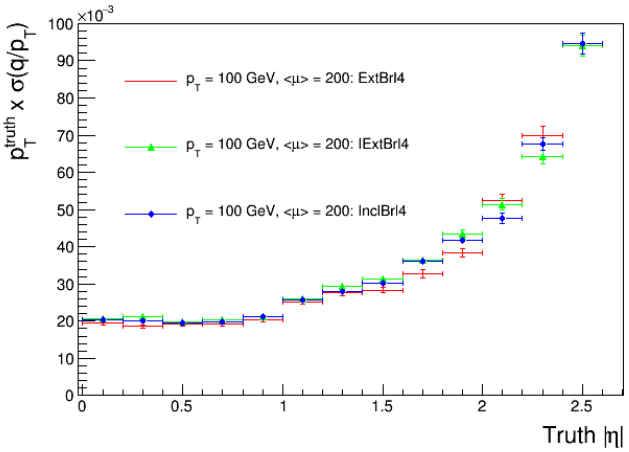

(a)

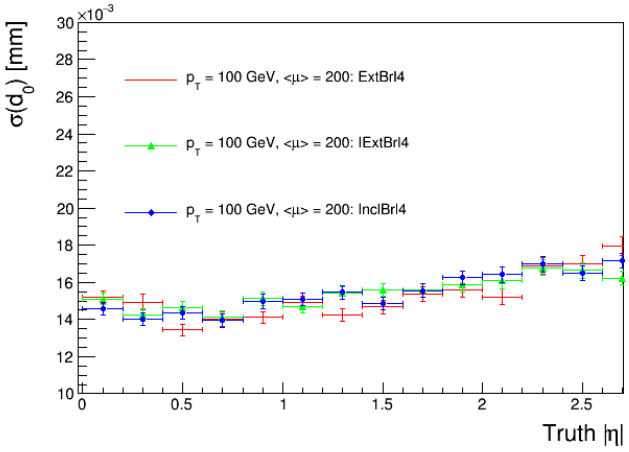

(b)

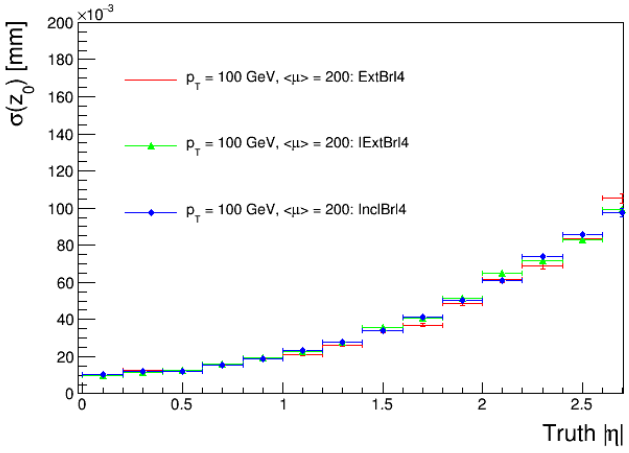

(c)

Figure 5.27: q/p_T, d_0 and z_0 resolutions of the three layouts in the central regions, at pion $p_T = 100$ GeV, in the $\langle\mu\rangle = 200$ scenario.

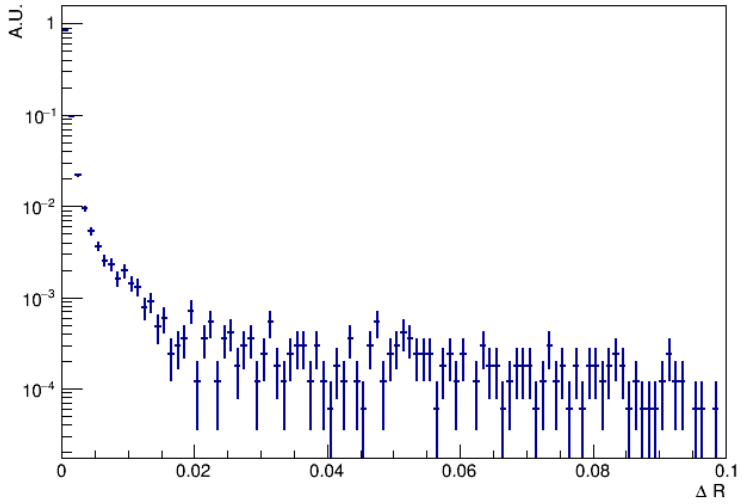

Figure 5.28: ΔR distance between the matched track and the hard-scatter pion, at $p_T = 15\ GeV$, $\langle\mu\rangle = 0$.

the average number of pile-up events or the layout was observed. By defining a **fake track** as a track in which the $\Delta R_{truth-track}$ is larger than this critical value, we are essentially selecting the tracks which are reconstructed with a distance from the "particle gun" which is large compared to the track angular resolution. As this resolution also depend on η, as shown in Fig. 5.14c, 5.15a, this critical value is an average over the whole angular spectrum.

The dependence of the fake probability on the track $|\eta|$ is shown, for the InclBrl4 layout, in Fig.5.29, for a generated pion with $p_T = 15$ GeV, for different values of $\langle\mu\rangle$. Due to the small fake probability and statistics, no significant dependence on the average number of pile-up events is observed in any η bin at fixed p_T. To minimize the uncertainty, the fake probability is computed by integrating over the whole η spectrum. Tab.5.4 summarizes the results for the three layouts considered, as a function of the generated pion p_T and average number of pile-up events. The total fake probability increases with p_T, is stable against pile-up within statistical uncertainties (all differences are $\lesssim 1\sigma$), and is significantly greater for the ExtBrl4 layout, whereas the others show similar performances. Note that these results depend on the definition of fake used. As the critical ΔR value that defines the fake tracks is p_T dependent, the fake rate should not depend on the $\Delta\eta - \Delta\phi$ resolution, but on the number of outliers. With increasing p_T, the pion produces more secondary particles, thus increasing the number of outliers, which qualitat-

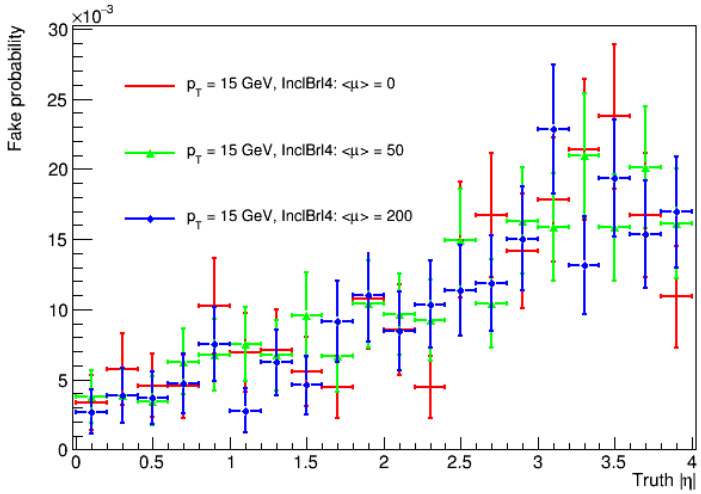

Figure 5.29: Fake probability as a function of the hard-scatter pion pseudo-rapidity for the ExtBrl4 layout, pion $p_T = 15$ GeV, as a function of $\langle\mu\rangle$.

ively justifies the result.

5.9.1 Study of the region of interest width

By definition, the fake probability should become asymptotically independent of the size of the region of interest selected in the fast simulation. When the size is small, however, a dependence could emerge for several reasons, that also depend on the definition of fake track. The size of the region of interest, which is a cone with $\Delta R = 0.1$, has first to be compared with the resolutions in η and ϕ measured in Chap.5.8, and is typically at least two order of magnitude larger. However, this alone cannot guarantee that the value chosen for the width is optimal, due to possible effects of pile-up particles outside the region of interest described in Chap.4.4. These effects are expected to become less and less significant with increasing size of the region of interest.

A study on the dependence of the fake probability on this size was carried out by generating a sample with larger cone $\Delta R = 0.2$. The time required by the simulation increases approximately with the square of the cone size, so that becomes difficult to produce samples with the large statistics necessary to assess a difference on the fake probability, which is also low. These samples

p_T	$\langle\mu\rangle$	ExtBrl4	IExtBrl4	InclBrl4
5 GeV	0	0.50 ± 0.04 %	0.35 ± 0.03 %	0.35 ± 0.03 %
	50	0.47 ± 0.04 %	0.42 ± 0.04 %	0.42 ± 0.04 %
	200	0.59 ± 0.04 %	0.46 ± 0.04 %	0.37 ± 0.03 %
15 GeV	0	1.49 ± 0.09 %	1.15 ± 0.06 %	1.11 ± 0.06 %
	50	1.49 ± 0.06 %	1.02 ± 0.05 %	1.08 ± 0.05 %
	200	1.43 ± 0.06 %	1.00 ± 0.05 %	1.06 ± 0.05 %
50 GeV	0	3.40 ± 0.09 %	2.70 ± 0.08 %	2.58 ± 0.08 %
	50	3.12 ± 0.10 %	2.49 ± 0.08 %	2.45 ± 0.08 %
	200	3.22 ± 0.09 %	2.47 ± 0.08 %	2.35 ± 0.08 %
100 GeV	0	4.1 ± 0.1 %	3.42 ± 0.10 %	3.29 ± 0.09 %
	50	4.1 ± 0.1 %	3.2 ± 0.1 %	3.1 ± 0.1 %
	200	4.3 ± 0.1 %	3.2 ± 0.1 %	3.1 ± 0.1 %

Table 5.4: Average fake probability as a function of the layout, generated pion p_T and $\langle\mu\rangle$.

were produced before the publication of the Step-1 layouts, with a similar layout that was proposed in the ATLAS Letter of Intent Document[2], in the $\langle\mu\rangle = 200$ scenario. The measured fake probability was 0.59 ± 0.05 % for the $\Delta R = 0.1$ sample and 0.63 ± 0.05 % for the $\Delta R = 0.2$ sample, which shows compatibility within the statistical uncertainties. Unfortunately, the uncertainty is large due to the small fake probability, even with the relatively high statistics generated ($5 \cdot 10^4$ events). However, no significant increase was observed, which we took as an indication that the cone size we used is reasonable, and the procedure is reliable.

5.10 Efficiency

The track reconstruction efficiency is defined, as a function of η or ϕ, as the probability of the track being correctly reconstructed (thus excluding the fake tracks) given that the hard scattering particle's η or ϕ is in a certain bin and within the detector acceptance. It is operatively computed as the ratio, for each bin, of the η or ϕ distribution of the matched tracks and the hard scatter truth, the latter being filled exclusively for the events within the geometrical acceptance. The results are shown for the three layouts, in the sample with a generated pion with $p_T = 15$ GeV, $\langle\mu\rangle = 200$ in Fig.5.30. The efficiencies are also shown as a function of the generated pion p_T and $\langle\mu\rangle$ for

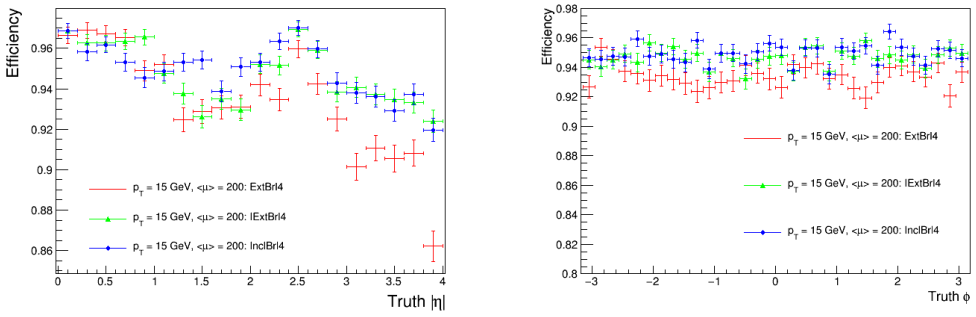

(a) (b)

Figure 5.30: Pion reconstruction efficiency in the three ITk layouts considered, in the sample with a generated $p_T = 15$ GeV and $\langle\mu\rangle = 200$.

the ExtBrl4 layout in Fig.5.31, 5.32. The uniformity of the efficiency in ϕ was tested with a χ^2 test for the three layouts, that showed compatibility with a p-value of around 20%. The total efficiency is also computed by dividing the number of matched tracks by the number of total hard-scatter truth within the detector acceptance. Results are summarized in Tab.5.5. As with the other reconstruction parameters, the IExtBrl4 and the InclBrl4 layouts perform very similarly, whereas the ExtBrl4 shows worse efficiencies, mainly in the forward region. Each layout results robust against pile-up, as no statistically significant difference was observed between the $\langle\mu\rangle = 0$ and $\langle\mu\rangle = 200$ scenarios. Also, an increase of the efficiency with increasing p_T was observed. The average efficiency for the InclBrl4 layout ranges from 93% to 96% depending on the p_T, which is also compatible with the results of the Letter of Intent Document[2] shown in Fig.5.33.

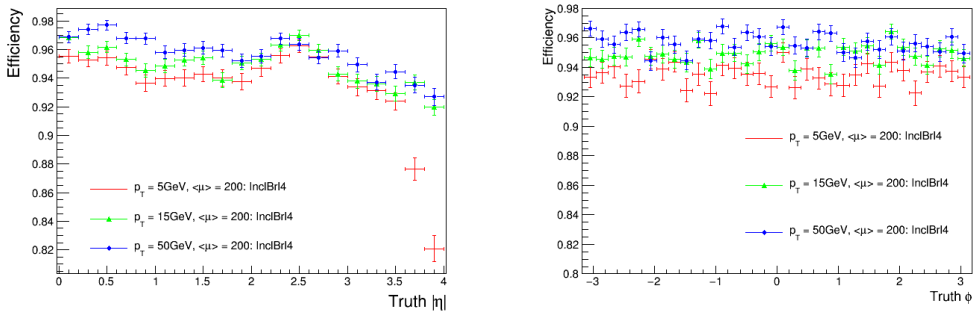

(a) (b)

Figure 5.31: Pion reconstruction efficiency in the InclBrl4 layout, in the sample with $\langle\mu\rangle = 200$, as a function of the generated pion p_T.

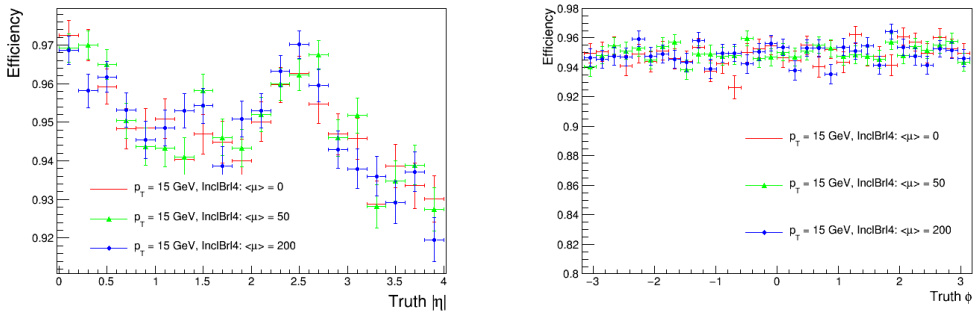

(a) (b)

Figure 5.32: Pion reconstruction efficiency in the InclBrl4, in the sample with a generated $p_T = 15$ GeV, for different $\langle\mu\rangle$.

p_T (GeV)	$\langle\mu\rangle$	**ExtBrl4**	**IExtBrl4**	**InclBrl4**
5 GeV	0	91.8 ± 0.1 %	92.9 ± 0.1 %	93.3 ± 0.1 %
	50	92.0 ± 0.1 %	93.0 ± 0.1 %	93.4 ± 0.1 %
	200	91.6 ± 0.1 %	93.0 ± 0.1 %	93.5 ± 0.1 %
15 GeV	0	93.3 ± 0.2 %	94.6 ± 0.1 %	94.9 ± 0.1 %
	50	93.4 ± 0.1 %	94.7 ± 0.1 %	95.0 ± 0.1 %
	200	93.4 ± 0.1 %	94.7 ± 0.1 %	94.9 ± 0.1 %
50 GeV	0	94.2 ± 0.1 %	95.4 ± 0.1 %	95.6 ± 0.1 %
	50	94.3 ± 0.1 %	95.3 ± 0.1 %	95.6 ± 0.1 %
	200	94.2 ± 0.1 %	95.3 ± 0.1 %	95.7 ± 0.1 %
100 GeV	0	94.5 ± 0.1 %	95.5 ± 0.1 %	95.7 ± 0.1 %
	50	94.6 ± 0.1 %	95.9 ± 0.1 %	96.0 ± 0.1 %
	200	94.0 ± 0.2 %	95.7 ± 0.1 %	95.9 ± 0.1 %

Table 5.5: Total reconstruction efficiency as a function of the layout, generated pion p_T and $\langle\mu\rangle$.

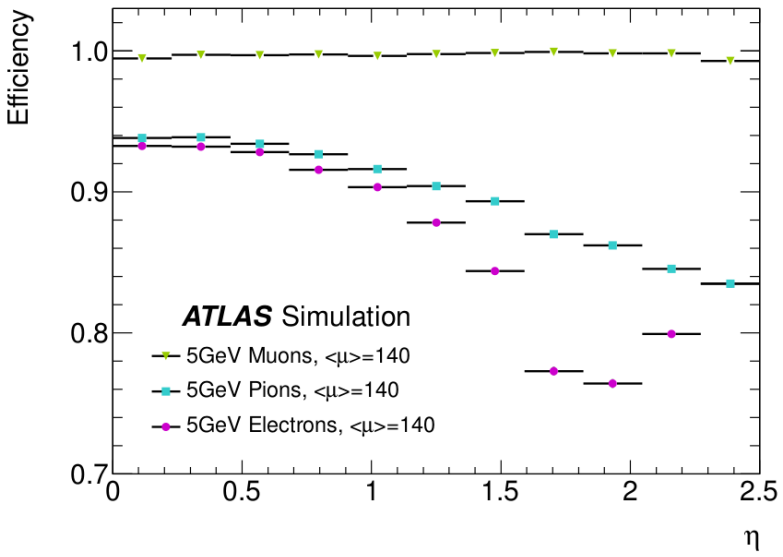

Figure 5.33: Efficiency of single muons, pions and electrons in the Letter Of Intent Document[2] layout, with $p_T = 5$ GeV and $\langle\mu\rangle = 140$.

It was also verified that there is no significant dependence of the efficiency on the generated particle charge. The results were also compared with the Letter of Intent Document[2] layout, which was different in the geometry (4 pixel + 5 SCT layers) but essentially confirm the plausibility of the results (see Fig.5.33).

5.11 Muon study

As the physics case presented in the next section uses muons as primary generated particles, it is interesting to measure their reconstruction efficiency. A sample of single muons with $p_T = 50$ GeV and $\langle\mu\rangle = 200$ was generated, and the efficiency as a function of the muon pseudo-rapidity is shown in Fig.5.34. The efficiency is essentially 100% in all η regions, except for the very forward region in which it starts to drop. The difference with respect to the pion reconstruction is due to the absence of hadronic interactions. This is also confirmed by the Letter of Intent[2] results shown in Fig.5.33.

The distribution of the ΔR between the matched tracks and the hard-scatter truth was also studied, and revealed essentially no fake tracks. The distribution is shown in Fig.5.35.

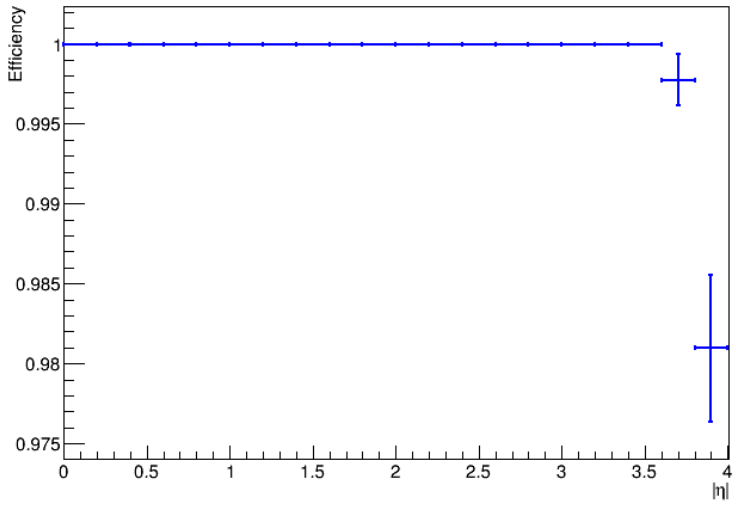

Figure 5.34: Efficiency of single muons with $p_T = 50$ GeV and $\langle\mu\rangle = 200$ in the InclBrl4 layout.

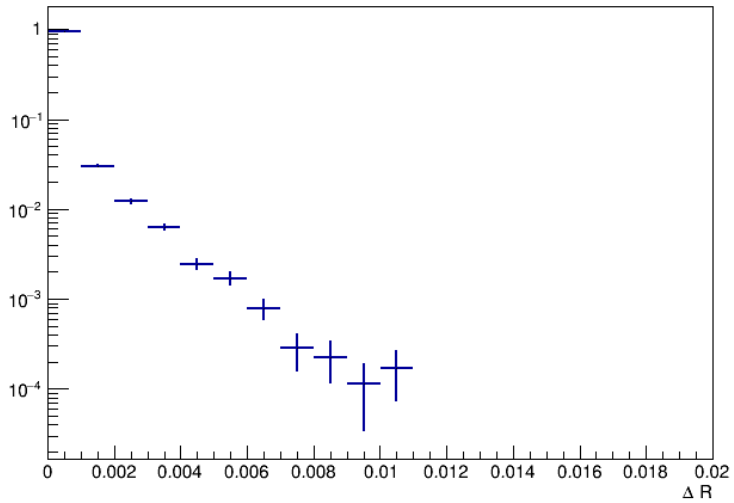

Figure 5.35: Distribution of the ΔR distance between the matched tracks and the hard-scatter muon, in the sample with a muon with $p_T = 50$ GeV, $\langle\mu\rangle = 200$, in the InclBrl4 layout.

Chapter 6

$H \to ZZ^* \to 4\mu$ performances

In this section the fast simulation technique described in Chap.4.6 is applied to the study of the physics process $gg \to H \to ZZ^* \to 4\mu$.

Performances of the detector are compared for the three layouts described in Chap.5 using the mass resolution, reconstructed track parameters (see appendix A) resolution, efficiency, fake probability and track quality. We also estimate the uncertainty on the signal strength measurement by including the effect of the background.

6.1 Motivations of the study

So far most of the measurements of the Higgs boson properties are limited by statistics. The large sample collected in the high luminosity phase will be fundamental to confirm its SM nature, and exclude (or limit) non SM contributions to its couplings.

As shown in Chap.1, in the Standard Model the main production mode of the Higgs boson is the gluon-gluon fusion (ggF) process. The second most important production mode, the vector-boson fusion (VBF), is a factor of ten less frequent and includes the associate production of two jets. The study presented in this section analyses the exclusive $gg \to H \to ZZ^* \to 4\mu$ channel (Fig.6.1), that represents a benchmark process to measure and compare the tracker performances on physics objects reconstruction among several detector configurations, while providing an important test bench for the fast simulation technique.

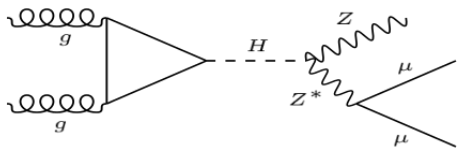

Figure 6.1: Feynman diagram of the complete production and decay process ggF $H \to ZZ^* \to 4\mu$ studied in this analysis.

In particular, this is one of the cleanest channels in which it is possible to measure the Higgs boson properties. While a full simulation including the other ATLAS sub-detectors would allow to include all the production modes, the tracker-only proposed study can only be applied to the ggF production mode and the subsequent decay into 4μ. This provides a clean tracker signature while allowing the measurement of basic tracking performance parameters such as Higgs and Z mass resolution.

6.2 ATLAS Scoping-document analysis: inclusive $H \to ZZ^* \to 4\mu$

The study of this physics channel is of particular relevance because of the cleanliness of the signature and the resulting accuracy with which it is measured at LHC. In this paragraph, the analysis of this channel performed in the ATLAS Phase II Upgrade Scoping Document[1] is summarized. This study, for sake of comparison, is the basis of our work.

The ITk layout used for the Scoping Document is different with respect to the ones described in Chap.5, but the angular coverage is the same ($|\eta| < 4.0$). Its details can be found in [1]. In this study, no specific production mode of the Higgs boson was selected. The only background considered is the irreducible dominant $ZZ^{(*)} \to 4\mu$, while the others are expected to have a small effect on the final result. The analysis requirements applied are based on those developed for the Run-1 analysis:

- the event must contain 2 pairs of candidate muons, each with 2 opposite charged tracks;
- the ordered p_T of the four muons must be larger than 20 GeV, 15 GeV, 10 GeV, 6 GeV respectively;
- the ΔR distance between the candidate muons must be > 0.1;

- The neutral muon pair with the mass closest to the Z boson is defines as the *on-shell* pair, while the remaining is defined as the *off-shell* pair; at least one of the off-shell muon candidates must lie in the region $|\eta| < 2.7$;
- the on-shell pair mass is required to lie in the mass region [50 GeV, 106 GeV];
- the off-shell pair mass must lie in the mass region [12 GeV, 115 GeV];

Furthermore, a simplified version of the Run-1 Z mass constraint is applied, considering only the effect of the p_T resolution. The overall acceptance of this channel is shown in Fig.6.2, from which it is inferable an acceptance gain of 21 % thanks to the coverage extension of the detector from $|\eta| < 2.7$ to $|\eta| < 4.0$. The results of the analysis are shown in Tab.6.1,6.2, where the performances of the three layouts proposed in the Scoping Document are compared. In the following, we describe in detail our study.

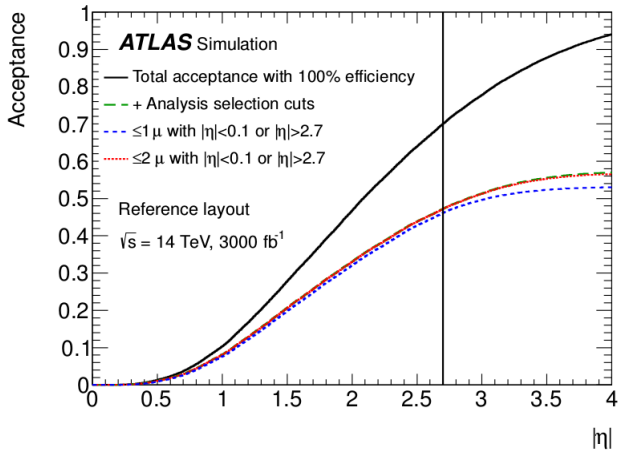

Figure 6.2: Acceptance of the channel $H \to ZZ* \to 4\mu$. The blue and red dashed lines corresponds to the angular selection in which the muon trigger is present.

6.3 Physics process generation

As described in Chap.4.6, the first step of the fast simulation technique employed is the generation of a number of proton-proton collisions containing the ggF production of a Higgs boson decaying into one on-shell and one off-shell Z boson, each of which decaying into a neutral muon pair. This production channel represents the more frequent way ($\sim$ 86% of the total

Coverage	Mass (GeV)	Width (GeV)
$\lvert\eta^{\mu}_{max}\rvert < 2.7$	124.95 ± 0.01	1.11 ± 0.01
$2.7 < \lvert\eta^{\mu}_{max}\rvert < 3.2$	125.31 ± 0.07	2.53 ± 0.08
$3.2 < \lvert\eta^{\mu}_{max}\rvert < 4.0$	125.89 ± 0.17	4.61 ± 0.23

Table 6.1: Higgs mass and width measurement, where the samples are divided into three regions, depending on the value of $|\eta|$ of the most forward muon[1]. In the Scoping Document, the only scenario with $|\eta| < 4.0$ coverage is the Reference scenario.

Scenario	$H \to 4\mu$	$ZZ^{(*)} \to 4\mu$	$\Delta\mu/\mu$
Reference	2551 ± 51	741 ± 27	0.022
Middle	2104 ± 46	351 ± 19	0.024
Low	2014 ± 45	336 ± 18	0.024

Table 6.2: Number of expected signal and background events at 3000 fb^{-1} integrated luminosity and signal strength accuracy for the three Scoping Documents ITk layouts[1].

cross section at 13 TeV) in which the Higgs boson is produced at LHC and the only one without associated production of other physics objects (usually jets). The other production modes were not taken into account for simplicity. The only background considered is the irreducible $ZZ^{(*)}$, in which each Z boson decays into two muons. The inclusion of other backgrounds are expected to have a negligible effect on the final result[1].

6.3.1 Higgs generation

The Higgs boson samples were generated with the Powheg[37] generator at 13 TeV (to make these results compatible with the ones from the Run-2 analysis) with a relativistic Breit-Wigner distribution with mean 125 GeV and $\Gamma = 4$ MeV (full width at half maximum), which is shown in Fig.6.4. Higgs boson is then forced to decay into two Z, that in turn decay into two muons each. The mass distribution of the two Z bosons is instead shown in Fig.6.5, where the Z boson with mass closest to the rest mass is defined as *on-shell* and the other as *off-shell*.

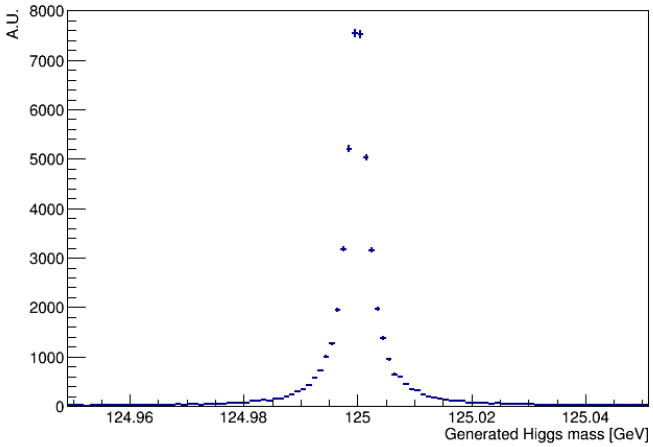

Figure 6.3

Figure 6.4: Higgs generated mass distribution.

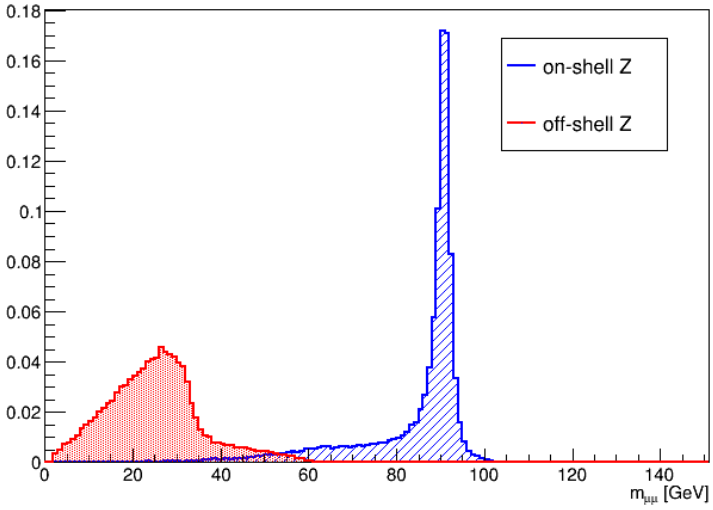

Figure 6.5: Generated mass distributions of the *on-shell* and *off-shell* Z boson in the $H \to ZZ^* \to 4\mu$ process with the Powheg generator.

6.3.2 Background process generation

In order to speed up the following simulation of the background process $ZZ^{(*)} \to 4\mu$, the generation was optimized by producing events in a selected kinematic region with the Powheg generator[37]. In particular, a minimum value of 15 GeV for the mass of the Drell-Yan produced Z^* boson was required. Moreover, the invariant mass of the four muon system is required to lie in the region between 50 GeV and 160 GeV. Values were chosen so that the 4μ system invariant mass is not affected in the region of intersection. The distribution of the generated masses is shown in Fig.6.6.

6.3.3 Selection of the generated events

The possible final states of the generated Higgs boson decay are not only the four muons that compose the signature in our channel of interest, but can be expressed as $H \to ZZ^* \to 4\mu + X$, where X are usually final state photons emitted in the radiative decay of the Z boson. Sometimes these photons are also converted in e^+e^- pairs. Fig.6.7 shows the distribution of the p_T and the number of photons per event. As this analysis is carried out by only considering the tracker reconstruction capabilities, to ensure an appropriate reconstruction of the physics objects a selection on the generated events was applied. Before selection, the Higgs boson decays were categorized into five mutually exclusive categories, whose frequency and kinematic features were separately studied. In the following list, the number between parentheses shows the relative frequency of that particular channel (no threshold on p_T applied):

- 4μ channel (25%);
- $4\mu + N\gamma$ channel, $N \geq 1$ (74.5%);
- $4\mu + e^+e^- + X$ channel (0.5%);
- $4\mu + X$ channel, $X \neq \gamma, e$ ($\sim 10^{-5}$);
- $N\mu + X$, $N \neq 4$ (0.06%).

As the detector is not always able to discriminate among these categories, the chosen selection attempts to include all the events that can be reconstructed as purely leptonic from the detector, thus including all the events from the first category and the ones from the second category passing a kinematic selection. The exclusion of the other categories relies on the approximation

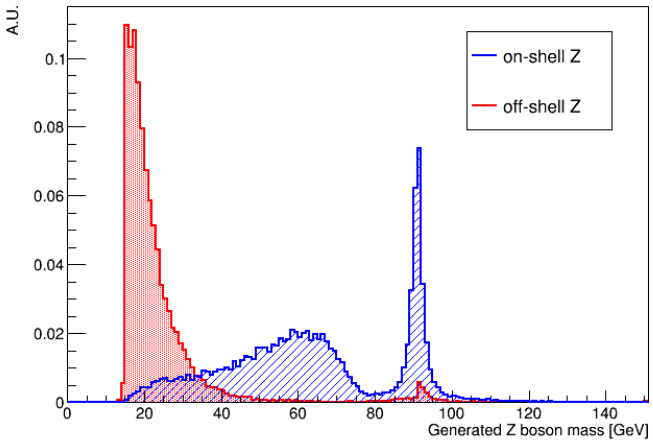

(a)

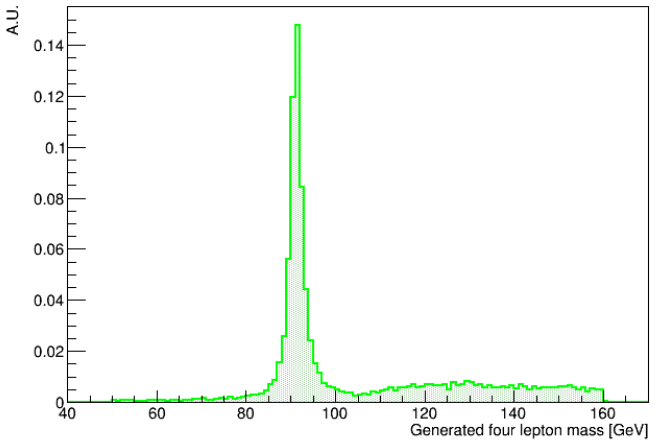

(b)

Figure 6.6: (a): Z boson generated distributions in the $ZZ^{(*)} \to 4\mu$ process, generated with Powheg;
(b): Mass distribution of the system of four leptons in the $ZZ^{(*)} \to 4\mu$ process, generated with Powheg.

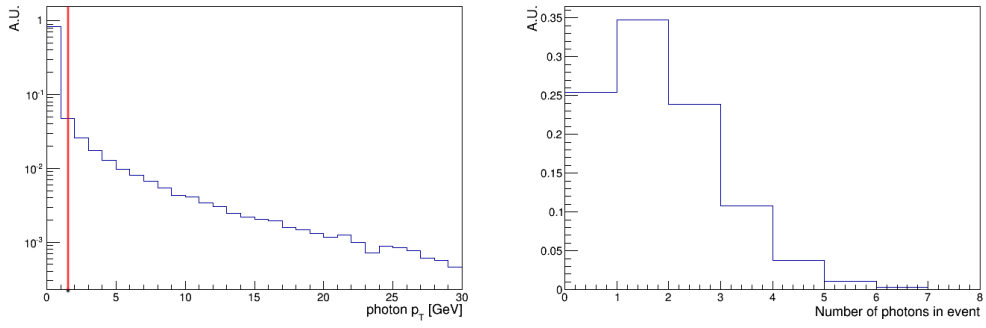

(a) (b)

Figure 6.7: (a): p_T spectrum of radiative photons of the process $gg \to H \to ZZ^* \to 4\mu$. The line marks the selection threshold; (b): histogram of the number of photons emitted per event.

that charged particles are reconstructed in the tracker. This is not true if the p_T of the particle is too low or if it lies outside the geometrical acceptance of the detector. The failure of one of these assumptions is, however, not expected to determine a significant change in the physics object reconstruction parameters (resolution, efficiency, etc.), because of the small fraction of these events inside the sample and their kinematic properties.

During the ATLAS Run-1 analysis the electromagnetic calorimeter was used to account for the system invariant mass in presence of photons[38]. In this analysis, we used a simplified version of this selection, assuming that the same can be done in the HL-LHC conditions. The selection excludes all events in which at least one photon has $p_T^\gamma > 1.5$ GeV. The η distribution and the ΔR distance of the photon from the muon after the application of this requirement is shown in Fig.6.8.

Thanks to the inclusion of the events from this category the generated events acceptance was measured to increase approximately from 25% to 80%.

6.4 Signal event simulation and truth analysis

The kinematics of the muons passing the generation selection for the signal sample is shown in Fig.6.9,6.10. In particular, a geometrical acceptance of

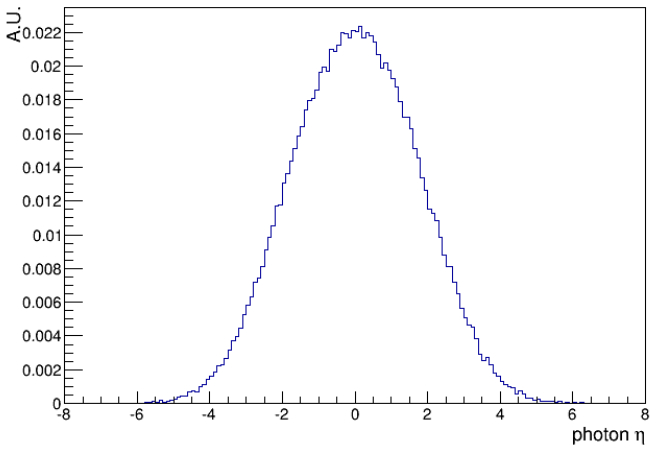

(a)

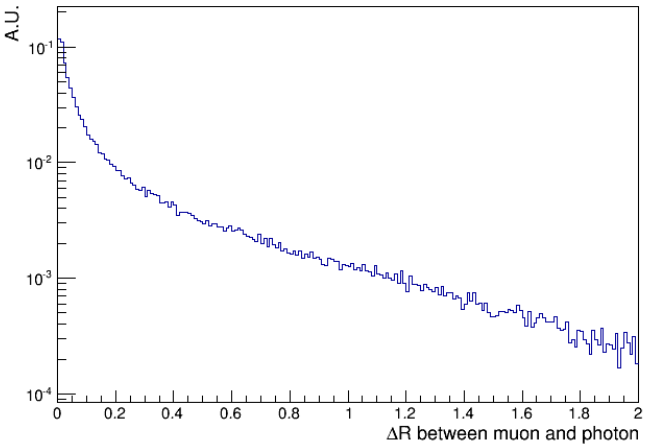

(b)

Figure 6.8: (a): η spectrum of radiative photons of the process $gg \to H \to ZZ^* \to 4\mu$ with $p_{T,\gamma}^{max} < 1.5$ GeV; (b): distribution of the ΔR distance between the muons and their emitted photons in events with $p_{T,\gamma}^{max} < 1.5$ GeV.

94.1% is inferable from the number of events in which all muons are within the detector coverage. It is also evident, from the p_T spectrum, the shoulder due to the decays of the on-shell Z.

Samples of $5 \cdot 10^4$ events were produced from the selected generated events by running the simulation/digitization/reconstruction chain described in Chap.4.4, in two pile-up scenarios $\langle\mu\rangle = 0$ and $\langle\mu\rangle = 200$, and for the three ITk layouts described in Chap.5 (referred as ExtBrl4, IExtBrl4 and InclBrl4). Unless otherwise specified, the plots refer to the $\langle\mu\rangle = 200$ sample, which is the reference value for the HL-LHC operations. For events in which the particles are within the detector acceptance, the distribution of the number of primary charged particles and the number of reconstructed tracks per event is shown in Fig.6.11. The difference between the two distributions (see Fig.6.11b) is mostly due to reconstruction inefficiency for pile-up tracks.

Identification of the truth event and track matching

At the end of the reconstruction stage, the output file contains both the truth and the reconstructed track information. For each event, the first step is to identify the Higgs boson decay products in the truth particles. To do so, for every event it was looked for four muons coming from the same vertex with zero total charge, which will referred from now on as **hard-scatter truth** muons. The extremely unlikely event in which more than one truth vertex contains four muons with null total charge is also taken into account. In this case the hard-scatter vertex is chosen as the one in which its outgoing particles have the invariant mass closest to the Higgs boson mass.

The next step is to find an appropriate **track matching** to every hard-scatter truth muon. There are several ways to define a match, which depend on the study. In the following a match is found by looking, for every hard-scatter truth muon, for the track whose *back-link* points to it, for every event in which all the muons are within the detector acceptance. This link is available at reconstruction level and connects a reconstructed track with a truth particle based on the value of the so called *truth match probability*. This variable is based on the ratio between the number of clusters correctly associated to the truth particle and the total number of clusters forming the track. The definition still employs a weight system to account for the different Inner Detector sections, which was optimized for the Run-1 reconstruction with the presence of the TRT. Despite not being yet optimized for HL-LHC, it can be used for our purposes.

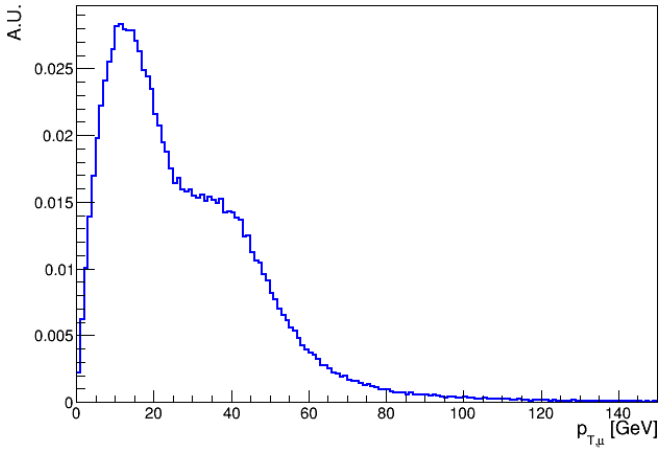

(a)

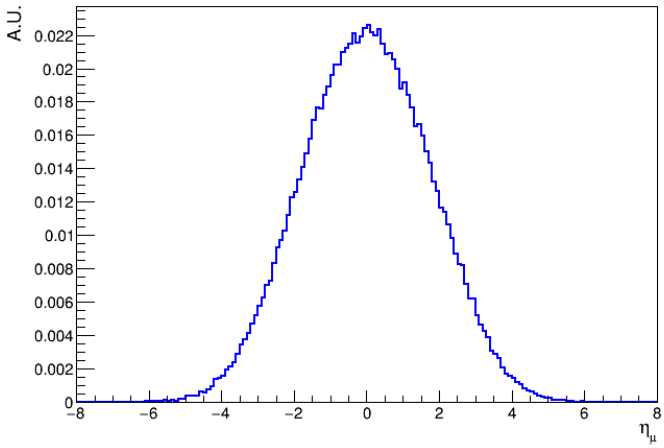

(b)

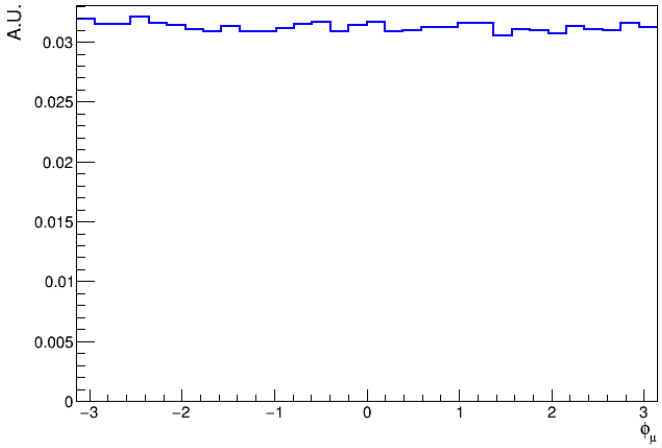

(c)

Figure 6.9: (a): p_T distribution of the muons passing the generation selection;
(b): η distribution of the muons passing the generation selection;
(c): ϕ distribution of the muons passing the generation selection.

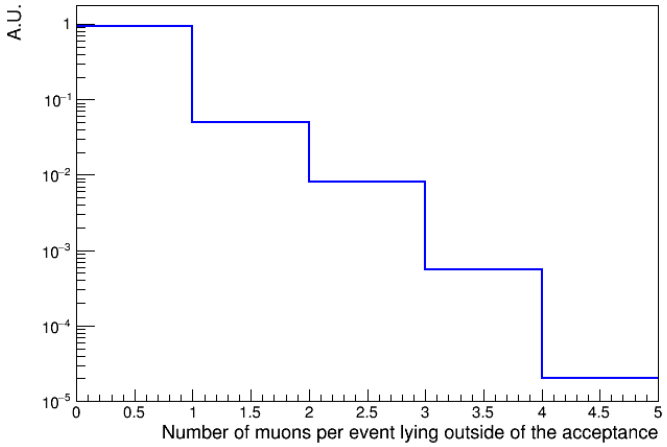

Figure 6.10: Histogram of the number of muons per event lying outside of the detector acceptance ($|\eta| > 4.0$);

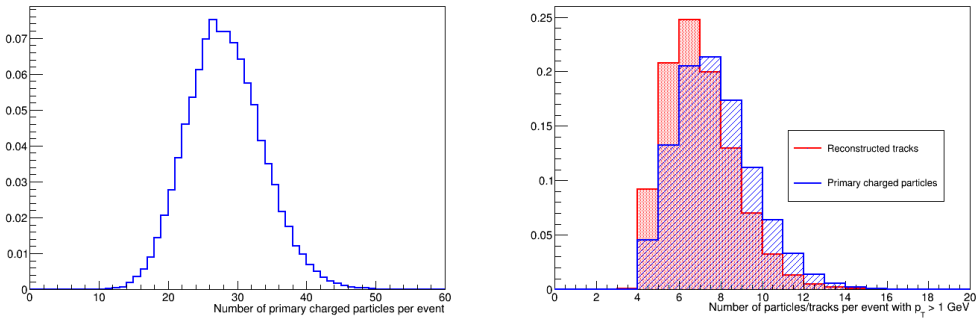

(a) (b)

Figure 6.11: (a): Number of primary charged particles in the events within the acceptance;
(b): Number of primary charged particles/reconstructed tracks with $p_T > 1\ GeV$ in the events within acceptance; the reconstructed tracks are shown, as an example, for the InclBrl4 layout.

6.5 Hard-scattering muons tracking performances

From the comparison between the kinematic distributions of the hard-scattering truth muons and the correspondent matched tracks it is possible to define basic tracking performance parameters, such as resolutions and efficiencies.

Resolution

The resolution of the generic variable x (usually one of the reconstructed track parameters, see appendix A) as a function of $|\eta|$ is defined, for every hard-scatter muon, from the distribution of the residual $\Delta_x = x_{matched} - x_{truth}$ for different $|\eta_{truth}|$ bins, as done in the study presented in Chap.5.8. The results for the hard-scatter muons are shown in Fig.6.12,6.13. The resolution tends to worsen with increasing pseudo-rapidity for reasons already discussed in Chap.5. In general, the ExtBrl4 layout shows worse performances in the forward region where, due to longer clusters, the algorithm for hit reconstruction in ITk does not perform well.

Track quality

The distribution of the number of *total silicon hits*[1] is shown separately for truth-matched tracks and pile-up tracks in Fig.6.14.

6.6 Physics analysis

To compare with the results of the Scoping document, that are based on different layouts and briefly summarized in Chap.6.2, similar analysis requirements were applied.

6.6.1 Identification of the track candidates

An initial set of tracks is selected by stacking into a vector all the tracks passing a minimum p_T requirement of 6 GeV and with at least 10 hits (Pixel + SCT) to minimize the fake rate. Our signal consists of four muons coming

[1] Here with total silicon hits it is meant the sum of the number of clusters in the Pixel and SCT layers.

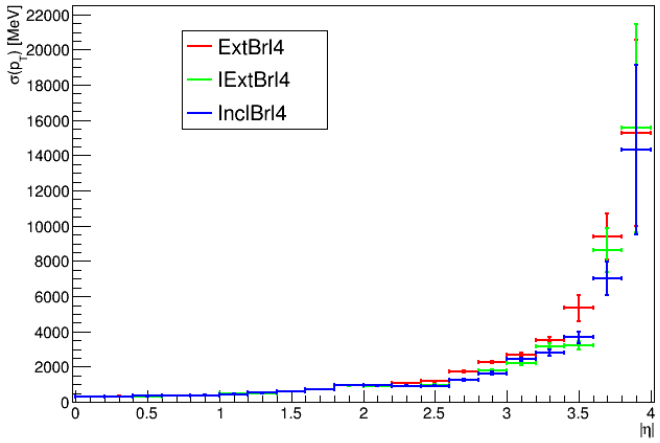

(a)

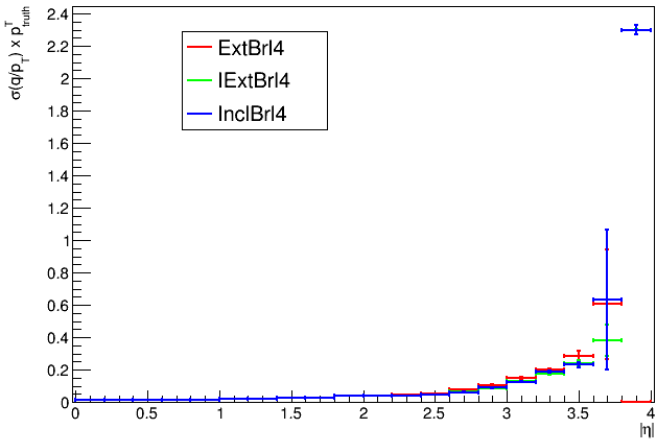

(b)

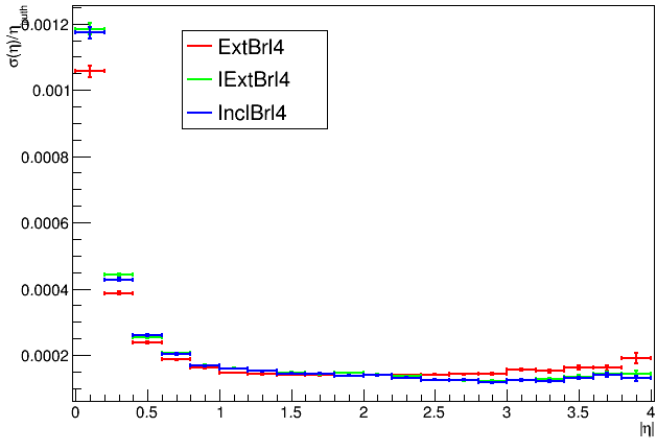

(c)

Figure 6.12: Resolution of the reconstructed muon matched track p_T, q/p_T and η for the three ITk layouts considered, in the sample with $\langle\mu\rangle = 200$, in the process $H \to ZZ^* \to 4\mu$.

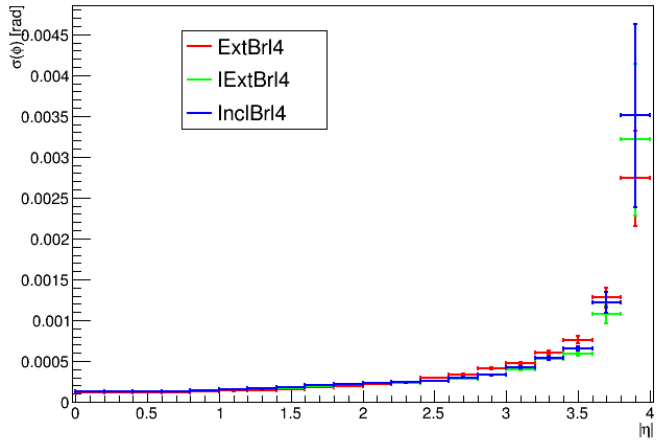

(a)

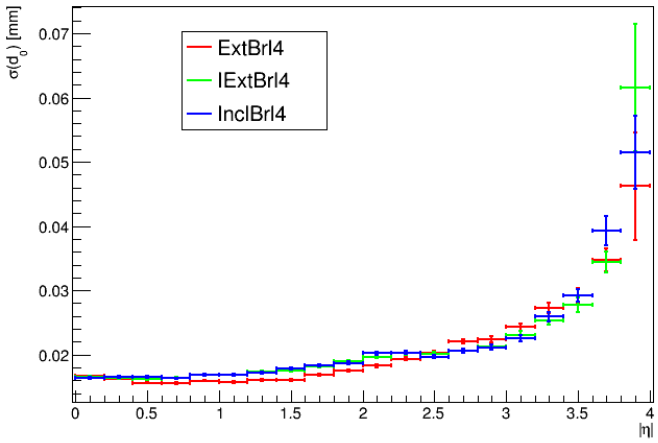

(b)

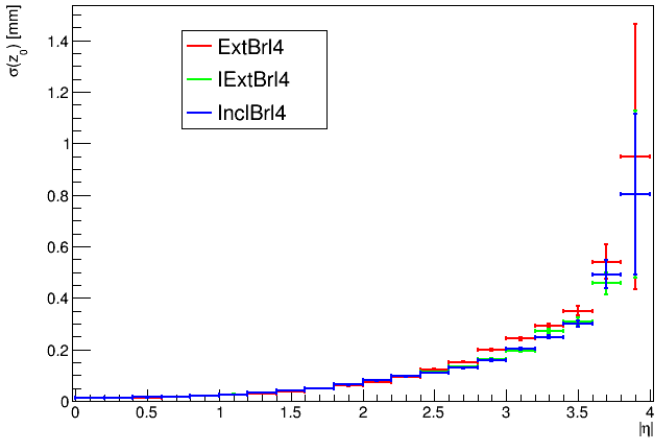

(c)

Figure 6.13: Resolution of the reconstructed muon matched track ϕ, d_0 and z_0 for the three ITk layouts considered, in the sample with $\langle\mu\rangle = 200$, in the process $H \to ZZ^* \to 4\mu$.

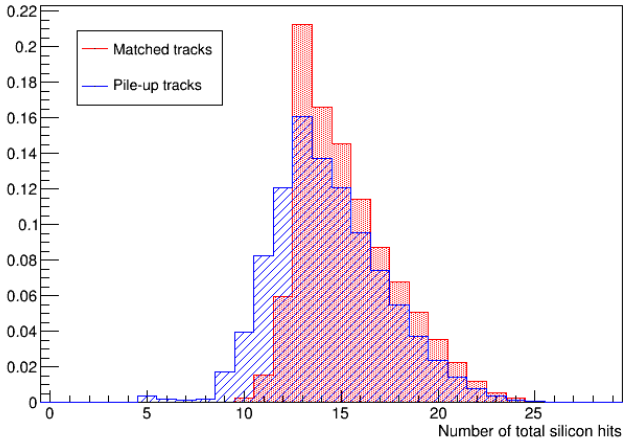

Figure 6.14: Distribution of the number of total silicon hits for truth-matched and pile-up tracks.

from the primary vertex. As no primary vertex finding algorithm is available in the reconstruction algorithm, a selection was applied on the distance between the track z_0 parameter and the true primary vertex z position. As the z_0 resolution heavily depends on the track pseudorapidity, as can be seen in Fig. 6.13c, the selection was applied in the following way:

$$|z_0\ (track) - z\ (truth\ primary\ vertex)| < 5 \times \sigma_z(\eta)$$

with $\sigma_z\ (\eta) = 50\ \mu$m for $|\eta| < 2.7$, 150 μm for $2.7 < |\eta| < 3.2$ and 500 μm for $3.2 < |\eta| < 4.0$.

A very loose isolation requirement was then applied to further reduce the rate of events in which more than four tracks pass all the requirements, which is similar to the one used during the Run-1 analysis[38]. It was applied by requiring that the sum of the p_T of the tracks inside a cone of size $\Delta R = 0.1$ around the muon candidate, divided by its p_T is smaller than 1. This requirement was kept loose as it is well known that isolation is strongly dependent on pile-up tracks and it has not yet been optimised for HL-LHC.

At this point, it was verified that the fraction of events in which more than four tracks pass all the requirements is $\lesssim 10^{-4}$. For sake of generality, the worst case was also taken into account. In this case, combinations of four tracks are formed first excluding the ones that do not form an electrically neutral system. Then, subsequent selections are applied to the combinations, starting from the transverse momenta requirements. If more than one

combination pass the selection, the one with the highest four-muon mass is chosen. This could result in the introduction of a bias, but it is not a worrying issue in this analysis due to the extreme rarity of this event.

The remaining requirements are applied sequentially in the same order as described in Chap.6.2.

6.6.2 Reconstruction efficiencies

The selection efficiencies were studied for the signal and background samples, in the $\langle\mu\rangle = 200$ scenario. They are summarized in Tab.6.3. In Tab.6.4, 6.5, 6.6 results are shown for the three different regions $|\eta_\mu^{max}| < 2.7$, $2.7 < |\eta_\mu^{max}| < 3.2$ and $3.2 < |\eta_\mu^{max}| < 4.0$. These three regions are relevant as they corrsepond to a "Run-1-like" scenario and to two possible extensions. Therefore it is important to assess the different capabilities of the three layouts.

	ExtBrl4		**IExtBrl4**		**InclBrl4**	
	Higgs	**ZZ**	**Higgs**	**ZZ**	**Higgs**	**ZZ**
Number of tracks	0.992	0.975	0.991	0.970	0.991	0.971
Hits	0.995	0.985	0.999	0.998	0.999	0.997
$\boldsymbol{p_4^T}$	0.700	0.590	0.715	0.614	0.717	0.615
$\boldsymbol{\Delta z}$	0.959	0.935	0.969	0.950	0.971	0.952
Isolation	0.987	0.990	0.988	0.990	0.987	0.990
Charge	0.996	0.992	0.994	0.989	0.995	0.987
$\boldsymbol{p_1^T}$	0.991	0.935	0.990	0.934	0.990	0.930
$\boldsymbol{p_2^T}$	0.981	0.944	0.981	0.941	0.981	0.946
$\boldsymbol{p_3^T}$	0.967	0.905	0.967	0.903	0.966	0.901
Off-shell muons	0.983	0.952	0.978	0.939	0.977	0.936
On-shell mass	0.990	0.844	0.991	0.842	0.991	0.840
Off-shell mass	0.920	0.996	0.921	0.996	0.921	0.996
Total efficiency	0.548	0.332	0.565	0.345	0.566	0.344

Table 6.3: Relative and total selection efficiencies for the three ITk layouts considered. Relative efficiencies are defined as the fraction of events passing the selection from the previous step, while the total efficiency is the fraction of events passing all the requirements with respect to the total number of generated events. The uncertainty on the total efficiency is not shown for graphical clarity and it is 0.002 for the Higgs sample and 0.003 for the ZZ sample.

	ExtBrl4		IExtBrl4		InclBrl4	
	Higgs	**ZZ**	**Higgs**	**ZZ**	**Higgs**	**ZZ**
Number of tracks	1.000	1.000	1.000	1.000	1.000	1.000
Hits	1.000	1.000	1.000	1.000	1.000	1.000
$\boldsymbol{p_4^T}$	0.783	0.721	0.782	0.723	0.785	0.722
$\boldsymbol{\Delta z}$	0.972	0.964	0.976	0.962	0.977	0.967
Isolation	0.987	0.992	0.987	0.992	0.987	0.992
Charge	1.000	1.000	1.000	1.000	1.000	1.000
$\boldsymbol{p_1^T}$	0.995	0.949	0.995	0.949	0.995	0.947
$\boldsymbol{p_2^T}$	0.987	0.952	0.987	0.951	0.987	0.953
$\boldsymbol{p_3^T}$	0.973	0.912	0.973	0.912	0.972	0.911
Off-shell muons	1.000	1.000	1.000	1.000	1.000	1.000
On-shell mass	0.997	0.846	0.997	0.848	0.997	0.843
Off-shell mass	0.918	0.998	0.918	0.998	0.918	0.998
Partial efficiency	0.657	0.480	0.659	0.480	0.661	0.480
Total efficiency	0.459	0.249	0.460	0.249	0.462	0.248

Table 6.4: Relative and total selection efficiencies for the three ITk layouts considered, only for the events with $|\eta^{\mu}_{max}| < 2.7$. Relative efficiencies are defined as the fraction of events passing the selection from the previous step. Partial efficiency is the fraction of events passing the selection with respect to the total number of generated events in the kinematic region. Total efficiency is the fraction of events passing the selection with respect to the total number of generated events. The uncertainty on the total efficiency is not shown for graphical clarity and it is 0.003 for the Higgs sample and 0.005 for the ZZ sample.

Results show that the Inclined (IExtBrl4) and Fully Inclined (InclBrl4) layouts perform similarly, whereas the Extended (ExtBrl4) layout shows slightly worse efficiencies, due to the worse p_T and z_0 resolution in the forward region.

The dependency on the number of simulated pile-up events was also studied comparing these efficiencies with a $\langle\mu\rangle = 0$ sample, and the corresponding results are shown in Tab.6.7, 6.8, 6.9, 6.10. The uncertainties indicated are statistical and include generation and simulation fluctuations, but the hard-scatter event sample in the two pile-up scenarios is the same, so that uncertainties are correlated. A weak systematic decrease of the efficiency with the pile-up appears to be present, which can be indication of resolution degradation, but it is not statistically significant.

	ExtBrl4		IExtBrl4		InclBrl4	
	Higgs	**ZZ**	**Higgs**	**ZZ**	**Higgs**	**ZZ**
Number of tracks	1.000	1.000	1.000	1.000	0.999	1.000
Hits	0.994	0.991	1.000	1.000	1.000	1.000
$\boldsymbol{p_4^T}$	0.628	0.625	0.697	0.686	0.699	0.695
$\boldsymbol{\Delta z}$	0.928	0.895	0.954	0.938	0.957	0.944
Isolation	0.991	0.993	0.991	0.991	0.990	0.990
Charge	1.000	0.998	1.000	1.000	1.000	1.000
$\boldsymbol{p_1^T}$	0.977	0.915	0.977	0.915	0.977	0.907
$\boldsymbol{p_2^T}$	0.962	0.933	0.961	0.934	0.964	0.937
$\boldsymbol{p_3^T}$	0.951	0.886	0.951	0.885	0.947	0.879
Off-shell muons	0.965	0.942	0.956	0.937	0.957	0.937
On-shell mass	0.979	0.853	0.986	0.848	0.988	0.849
Off-shell mass	0.924	0.993	0.926	0.996	0.926	0.995
Partial efficiency	0.448	0.33	0.513	0.38	0.516	0.38
Total efficiency	0.056	0.046	0.064	0.053	0.064	0.053

Table 6.5: Relative and total selection efficiencies for the three ITk layouts considered, only for the events with $2.7 < |\eta^{\mu}_{max}| < 3.2$. Relative efficiencies are defined as the fraction of events passing the selection from the previous step. Partial efficiency is the fraction of events passing the selection with respect to the total number of generated events in the kinematic region. Total efficiency is the fraction of events passing the selection with respect to the total number of generated events. The uncertainty on the total efficiency is not shown for graphical clarity and it is 0.006 for the Higgs sample and 0.01 for the ZZ sample.

6.6.3 Higgs reconstruction performance

As described, events passing the analysis requirements were divided into three kinematic regions, depending on the $|\eta|$ value of the most forward muon candidate. This is useful to compare the reconstruction resolution and the signal significance as a function of the detector coverage.
Fig.6.15 shows the distribution of the reconstructed on-shell and off-shell candidate muon pair mass and the four-muon mass for the signal sample. The resolution of the same reconstructed quantities is shown in Fig.6.16, divided into the three kinematic regions, for the InclBrl4 layout, as an example. Fig.6.17 shows instead the comparison between the mass resolution in the three ITk layouts considered. These distributions were fitted with a gaussian shape employing an iterative method (see appendix C). Results are summarized in Tab.6.11, which shows that the ExtBrl4 layout has worse

	ExtBrl4		IExtBrl4		InclBrl4	
	Higgs	**ZZ**	**Higgs**	**ZZ**	**Higgs**	**ZZ**
Number of tracks	0.999	1.000	0.998	1.000	0.999	1.000
Hits	0.989	0.991	0.999	1.000	0.999	1.000
$\boldsymbol{p_4^T}$	0.558	0.548	0.628	0.640	0.630	0.638
$\boldsymbol{\Delta z}$	0.903	0.886	0.946	0.936	0.951	0.926
Isolation	0.982	0.979	0.988	0.984	0.987	0.984
Charge	0.958	0.955	0.940	0.944	0.953	0.936
$\boldsymbol{p_1^T}$	0.970	0.891	0.969	0.900	0.971	0.890
$\boldsymbol{p_2^T}$	0.949	0.923	0.957	0.909	0.953	0.928
$\boldsymbol{p_3^T}$	0.934	0.888	0.940	0.883	0.936	0.882
Off-shell muons	0.828	0.736	0.809	0.709	0.804	0.688
On-shell mass	0.917	0.820	0.937	0.807	0.926	0.816
Off-shell mass	0.946	0.989	0.943	0.986	0.946	0.988
Partial efficiency	0.289	0.196	0.343	0.227	0.343	0.220
Total efficiency	0.034	0.038	0.041	0.044	0.041	0.042

Table 6.6: Relative and total selection efficiencies for the three ITk layouts considered, only for the events with $3.2 < |\eta^{\mu}_{max}| < 4.0$. Relative efficiencies are defined as the fraction of events passing the selection from the previous step. Partial efficiency is the fraction of events passing the selection with respect to the total number of generated events in the kinematic region. Total efficiency is the fraction of events passing the selection with respect to the total number of generated events. The uncertainty on the total efficiency is not shown for graphical clarity and it is 0.006 for the Higgs sample and 0.007 for the ZZ sample.

performances in the forward region, as expected.

The reconstructed p_T and η distributions and resolution of the 4μ system are shown in Fig.6.18 and Fig.6.19 for the InclBrl4 layout. As for the masses, these distributions were fitted using a gaussian shape, and the results are summarized in Tab.6.12.

Compared with the results of the Scoping Document (Tab.6.1), the resolutions of the 4μ system are worse, but in our case no Z mass constraint is present, so the comparison is not fully consistent. With increasing pseudorapidity of the most forward muon candidate, resolutions decrease significantly, but the measurement also suffers from decrease of the statistics. To assess the impact of the final-state radiation, a special sample with reduced statistics was generated by including all the events, without any photon p_T

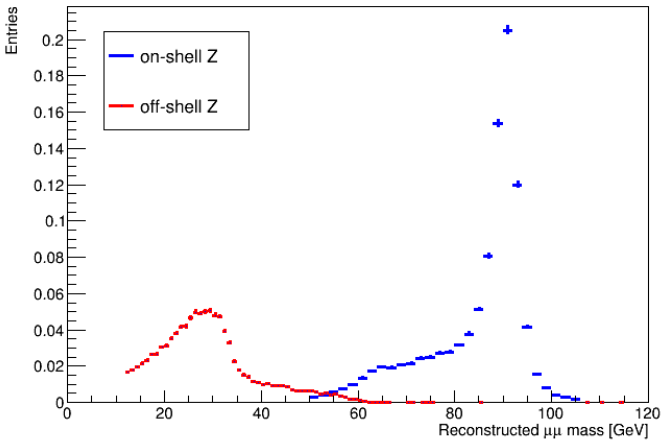

(a)

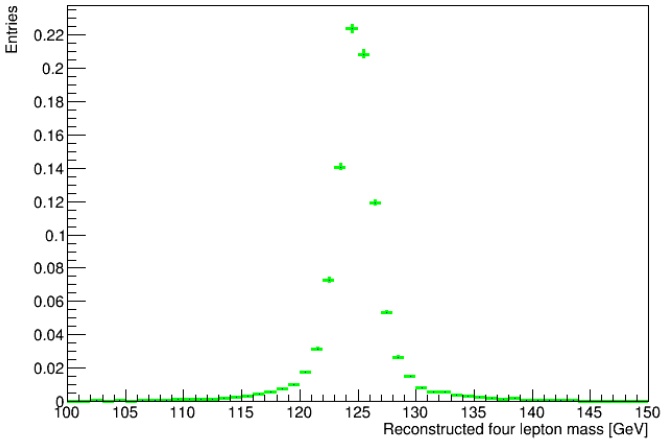

(b)

Figure 6.15: (a): $\mu\mu$ reconstructed mass distribution in the signal process; (b): 4μ reconstructed mass distribution in the signal process.

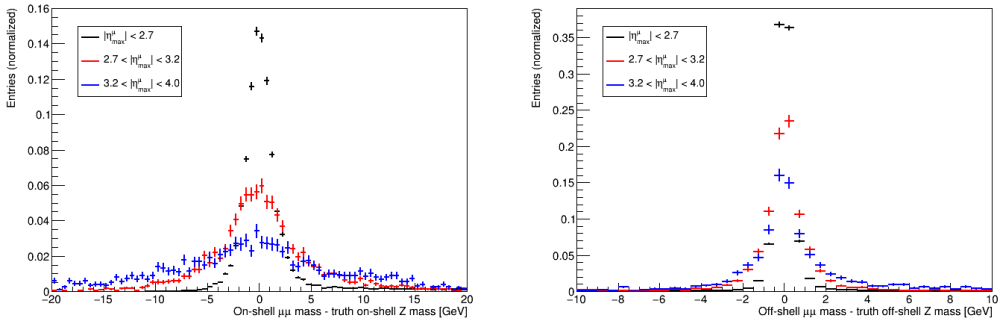

(a) (b)

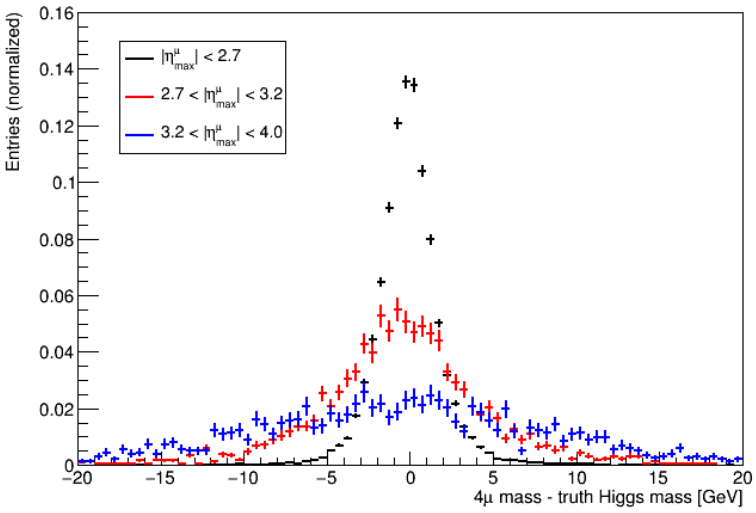

(c)

Figure 6.16: $\mu\mu$ (a, b) and 4μ (c) reconstructed mass resolution in three kinematic regions, for the InclBrl4 layout.

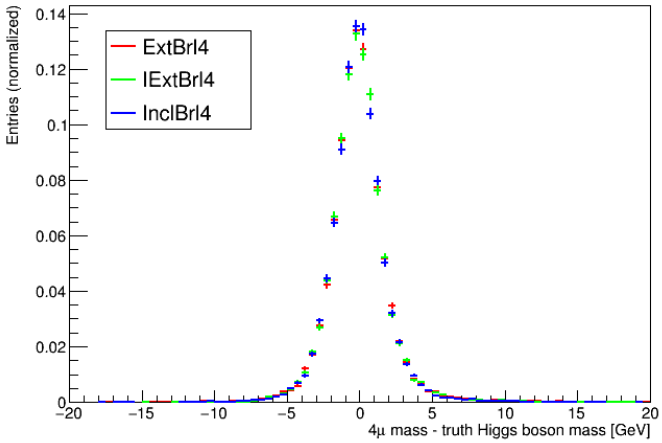

(a)

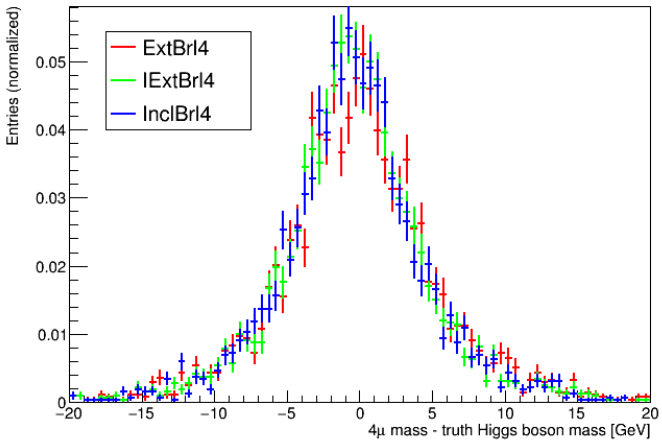

(b)

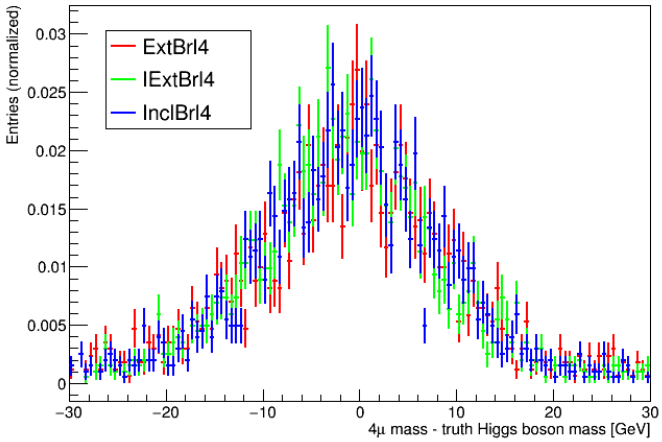

(c)

Figure 6.17: Comparison between the 4μ reconstructed mass resolution in the three considered ITk layouts separately for the events with $|\eta^{\mu}_{max}| < 2.7$ (a), $2.7 < |\eta^{\mu}_{max}| < 3.2$ (b), and $3.2 < |\eta^{\mu}_{max}| < 4.0$ (c).

	ExtBrl4		IExtBrl4		InclBrl4	
	Higgs	**ZZ**	**Higgs**	**ZZ**	**Higgs**	**ZZ**
$\langle\mu\rangle = 0$	0.551	0.332	0.567	0.348	0.568	0.347
$\langle\mu\rangle = 200$	0.548	0.332	0.565	0.345	0.566	0.344

Table 6.7: Total selection efficiencies for the three ITk layouts considered and two pile-up scenarios. The uncertainty on the total efficiency is not shown for graphical clarity and it is 0.002 for the Higgs sample and 0.003 for the ZZ sample.

	ExtBrl4		IExtBrl4		InclBrl4	
	Higgs	**ZZ**	**Higgs**	**ZZ**	**Higgs**	**ZZ**
$\langle\mu\rangle = 0$	0.658	0.478	0.662	0.482	0.663	0.481
$\langle\mu\rangle = 200$	0.657	0.480	0.659	0.480	0.661	0.480

Table 6.8: Total selection efficiencies for the three ITk layouts considered and two pile-up scenarios, only for the events with $|\eta^{\mu}_{max}| < 2.7$. The uncertainty on the total efficiency is not shown for graphical clarity and it is 0.003 for the Higgs sample and 0.005 for the ZZ sample.

requirement. The resolution on the 4μ mass system in this case is summarized in Tab.6.13. The results show that the resolution worsens in all the kinematic regions, as expected, but the InclBrl4 layout shows good performances in the forward region. We also expect that, in the final configuration, resolution will be improved by using the electromagnetic calorimeter.

Analysis of fake tracks

As explained in Chap.4.6, the fast simulation technique presents some limitations when defining a fake event in a physics process. One of the possible sources of fake events, especially at HL-LHC, could be the inclusion of a track produced by a pile-up particle into the combination of hard-scatter candidates. The absence of the full sample of tracks in the whole detector makes it impossible to correctly assess the importance of this effect. However, this study can be done with the available samples and provides an estimate (although optimistic) of the rate at which it happens.

Here, we define a fake event as an event that passes the requirements in which at least one of the following happens:

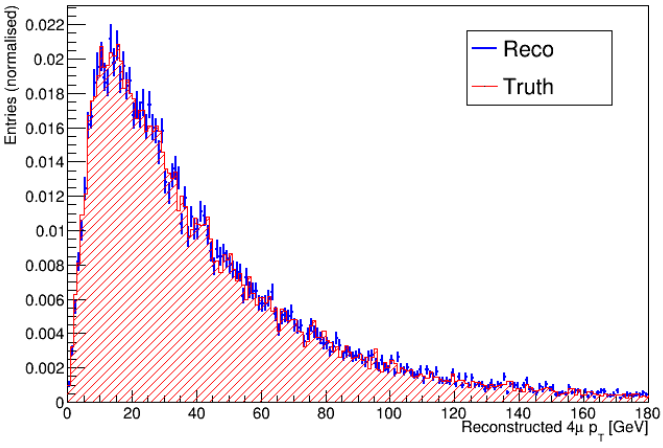

(a)

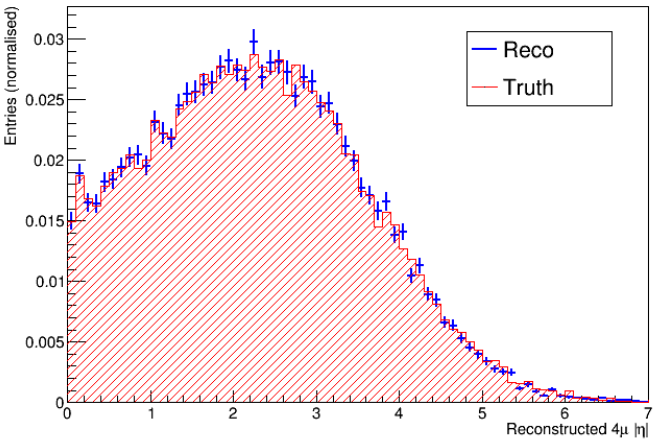

(b)

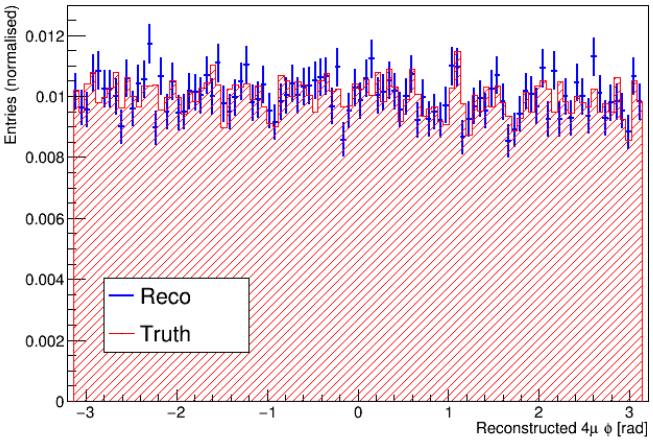

(c)

Figure 6.18: 4μ reconstructed p_T (a), η (b) and ϕ (c) spectrum.

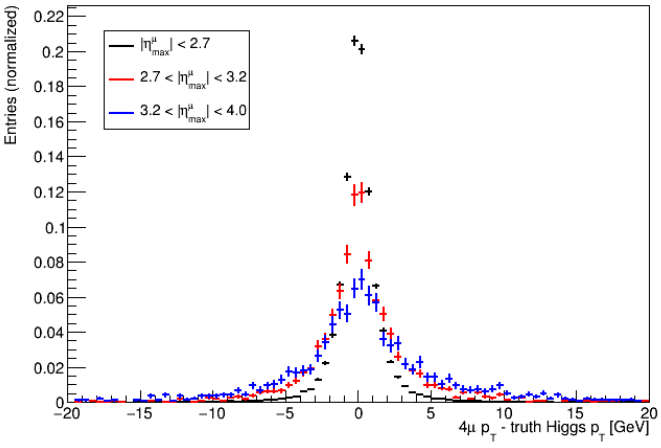

(a)

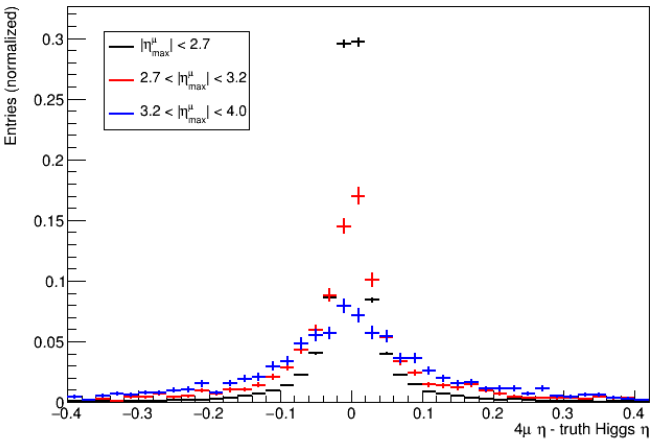

(b)

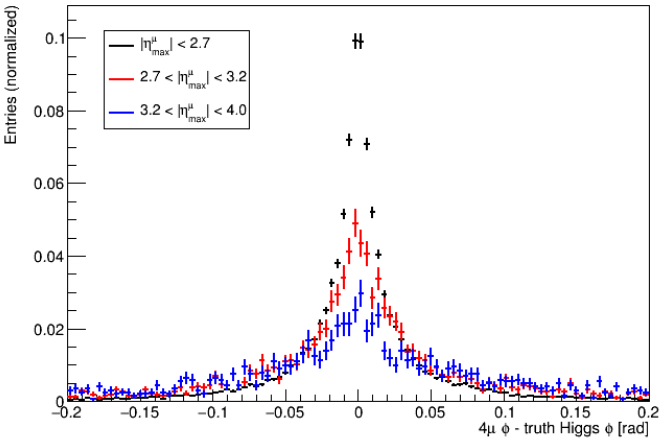

(c)

Figure 6.19: 4μ resolutions in p_T (a), η (b) and ϕ (c), comparing the performances in three kinematic regions.

	ExtBrl4		IExtBrl4		InclBrl4	
	Higgs	**ZZ**	**Higgs**	**ZZ**	**Higgs**	**ZZ**
$\langle\mu\rangle = 0$	0.453	0.34	0.519	0.40	0.519	0.40
$\langle\mu\rangle = 200$	0.448	0.33	0.513	0.38	0.516	0.38

Table 6.9: Total selection efficiencies for the three ITk layouts considered and two pile-up scenarios, only for the events with $2.7 < |\eta^{\mu}_{max}| < 3.2$. The uncertainty on the total efficiency is not shown for graphical clarity and it is 0.006 for the Higgs sample and 0.01 for the ZZ sample.

	ExtBrl4		IExtBrl4		InclBrl4	
	Higgs	**ZZ**	**Higgs**	**ZZ**	**Higgs**	**ZZ**
$\langle\mu\rangle = 0$	0.297	0.191	0.345	0.221	0.345	0.222
$\langle\mu\rangle = 200$	0.289	0.196	0.343	0.227	0.343	0.220

Table 6.10: Total selection efficiencies for the three ITk layouts considered and two pile-up scenarios, only for the events with $3.2 < |\eta^{\mu}_{max}| < 4.0$. The uncertainty on the total efficiency is not shown for graphical clarity and it is 0.006 for the Higgs sample and 0.007 for the ZZ sample.

	ExtBrl4	**IExtBrl4**	**InclBrl4**
On-shell resolution	1.26 ± 0.01	1.26 ± 0.01	1.27 ± 0.01
Off-shell resolution	0.400 ± 0.002	0.404 ± 0.002	0.405 ± 0.002
4μ **resolution**	1.55 ± 0.01	1.55 ± 0.01	1.55 ± 0.01
On-shell resolution - $|\eta^{\mu}_{max}| < 2.7$	1.21 ± 0.01	1.194 ± 0.010	1.198 ± 0.010
Off-shell resolution - $|\eta^{\mu}_{max}| < 2.7$	0.382 ± 0.002	0.382 ± 0.002	0.384 ± 0.002
4μ **resolution - $|\eta^{\mu}_{max}| < 2.7$**	1.46 ± 0.01	1.42 ± 0.01	1.42 ± 0.01
On-shell resolution - $2.7 < |\eta^{\mu}_{max}| < 3.2$	3.52 ± 0.10	3.07 ± 0.08	3.14 ± 0.08
Off-shell resolution - $2.7 < |\eta^{\mu}_{max}| < 3.2$	0.77 ± 0.02	0.68 ± 0.02	0.71 ± 0.02
4μ **resolution - $2.7 < |\eta^{\mu}_{max}| < 3.2$**	4.10 ± 0.10	3.69 ± 0.08	3.72 ± 0.09
On-shell resolution - $3.2 < |\eta^{\mu}_{max}| < 4.0$	7.5 ± 0.3	7.4 ± 0.2	7.9 ± 0.3
Off-shell resolution - $3.2 < |\eta^{\mu}_{max}| < 4.0$	1.21 ± 0.05	0.93 ± 0.03	0.95 ± 0.04
4μ **resolution - $3.2 < |\eta^{\mu}_{max}| < 4.0$**	9.2 ± 0.3	8.4 ± 0.2	8.6 ± 0.2

Table 6.11: On-shell, off-shell pair and 4μ mass resolution for the three ITk layouts considered, in total and separately for the three kinematic regions. The uncertainties are the fit parameters estimation uncertainties. Values are expressed in GeV.

- the charge associated with two or four tracks is wrong;
- at least one of the hard-scatter truth muons is outside the detector acceptance;

	ExtBrl4	**IExtBrl4**	**InclBrl4**
$\boldsymbol{p_T}$	0.960 ± 0.008	0.972 ± 0.008	0.953 ± 0.008
$\boldsymbol{\eta}$	0.0188 ± 0.0001	0.0187 ± 0.0001	0.0187 ± 0.0001
$\boldsymbol{\phi}$	0.0171 ± 0.0002	0.0171 ± 0.0002	0.0157 ± 0.0002
$\boldsymbol{p_T}$ - $\boldsymbol{\lvert\eta^{\mu}_{max}\rvert < 2.7}$	0.913 ± 0.007	0.930 ± 0.008	0.908 ± 0.007
$\boldsymbol{\eta}$ - $\boldsymbol{\lvert\eta^{\mu}_{max}\rvert < 2.7}$	0.0181 ± 0.0001	0.0179 ± 0.0001	0.0179 ± 0.0001
$\boldsymbol{\phi}$ - $\boldsymbol{\lvert\eta^{\mu}_{max}\rvert < 2.7}$	0.0152 ± 0.0002	0.0153 ± 0.0002	0.0151 ± 0.0002
$\boldsymbol{p_T}$ - $\boldsymbol{2.7 < \lvert\eta^{\mu}_{max}\rvert < 3.2}$	1.78 ± 0.05	1.71 ± 0.04	1.72 ± 0.04
$\boldsymbol{\eta}$ - $\boldsymbol{2.7 < \lvert\eta^{\mu}_{max}\rvert < 3.2}$	0.046 ± 0.001	0.038 ± 0.001	0.039 ± 0.001
$\boldsymbol{\phi}$ - $\boldsymbol{2.7 < \lvert\eta^{\mu}_{max}\rvert < 3.2}$	0.032 ± 0.001	0.036 ± 0.001	0.0279 ± 0.0008
$\boldsymbol{p_T}$ - $\boldsymbol{3.2 < \lvert\eta^{\mu}_{max}\rvert < 4.0}$	2.9 ± 0.1	2.96 ± 0.09	2.72 ± 0.10
$\boldsymbol{\eta}$ - $\boldsymbol{3.2 < \lvert\eta^{\mu}_{max}\rvert < 4.0}$	0.098 ± 0.004	0.097 ± 0.003	0.091 ± 0.003
$\boldsymbol{\phi}$ - $\boldsymbol{3.2 < \lvert\eta^{\mu}_{max}\rvert < 4.0}$	0.063 ± 0.003	0.062 ± 0.003	0.065 ± 0.003

Table 6.12: 4μ p_T, η and ϕ resolutions for the three ITk layouts considered, in total and separately for the three kinematic regions. The uncertainties are the fit parameters estimation errors. The values are expressed in GeV for the p_T and in radians for ϕ.

	ExtBrl4		**IExtBrl4**		**InclBrl4**	
	γ selection	**No selection**	**γ selection**	**No selection**	**γ selection**	**No selection**
$\boldsymbol{\lvert\eta^{\mu}_{max}\rvert < 2.7}$	1.46 ± 0.01	1.8 ± 0.1	1.42 ± 0.01	1.8 ± 0.1	1.42 ± 0.01	1.8 ± 0.1
$\boldsymbol{2.7 < \lvert\eta^{\mu}_{max}\rvert < 3.2}$	4.10 ± 0.10	4.8 ± 0.5	3.69 ± 0.08	4.6 ± 0.5	3.72 ± 0.09	4.3 ± 0.5
$\boldsymbol{3.2 < \lvert\eta^{\mu}_{max}\rvert < 4.0}$	9.2 ± 0.3	17 ± 2	8.4 ± 0.2	11 ± 1	8.6 ± 0.2	9 ± 1

Table 6.13: Comparison between the 4μ mass resolutions with or without the photon selection applied during the generation stage. Values are expressed in GeV.

- at least one of the muon candidates has a truth link pointing to a particle different from a hard-scatter muon.

First of all, a matching is needed for each event passing our requirements to compare the tracks and the hard-scatter muons. A matching was realized by comparing the candidate tracks vector with the hard-scatter truth muons vector and start by matching the pairs that are nearest (in ΔR) to each other. The pair is withdrawn and then the process is iterated. This method ensures, in case of a fake event, the correct identification of the fake tracks.

The measured charge fake rate was zero for the three layouts, which places this effect at the 10^{-4} level.

We found a case (in the ExtBrl4 layout) in which an event (over 50000 generated) passed all the requirements but one of the four muons was slightly

outside the detector acceptance.

The truth link was found incorrectly matched in one of the four tracks in 37, 41 and 39 events (over 50000 generated) respectively, for the ExtBrl4, IExtBrl4 and InclBrl4 layout, which is an effect at the 10^{-3} level. No events in which more than one track was incorrectly linked were found. It was verified that the reason for which the truth link fails to identify the hard-scatter muon is that the muon itself has produced a secondary particle in one of the first layers, so that the track is mostly due to the muon after the interaction, and is slightly deviated.

The measured fake rate is therefore extremely low and does not depend on pile-up at this level. This confirms that the layouts being considered by ATLAS are adequate to the requirements of the high luminosity phase.

Signal significance

In order to assess the significance of our findings, selected events, both for the signal and the background processes, were scaled to an integrated luminosity of 3000 fb^{-1}, which is the expected value at the end of HL-LHC operations, in 2036. Note that the processes were generated at $\sqrt{s} = 13$ TeV, at a lower cross section with respect to the expected HL-LHC one, therefore slightly underestimating the signal yield. Scaling factor was computed by using the theoretical values of the cross sections and the branching ratios, and the measured generation and analysis efficiencies. The number of expected events at a particular integrated luminosity is given by:

$$N = (\sigma \times BR) \cdot \mathcal{L} \cdot \epsilon_{gen.cuts} \cdot \epsilon_{gen.selection} \cdot \epsilon_{analysis},$$

where $\epsilon_{gen.cuts}$ is the fraction of events passing the generation selection applied in order to optimize the generation process, as described in Chap.6.3.2, $\epsilon_{gen.selection}$ is the fraction of events being passed to the sim/digit/reco chain with respect to the generated sample and ϵ_{cuts} is the analysis selection efficiency, $\sigma \times BR$ is the production cross section for the particular decay mode and $\mathcal{L}$ is the integrated luminosity.

The measured values are $\epsilon_{gen.cuts} = 100$ %, $\epsilon_{gen.selection} = 81.2 \pm 0.1$ % for the Higgs sample and $\epsilon_{gen.cuts} = 25$ %, $\epsilon_{gen.selection} = 80.8 \pm 0.2$ % for the background sample. The analysis efficiencies were described in Chap.6.6.2 and depend weakly on the considered ITk layout. The values used for the cross sections are $\sigma\times$ BR = 1.64 fb for the signal process and $\sigma\times$ BR = 24

fb for the background process, using Powheg[37] estimate.

In order to evaluate the effect of the ITk angular coverage extension on the significance of this channel, the analysis was also carried out for different η coverage by selecting events with $|\eta^{\mu}_{max}| < 2.7$, $|\eta^{\mu}_{max}| < 3.2$ and $|\eta^{\mu}_{max}| < 4.0$. The results are shown for the InclBrl4 layout in Fig.6.20. Looking at the plots in Fig.6.16-6.19 we can see that the 4μ invariant mass resolution appears good enough that a meaningful exercise can be performed.

To define the signal measurement, we integrate a region of $\pm 1.5\ \sigma$ around the measured resonance peak in the 4μ invariant mass distribution. The fit was performed iteratively using a gaussian shape. Results for the different layouts and angular coverage are summarized in Tab.6.14.

ExtBrl4	**S**	**B**	**S/B**	$\frac{S}{\sqrt{S+B}}$	$\Delta\mu/\mu$
$\|\eta^{\mu}_{max}\| < 2.7$	1648 ± 41	183 ± 14	9.0	38.5 ± 0.7	0.026
$\|\eta^{\mu}_{max}\| < 3.2$	1756 ± 42	227 ± 15	7.7	39.4 ± 0.7	0.025
$\|\eta^{\mu}_{max}\| < 4.0$	1788 ± 42	255 ± 16	7.0	39.6 ± 0.7	0.025
IExtBrl4	**S**	**B**	**S/B**	$\frac{S}{\sqrt{S+B}}$	$\Delta\mu/\mu$
$\|\eta^{\mu}_{max}\| < 2.7$	1655 ± 41	168 ± 13	9.8	38.8 ± 0.7	0.026
$\|\eta^{\mu}_{max}\| < 3.2$	1790 ± 42	226 ± 15	7.9	39.9 ± 0.7	0.025
$\|\eta^{\mu}_{max}\| < 4.0$	1830 ± 43	266 ± 16	6.9	40.0 ± 0.7	0.025
InclBrl4	**S**	**B**	**S/B**	$\frac{S}{\sqrt{S+B}}$	$\Delta\mu/\mu$
$\|\eta^{\mu}_{max}\| < 2.7$	1672 ± 41	175 ± 13	9.6	38.9 ± 0.7	0.026
$\|\eta^{\mu}_{max}\| < 3.2$	1809 ± 43	230 ± 15	7.9	40.1 ± 0.7	0.025
$\|\eta^{\mu}_{max}\| < 4.0$	1851 ± 43	266 ± 16	7.0	40.2 ± 0.7	0.024

Table 6.14: Expected signal, background, signal-to-background ratio and significance for different ITk layouts and detector coverage. The indicated errors on the signal and backgrounds are purely statistical. Scale errors due to efficiency measurement errors are negligible.

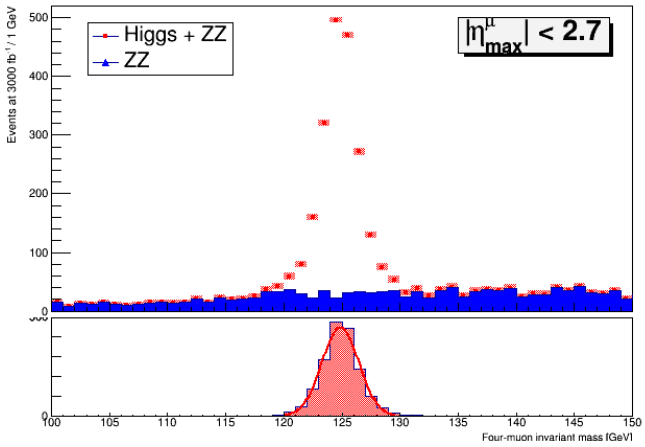

(a)

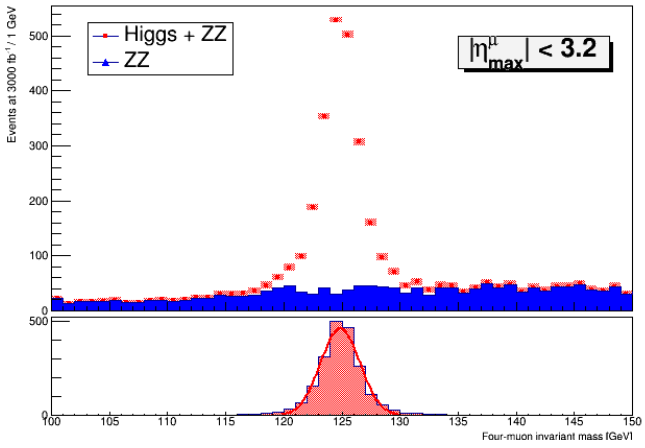

(b)

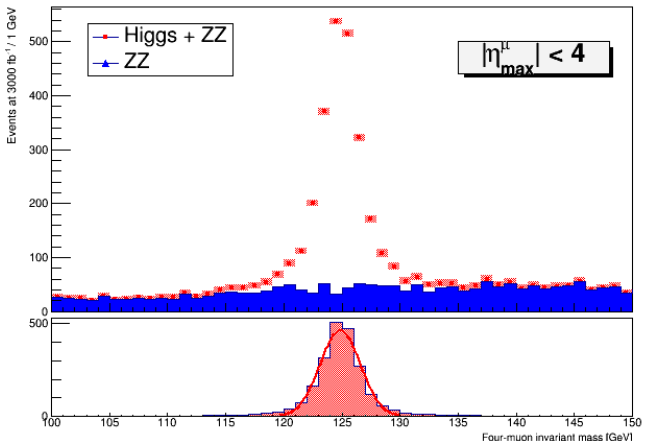

(c)

Figure 6.20: Top: expected measured 4μ invariant mass distribution at 3000 fb^{-1} of integrated luminosity (signal + background) in three angular coverage scenarios, for the InclBrl4 layout. Bottom: signal fit with a gaussian shape.

The results show compatibility of the significance of the layouts within the errors. As a function of the angular coverage, the signal-to-background ratio worsens, but the significance, defined as $\frac{S}{\sqrt{S+B}}$, increases. Compared with the results from the Scoping Document in the Reference Scenario ($|\eta| < 4.0$ coverage, Tab.6.2), the number of signal and background events is smaller. The discrepancy is explained by different factors:

- the samples were generated at $\sqrt{s} = 13$ TeV instead of 14 TeV in the present study. The Higgs production cross section is smaller by a factor of 1.13;
- the Scoping Document study includes all the Higgs production modes, whereas the ggF process represents the 86% of the total;
- the applied generation selection excluded 20% of the events due to photons, that could have been recovered with the electromagnetic calorimeter.

For the background process the difference is also partially due to the same reasons, but other effects tend to increase the difference. An important difference between the two analyses is that the Scoping Document analysis employs a Z mass constraint in the reconstruction algorithm. However, in the reference scenarios used in the Scoping Document is not obvious that it is possible to separate Higgs from ZZ* in the region $|\eta| > 2.7$.

Conclusions

The High Luminosity Phase of the LHC will provide unique opportunities to precision studies of the Higgs Boson properties.

Due to the large integrated luminosity (3000 fb^{-1}), rare decay channels can be searched for and couplings measured with accuracy at the few percent level. In order to exploit these opportunities, the ATLAS Collaboration is currently studying different options for the upgrades of its inner tracker, the heart of the spectrometer. Due to the large number (on average 200) of overlapping events to the high instantaneous luminosity, this tracker must be robust both in terms of radiation tolerance as of in terms of occupancy, therefore several (at the moment three) different layouts are being studied. Due to the large CPU time required to simulate events with such a large pile-up, for so many layouts, we have developed a tool for a fast simulation that, however, avoids parametrizations and allows to perform realistic tracking studies, both in terms of single particle production, and for some physics processes.

Our work shows that , while no clear choice among the different layouts can be drawn at this stage, the extension of the η coverage up to $|\eta| = 4.0$ will provide the Higgs studies with better statistics. A signal-to-background ratio of at least 7 can be obtained in the $H \to ZZ^* \to 4\mu$ channel alone, with an estimated experimental $\Delta\mu/\mu$ of about 2.5% (before inclusion of luminosity uncertainty) for the various layouts, which is very close to the requirement of the Collaboration.

Appendices

Appendix A

ATLAS reference frame and track parameters

Fig.A.1 shows the ATLAS frame of reference (e_x, e_y, e_z), where e_z is parallel to the beam line and e_x, e_y lie on the transverse plane and are oriented so that the system is right-handed. A reconstructed track is completely characterized by five variables, called the *perigee parameters*, also shown in Fig.A.1, which are the **transverse impact parameter** d_0, **the longitudinal impact parameter** z_0, the **polar angle** θ, commonly replaced by the pseudo-rapidity $\eta = -\log\tan\frac{\theta}{2}$, the **azimuthal angle** ϕ, the measured charge divided by the p_T, $\boldsymbol{q/p_T}$. In standard analyses, the impact parameters are calculated with respect to the primary vertex, so large values of these variables typically indicate the presence of a secondary vertex produced by the decay of a long-lived particle. In the reconstruction algorithm used to produce the samples for our analysis, however, a primary vertex reconstruction algorithm is not present, so the longitudinal impact parameter is calculated with respect to the origin of the axes. When calculating z_0 resolution, however, the truth z_0 is assumed as the z coordinate of the primary vertex, which is a good approximation due to the small transverse dimensions of the LHC bunch ($\simeq 15$ μm). The same applies for the transverse impact parameter, where the truth d_0 is assumed as 0. In this case, the intrinsic d_0 resolution was calculated by subtracting in quadrature the beam transverse dimensions:

$$\sigma^2_{d0,intrinsic} = \sigma^2_{d0,measured} - 0.5 \cdot \sigma^2_{beam,x} - 0.5 \cdot \sigma^2_{beam,y}$$

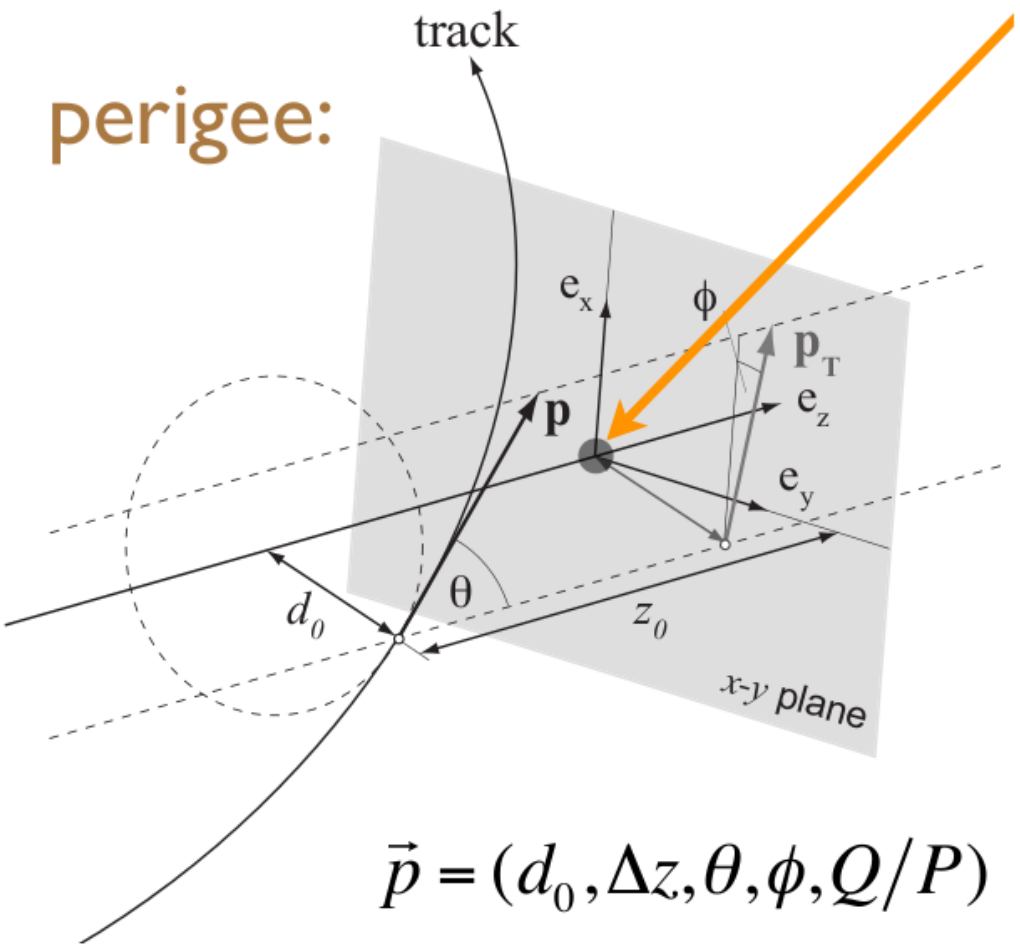

Figure A.1: ATLAS frame of reference and perigee parameters. The orange arrow indicates the position of the reconstructed primary vertex.

Appendix B

Monte Carlo generators

B.1 Minimum bias events: Pythia 8

Pythia 8 is a program used to generate high-energy collisions that employs a set of physics models to simulate the evolution of a hard process from the interaction between few bodies to a possibly complex multihadronic final state[39].
It employs a *leading-logarithm algorithm* to simulate the hard processes, taking into account inital- and final-state parton shower, multiple interactions, beam remnants and hadronisation. The version used was Pythia 8.210.

B.2 $H \to ZZ^* \to 4\mu$: Powheg

POsitive Weight Hardest Emission Generator (POWHEG) is a Next-to-leading order (NLO) Monte Carlo generator used when the classic leading logarithm methods accuracy is not sufficient to correctly represent the physical process of interest. POWHEG-BOX is a computer framework that implements the theoretical construction of POWHEG, computing the matrix element at NLO[37]. In this thesis, the POWHEG generator is employed to produce Higgs samples from gluon-gluon fusion. This process, which is the dominant Higgs production channel at LHC, receives very large NLO QCD corections, which are important to test the electroweak symmetry breaking mechanism[40]. The residual uncertainty on the total cross section at NLO comes mainly from higher-order QCD effects and from the parton distribution functions uncertainties.

Appendix C

Iterative gaussian fit

A gaussian fit is performed following an iterative method. During the first iteration the fit parameters, which are amplitude, mean and σ of the gaussian distribution, are estimated using the histogram peak, mean and RMS value. A fit is performed by limiting the range to 3σ around the mean. The parameters obtained from the fit are used as input for the next iteration. The iteration stops when the relative variation of each parameter between two consecutive iterations is below a certain threshold, that was fixed to 10^{-4}.

Bibliography

[1] ATLAS Collaboration. "Phase-II Upgrade Scoping document". *CERN-LHCC-2015-020 LHCC-G-166*, 2015.

[2] ATLAS Collaboration. "Letter of Intent Phase-II Upgrade". *CERN-2012-022 LHCC-I-023*, 2012.

[3] C. Rubbia. "The Discovery of the W and Z bosons". *Phys. Rept.*, 239:241–284, 1994.

[4] CDF Collaboration. "Observation of Top Quark Production in $\overline{p}p$ Collisions with the Collider Detector at Fermilab". *Phys. Rev. Lett.*, 74:2626–2631, Apr 1995.

[5] D0 Collaboration. "Observation of the Top Quark". *Phys. Rev. Lett.*, 74:2632–2637, Apr 1995.

[6] ATLAS Collaboration. "Observation of a new particle in the search for the Standard Model Higgs boson with the ATLAS detector at the LHC". *Phys. Lett.*, B716:1–29, 2012.

[7] CMS Collaboration. "Observation of a new boson at a mass of 125 GeV with the CMS experiment at the LHC". *Phys. Lett.*, B716:30–61, 2012.

[8] P. Higgs. "Broken Symmetries and the Masses of Gauge Bosons". *Phys. Rev. Lett.*, 13:508–509, 1964.

[9] ATLAS Collaboration. "Projections for measurements of Higgs boson signal strengths and coupling parameters with the ATLAS detector at a HL-LHC". *ATL-PHYS-PUB-2014-016*, Geneva, Oct 2014.

[10] D. Ghosh, R. Godbole, M. Guchait, K. Mohan, D. Sengupta. "Looking for an Invisible Higgs Signal at the LHC". *Phys. Lett.*, B725:344–351, 2013.

[11] LHC Higgs Cross sections Working Group. "Twiki page". *https://twiki.cern.ch/twiki/bin/view/LHCPhysics/CrossSections.*

[12] ATLAS Collaboration. "Physics at a High-Luminosity LHC with ATLAS". *ATL-PHYS-PUB-2012-001, ATL-COM-PHYS-2012-1118*, 2012.

[13] ATLAS Collaboration. "Studies of the ATLAS potential for Higgs self-coupling measurements at a High Luminosity LHC". *ATL-PHYS-PUB-2013-002*, 2013.

[14] ATLAS Collaboration. "Studies of Vector Boson Scattering with an Upgraded ATLAS Detector at a High-Luminosity LHC". *ATL-PHYS-PUB-2012-005*, Geneva, Nov 2012.

[15] ATLAS Collaboration. "ATLAS Magnet System: Technical Design Report". Geneva, 1997.

[16] H. H. J. Ten Kate. "The ATLAS Superconducting Magnet System Performance". *IEEE Trans. Appl. Superc. 17, 1191,* http://ieeexplore.ieee.org/xpl/articleDetails.jsp?arnumber=4277757, 2007.

[17] ATLAS Collaboration. "The ATLAS Experiment at the CERN Large Hadron Collider". *Journal of Instrumentation*, 3:S08003, 2008.

[18] A. Miucci. "The ATLAS Insertable B-Layer project". *Journal of Instrumentation*, 9(02):C02018, 2014.

[19] ATLAS Collaboration. "ATLAS Inner Detector: Technical design report. Vol. 1". Geneva, 1997.

[20] ATLAS Collaboration. "ATLAS Liquid-Argon Calorimeter: Technical Design Report". *ATLAS-TDR-2; CERN-LHCC-96-041,* http://cds.cern.ch/record/331061?ln=en, 1996.

[21] T. Barillari. "The ATLAS Liquid Argon Hadronic End-Cap Calorimeter: Construction and selected beam test results". *Nucl.Phys.Proc.Suppl.150:102-105*, 2004.

[22] ATLAS Collaboration. "ATLAS Muon Spectrometer: Technical Design Report". *Technical Design Report ATLAS.* CERN, Geneva, 1997.

[23] D. Green, editor. "At the leading edge: The ATLAS and CMS LHC experiments". 2010.

[24] M. Shochet, L. Tompkins, V. Cavaliere, P. Giannetti, A. Annovi, G. Volpi. "Fast TracKer (FTK) Technical Design Report". *CERN-LHCC-2013-007. ATLAS-TDR-021*, Geneva, Jun 2013.

[25] S. Xella. "Physics object reconstruction in the ATLAS experiment". *PoS*, page 011, 2012.

[26] ATLAS Collaboration. "The Optimization of ATLAS Track Reconstruction in Dense Environments". *ATL-PHYS-PUB-2015-006*, Geneva, Mar 2015.

[27] C. Gemme. Private communication. INFN Genova.

[28] ATLAS Collaboration. "Muon reconstruction performance of the ATLAS detector in proton–proton collision data at $\sqrt{s}$ =13 TeV". *Eur. Phys. J.*, C76(5):292, 2016.

[29] ATLAS Collaboration. "Simulation of Pile-up in the ATLAS Experiment". *Journal of Physics: Conference Series*, 513(2):022024, 2014.

[30] G. Aad and others. "Studies of the performance of the ATLAS detector using cosmic-ray muons". *Eur. Phys. J.*, C71:1593, 2011.

[31] S. Agostinelli and others. "GEANT4: A Simulation toolkit". *Nucl. Instrum. Meth.*, A506:250–303, 2003.

[32] W. Bhimji, J. Cranshaw, P. van Gemmeren, D. Malon, R.D. Schaffer, I. Vukotic. "The ATLAS ROOT-based data formats: recent improvements and performance measurements". *ATL-SOFT-PROC-2012-020, ATL-COM-SOFT-2012-054*, Geneva, 2012.

[33] R. Brun, E. Rademakers. "ROOT: An object oriented data analysis framework". *Nucl. Instrum. Meth.*, A389:81–86, 1997.

[34] A. Aimar, J. Harvey, N. Knoors. "Computing in High Energy Physics and Nuclear Physics 2004". Geneva. 2 volumes, consecutive pagination.

[35] S. Tsuno. Private communication. High Energy Accelerator Research Organization (KEK).

[36] ATLAS Collaboration. "Performance Specifications of the Tracker Phase II Upgrade". *ATL-UPGRADE-PUB-2012-003*, Sep 2012.

[37] C. Oleari. "The POWHEG-BOX". *Nucl. Phys. Proc. Suppl.*, 205-206:36–41, 2010.

[38] ATLAS Collaboration. "Measurements of Higgs boson production and couplings in the four-lepton channel in pp collisions at center-of-mass energies of 7 and 8 TeV with the ATLAS detector". *Phys. Rev.*, D91(1):012006, 2015.

[39] T. Sjostrand, S. Mrenna, P. Skands, Z. Peter. "A Brief Introduction to PYTHIA 8.1". *Comput. Phys. Commun.*, 178:852–867, 2008.

[40] E. Bagnaschi, G. Degrassi, P. Slavich, A. Vicini. "Higgs production via gluon fusion in the POWHEG approach in the SM and in the MSSM". *JHEP*, 02:088, 2012.